

Oil & Natural Gas Technology

Detection and Production of Methane Hydrate

End of Phase 4; Continuation Report

Reporting Period: July 2009-June 2010

Submitted by:

Rice University, University of Texas, and Oklahoma State University

George J. Hirasaki and Walter Chapman, Chemical and Biomolecular Engineering

Gerald R. Dickens, Colin A. Zelt, and Brandon E. Dugan, Earth Science

Kishore K. Mohanty, University of Texas

Priyank Jaiswal, Oklahoma State University

June, 2010

DOE Award No.: DE-FC26-06NT42960

John Terneus, Program Officer

Rice University – MS 362

6100 Main St.

Houston, TX 77251-1892

Phone: 713-348-5416; FAX: 713-348-5478; Email: gjh@rice.edu

Prepared for:

United States Department of Energy

National Energy Technology Laboratory



Office of Fossil Energy

Table of Contents

Disclaimer	3
Executive Summary	4
Background.....	6
Task 5: Carbon Inputs and Outputs to Gas Hydrate Systems	7
Task 6: Numerical Models for Quantification of Hydrate and Free Gas Accumulations.....	11
Compositional Effect on BSR.....	11
Blanking and chaotic zones due to hydrate distribution	19
Sulfate, Bicarbonate, Calcium and carbon isotope ($\delta^{13}\text{C}$) balance as an indicator of methane flux	33
Processes leading to overpressure	58
Concentrated hydrate and free gas.....	58
Task 7: Analysis of Production Strategy	60
Task 8: Seafloor and Borehole Stability	70
Task 9: Geophysical Imaging of Gas Hydrate and Free Gas Accumulations...	86
Task 10 Technology Transfer	98
Cost Plan / Status	101
Milestone Plan / Status	102
Success Criteria.....	108

Disclaimer

This report was prepared as an account of work sponsored by an agency of the United States Government. Neither the United States Government nor any agency thereof, nor any of their employees, makes any warranty, express or implied, or assumes any legal liability or responsibility for the accuracy, completeness, or usefulness of any information, apparatus, product, or process disclosed, or represents that its use would not infringe privately owned rights. Reference herein to any specific commercial product, process, or service by trade name, trademark, manufacturer, or otherwise does not necessarily constitute or imply its endorsement, recommendation, or favoring by the United States Government or any agency thereof. The views and opinions of authors expressed herein do not necessarily state or reflect those of the United States Government or any agency thereof.

Executive Summary

Task 5: Carbon Inputs and Outputs to Gas Hydrate Systems

Subtask 5.1. Iodine cycling. We have completed measurements of iodine in pore water and sediment from cores of Blake Ridge, Peru Margin, Gulf of Mexico and Sea of Japan. We have measured the amount and isotopic composition of organic carbon in sediment from the Peru Margin. We have the data tabulated and interpreted, and have nearly finished a manuscript on these findings. We are presently incorporating iodine cycling into our 1-D numerical models for gas hydrate formation.

Subtask 5.2. Authigenic minerals. We have completed measurements of inorganic carbon (concentration and isotopes) and metals (Ca, Mg Fe, S and Ba) in pore water and sediment from cores on Blake Ridge, Peru Margin, Gulf of Mexico and Japan Sea. We have the data tabulated and interpreted, and have completed one manuscript so far on these findings. We have incorporated some of this data into our 1-D numerical models for gas hydrate formation, and have recently presented this work (see Subtask 6.8). Glen Snyder is presently collecting additional samples from the Sea of Japan with colleagues from the University of Tokyo.

Glen Snyder is presently assisting Andrew Hunt of the USGS Noble Gas laboratory in Colorado to collect and analyze noble gases from pore waters and gas hydrates in gas hydrate systems.

Task 6: Numerical Models for Quantification of Hydrate and Free Gas Accumulations

Subtask 6.3, Compositional Effect on BSR. The ability to generate synthetic seismogram with Ricker wavelets on some cases of hydrate/gas transition has been established, and has been applied to the methane – propane hydrate system.

Subtask 6.4. Blanking and chaotic zones due to hydrate distribution. We have started working on acoustic velocity profiles in different types of sediment layers. Due to hydrate accumulation, the velocity in different types of sediment layers can become similar with each other. 2-D code has been developed to consider 2-D lithology heterogeneity. Simulation show that high permeability conduits are very important for high saturation hydrate/free gas accumulation.

Subtask 6.8 (b): Sulfate, bicarbonate, calcium and carbon isotope ($\delta^{13}\text{C}$) profiles as an indicator of methane flux above marine gas hydrate systems

Methane flux is an important constraint on the amount of hydrate that may be present in marine sediments. One approach to determine this flux is to use the depth to the sulfate-methane transition (SMT). Pore-water sulfate concentrations deplete to zero in shallow sediments above methane hydrate systems. Many

authors attributed these chemical gradients to anaerobic oxidation of methane (AOM) at the SMT and directly related the depth of the SMT to the upward methane flux at steady-state conditions. However, an alternative mechanism for sulfate consumption by particulate organic carbon (POC) has been interpreted by various authors. To reconcile these two interpretations, *Bhatnagar and others' 1-D model* (2008) was extended and methane, sulfate, dissolved inorganic carbon (DIC), calcium and carbon isotope concentration profiles were computed with both advective and diffusive fluxes.

Task 7: Analysis of Production Strategy

A large deposit of gas hydrate is found in the Gulf of Mexico (GOM) block AC 818. In the last 6 months, we have worked on assessing the production from this block using a thermal, compositional, 3-D simulator in equilibrium mode. Four components (water, methane, hydrate and salt) and four phases (gas, aqueous-phase, hydrate and ice) are considered where salt is assumed to be in aqueous phase only. The reservoir GOM, block AC 818 is reported to be an unconfined reservoir. For these types of reservoirs, depressurization is ineffective and warm water flooding is necessary for production. We study different well configurations for production from this hydrate reservoir using warm water flooding.

Task 8: Seafloor and Borehole Stability

We are concentrating on different scales of failure in gas hydrate systems ranging from bed-scale fracture genesis to regional-scale slope failure (Subtask 8.2). This work, which is grounded on data collected from previous hydrate studies (Subtasks 8.1 and 8.3), is not only providing constraints on what drives different types of failure, but it is also helping us characterize the controls on heterogeneous hydrate accumulations. This has led to our involvement in other hydrate collaborations with the Chevron Gulf of Mexico JIP, hydrate studies in China, and hydrate studies in Cascadia (building on Subtask 8.3 and general collaborations within DOE and outside of DOE).

Task 9: Geophysical Imaging of Gas Hydrate and Free Gas Accumulations

The seismic data that is being used for Task 9 comes from Krishna-Godavari (K-G) Basin in the Indian east coast. The well data were collected during the NGHP drilling expedition in 2005. The PI is successfully collaborating with National Institute of Oceanography (NIO), India.

A pre-stack depth migrated image was generated using velocity model from composite inversion/migration that agreed very well with the sonic log suggesting that the velocity model and the depth image were geologically accurate.

Background

A. Objective

This project seeks to understand regional differences in gas hydrate systems from the perspective of as an energy resource, geohazard, and long-term climate influence. Specifically, the effort will: (1) collect data and conceptual models that targets causes of gas hydrate variance, (2) construct numerical models that explain and predict regional-scale gas hydrate differences in 2- and 3-dimensions with minimal “free parameters”, (3) simulate hydrocarbon production from various gas hydrate systems to establish promising resource characteristics, (4) perturb different gas hydrate systems to assess potential impacts of hot fluids on seafloor stability and well stability, and (5) develop geophysical approaches that enable remote quantification of gas hydrate heterogeneities so that they can be characterized with minimal costly drilling. Our integrated program takes advantage of the fact that we have a close working team comprised of experts in distinct disciplines.

The expected outcomes of this project are improved exploration and production technology for production of natural gas from methane hydrates and improved safety through understanding of seafloor and well bore stability in the presence of hydrates.

B. Scope of Work

The scope of this project is to more fully characterize, understand, and appreciate fundamental differences in the amount and distribution of gas hydrate and how this affects the production potential of a hydrate accumulation in the marine environment. The effort will combine existing information from locations in the ocean that are dominated by low permeability sediments with small amounts of high permeability sediments, one permafrost location where extensive hydrates exist in reservoir quality rocks and other locations deemed by mutual agreement of DOE and Rice to be appropriate. The initial ocean locations are Blake Ridge, Hydrate Ridge, Peru Margin and GOM. The permafrost location is Mallik. Although the ultimate goal of the project is to understand processes that control production potential of hydrates in marine settings, Mallik will be included because of the extensive data collected in a producible hydrate accumulation. To date, such a location has not been studied in the oceanic environment. The project will work closely with ongoing projects (e.g. GOM JIP and offshore India) that are actively investigating potentially economic hydrate accumulations in marine settings.

The overall approach is fivefold: (1) collect key data concerning hydrocarbon fluxes which is currently missing at all locations to be included in the study, (2) use this and existing data to build numerical models that can explain gas hydrate variance at all four locations, (3) simulate how natural gas could be produced from each location with different production strategies, (4) collect new sediment property data at these locations that are required for constraining fluxes, production simulations and assessing sediment stability, and (5) develop a method for remotely quantifying heterogeneities in gas hydrate and free gas distributions. While we generally restrict our efforts to the locations where key parameters can be measured or constrained, our ultimate aim is to make our efforts universally applicable to any hydrate accumulation.

Task 5: Carbon Inputs and Outputs to Gas Hydrate Systems

Gerald Dickens and Glen Snyder

Summary

The amount and distribution of gas hydrate in marine sediment sequences at the regional scale depend on inputs and outputs of carbon over time. The main input is solid organic carbon, which is converted to methane by microbes or heat. Depending on location, the main outputs are anaerobic oxidation of methane (AOM), venting, and gas burial. The primary scope of this task is to generate chemical constraints on carbon inputs and outputs, which can be incorporated into numerical models, especially those developed as part of this project (i.e., Bhatnagar et al., 2007). We have generated most of the proposed data, and have arrived at solid interpretations for this data. Much of our effort in the past two years has been to verify interpretations given competing hypotheses regarding AOM and the sulfate methane transition (SMT) (cf. Kastner et al., 2008; Dickens and Snyder, 2009). Our current efforts are now focused on presenting this data in talks and papers, and using it to test and constrain our numerical models. There are now very strong overlaps between Task 5 and parts of Task 6 (e.g., Subtask 6.8).

Milestone Status

5.1a Measure iodine in sediments. We have completed the first-ever synthesis of all literature concerning iodine in marine sediment, tabulating and interpreting the concentrations in pore water and sediment. We have supplemented this data with new measurements, especially pertaining to gas hydrate systems. We now have a very good understanding on the distribution of iodine and its relationship to methane and gas hydrates. A manuscript will be submitted shortly.

5.1b Constrain C_{org} inputs from iodine. We have completed measurements of organic carbon for Site 1230. We are collecting new samples from the Sea of Japan to further this work. We are now specifically incorporating organic carbon and iodine into numerical models for gas hydrate formation. This objective is somewhat behind schedule because a cruise was postponed, because interpretations required a full-blown synthesis, and because we needed a new student. This is now progressing very well.

5.1c Construct metal profiles in sediments. We have measured metal contents in pore water and sediment from cores of four gas hydrate systems. The initial Sea of Japan work has been published (Snyder et al., 2007) and the Peru Margin work is almost ready for submission.

5.2b Modeling/integrating (geochemical) profiles. We have incorporated results from authigenic minerals into models (Subtask 6.8). We have written an article defending our use of the SMT as a proxy for methane loss through AOM (Dickens and Snyder, 2009).

Subtask 5.1. Iodine cycling

Solid organic carbon landing on the seafloor incorporates small amounts of iodate from seawater (IO_3^-). During burial and diagenesis, this iodine is released to pore waters as iodide (I^-), which can then diffuse. However, near the seafloor, where dissolved O_2 occurs, the iodide is converted back to iodate and reabsorbed onto organic carbon. The net consequence is a “build-up” of iodine in pore waters that represents the long-term input of organic carbon. In theory, the amount of iodine in pore water should relate to the amount of gas hydrate, although such a relationship may be complex.

As shown in previous reports, our results indicate that diffusion dominated gas hydrate systems (e.g., Blake Ridge, Peru Margin) have extremely high dissolved iodine concentrations. Indeed, concentrations can be over 5 orders of magnitude greater than that in seawater. The remarkably high concentrations almost assuredly attest to organic carbon input over millions of years. Based on our work so far, there are definitely first order relationships between the amount and distribution of iodine and the accumulation of organic carbon. We have written a manuscript on this topic, and will submit it soon after Glen Snyder (lead author) returns from Japan.

We are presently adding iodine into a 1-D version of our numerical model. Basically, organic carbon landing on the seafloor (α in our model) contains a small amount of iodine. As the organic carbon is buried and converts to methane, iodine is released to pore waters and diffuses through the sediment column with parameters dictated by the model. The current goals of this exercise are threefold: (1) can our numerical model generate the different iodine profiles at multiple sites using “realistic” values for sediment properties? (2) what are the primary model parameters that govern the iodine profiles? (3) how are the iodine profiles related to gas hydrate abundance? In theory, a reasonable model for gas hydrate formation in marine sediment should be able to produce reasonably accurate gas hydrate AND iodine profiles at multiple locations.

Subtask 5.2. Authigenic minerals

Many workers, including us, have assumed that AOM dominates the output of carbon from most gas hydrate systems (especially those dominated by diffusion). According to this view, there is a relatively thin horizon at or near the seafloor referred to as the sulfate-methane transition; here, microbes use downward diffusing sulfate to consume upward migrating methane. This concept, if correct, is very important to gas hydrate studies because the sulfate gradient should relate to the top occurrence of gas hydrate in sediment (nb. we recognize that this postulated relationship is complicated because of several factors).

Initially, the main purpose of this subtask was to establish average SMT depths above gas hydrate systems using authigenic minerals (calcite, aragonite and barite). These minerals precipitate at or near the SMT because of changes in

pore water chemistry induced by AOM. Hence, although the depth of the SMT may migrate over short time intervals, authigenic minerals provide a means to assess the average depth over longer time intervals. We have generated a series of authigenic mineral profiles above gas hydrate systems. In most cases, there are obvious carbonate and barite “fronts” that mark the average depth of the SMT (e.g., Snyder et al., 2007).

More recently, several authors have challenged the notion that pore water sulfate profiles can be used to establish upward methane fluxes (Kastner et al., 2008). The primary grounds for this argumentation comes from pore water alkalinity and carbon isotope data, which show high concentrations of relatively ^{13}C -rich bicarbonate across the SMT. We believe this alternative view is fundamentally flawed because a deep flux of ^{13}C -rich bicarbonate into the SMT has been omitted (Dickens and Snyder, 2009). We have now generated carbon isotope profiles of inorganic and organic carbon at some of our sites, and are collecting additional relevant data from the Sea of Japan.

Organic carbon results from Site 1230 on the Peru Margin are most intriguing. The organic carbon content of sediment in the upper 30 m ranges between 2 and 8%; it has a $\delta^{13}\text{C}$ composition between -20 and -22 per mil. These values are consistent with limited earlier work at this location and emphasize a crucial point relevant to gas hydrate investigations and our numerical modeling. The sulfate-methane transition (SMT) at Site 1230 is characterized by pore water with bicarbonate at extremely high concentrations (50 mM) and unusually enriched in ^{13}C for shallow sediment above gas hydrate ($\delta^{13}\text{C} = -13$ per mil).

According to arguments by Kastner et al. (2008), high concentrations of ^{13}C -rich bicarbonate at the SMT above gas hydrate systems signifies sulfate reduction of solid organic carbon, such that anaerobic oxidation of methane rising from below is relatively minor. However, at Site 1230, there is no possible mechanism to convert solid organic carbon with a $\delta^{13}\text{C}$ of -20 to -22 per mil into bicarbonate at the SMT with a $\delta^{13}\text{C} = -13$ per mil via organoclastic sulfate reduction. On the other hand, we specifically selected Site 1230 because it has a very high upward flux of bicarbonate produced by methanogenesis in deeper sediment. As we have suggested previously, the extremely ^{13}C -rich enriched bicarbonate at the SMT at Site 1230 is entirely predicted once this deep flux is included.

Glen Snyder presented the above work and that at other sites at the DOE workshop in Atlanta (January, 2010). As a good summary, fluxes of dissolved carbon nicely balance across the SMT at multiple “gas hydrate” sites with very different characteristics but only if AOM dominates methane output AND a deep bicarbonate flux is included. Moreover, the wide range in $\delta^{13}\text{C}$ of bicarbonate at the SMT above gas hydrate systems is explained by the mixing of bicarbonate from AOM and bicarbonate rising from depth. Lastly, this concept naturally arises

in our numerical modeling efforts for gas hydrate formation when we incorporate a more complete carbon cycle (i.e., methanogenesis produces 13C-depleted methane and 13C-rich bicarbonate; Subtask 6.8).

Additional Subtask

After discussions with Carolyn Ruppel at the DOE workshop in Atlanta, Glen Snyder and Andrew Hunt (USGS) are developing methods to collect and analyze noble gases in pore waters and gas hydrates (following [Chaduteau et al., 2007](#)). He is presently testing the apparatus on a gas hydrate cruise in the Sea of Japan. The cruise is led by Ryo Matsumoto of the University of Tokyo and is sponsored by the Japanese Ministry of Economy, Trade and Industry. After the cruise, the apparatus and techniques will be used in the Gulf of Mexico with USGS.

The work follows concepts articulated over 10 years ago (Dickens and Kennedy, 2000) but not pursued because of sampling limitations. The basic idea is that gas hydrates, during formation, will fractionate the noble gases. Specifically, the heavier noble gases (Ar, Kr, and especially Xe) can fit into gas hydrate lattices, whereas the lighter noble gases (He and Ne) cannot. The relative abundances of the noble gases in pore waters and gas hydrates might therefore provide valuable information on the source and cycling time of fluids in gas hydrate systems (Winckler et al., 2002). The noble gases might further aid in the delineation of biogenic and thermogenic sources.

References

- Chaduteau, C., Fourré, E., Jean-Baptiste, P., Dapoigny, A., Baumier, D., and Charlou, J., 2007. A new method for quantitative analysis of helium isotopes in sediment pore-waters. Limnology and Oceanographic Methods, 5: 425-432.
- Dickens, G.R., and Kennedy, B. M., 2000. Noble gases in methane hydrate from the Blake Ridge. Proceedings of the Ocean Drilling Program, 164.
- Dickens, G.R. and Snyder, G., 2009. Interpreting upward methane flux. Fire in the Ice, Winter, 7-10
- Kastner, M., Torres, M., Solomon, E., and Spivack, A. J., 2008. Marine pore fluid profiles of dissolved sulfate: do they reflect in situ methane fluxes? Fire in the Ice, Summer, 6-8
- Winckler, G., Aeschbach-Hertig, W., Holocher, J., Kipfer, R., Levin, I., Poss, C., Rehder, G., Suess, E., and Schlosser, P., 2002. Noble gas and radiocarbon in natural gas hydrates: Geophysical Research Letters, v. 29: 4.

Task 6: Numerical Models for Quantification of Hydrate and Free Gas Accumulations

Subtask 6.3. Compositional Effect on BSR, Synthetic Seismic Response

Guangsheng Gu

(1) Hydrate distribution and seismic response due to multiple gas components

In this subtask, we have established the ability to generate synthetic seismogram with Ricker wavelets on some cases of hydrate/gas transition.

From the work we have finished, we can find out existence of another gas component in marine hydrate system, can affect the hydrate and gas distribution greatly. As an example, in a $\text{CH}_4\text{-C}_3\text{H}_8\text{-H}_2\text{O}$ hydrate system, there can exist a transition region in which Aq, H (sII) and V can co-exist, and S_H and S_V can change gradually (Fig. 6.3.1.). The transition zone can be as thick as 300 m. The p-wave velocity V_p , can vary gradually throughout this transition zone (Fig. 6.3.2).

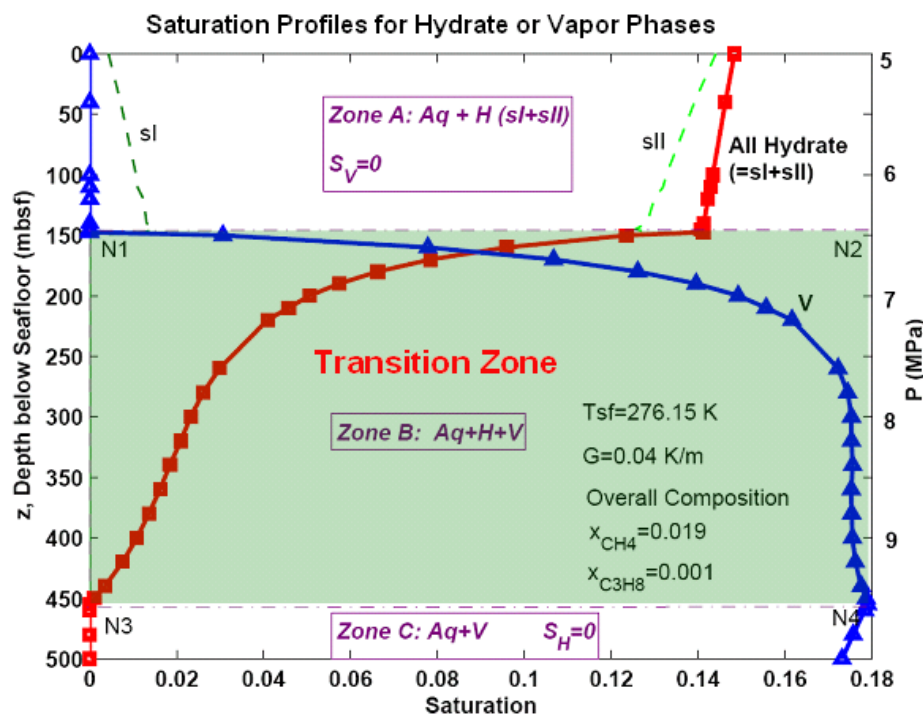


Figure 6.3.1. An example calculation of a $\text{CH}_4\text{-C}_3\text{H}_8\text{-H}_2\text{O}$ System (water-free propane molar fraction is 0.05; Overall composition $x_{\text{CH}_4}=0.019$, $x_{\text{C}_3\text{H}_8}=0.001$, $x_{\text{H}_2\text{O}}=0.98$).

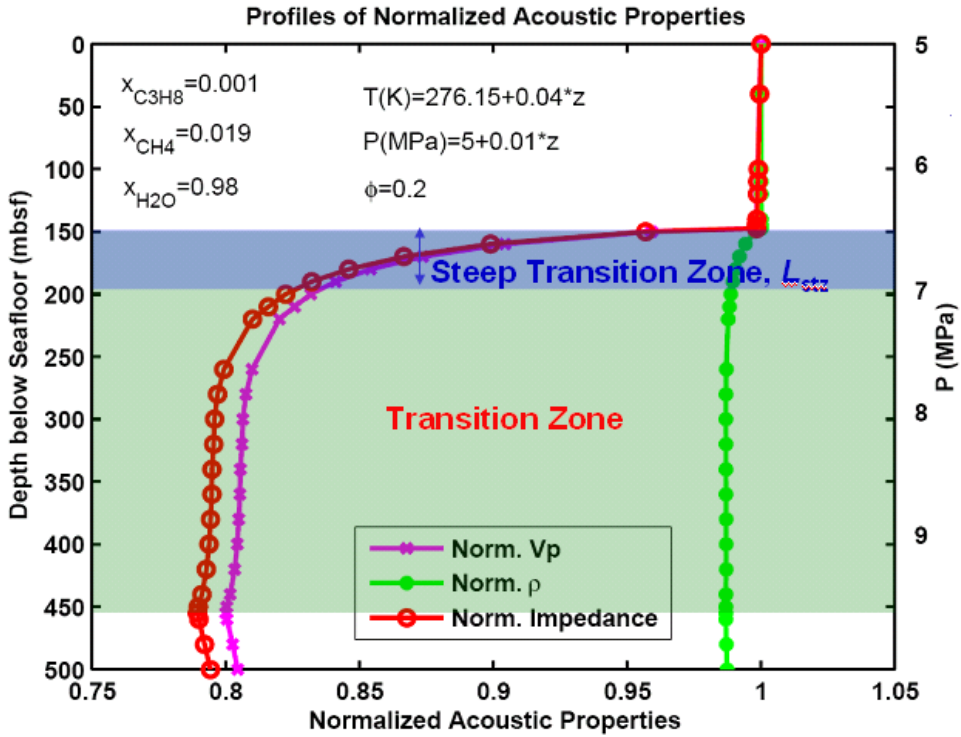


Figure 6.3.2. An example calculation of a $\text{CH}_4\text{-C}_3\text{H}_8\text{-H}_2\text{O}$ System (Profiles of Normalized Acoustic Properties of the $\text{CH}_4\text{-C}_3\text{H}_8\text{-H}_2\text{O}$ Hydrate System. Impedance $Z = \rho V_p$. Data are normalized so that at seafloor the value is 1).

By simplification, we can have two different types of V_p profiles from seafloor to deeper sediment shown in Fig. 6.3.3 – 6.3.4. There impulse responses are also shown in these figures. We can see that the seismic response, at Base of GHSZ (BGHSZ) for pure methane hydrate system (abrupt V_p change), the amplitude of reflection at BGHSZ is in the similar order of magnitude of that at seafloor (Fig. 6.3.3.).

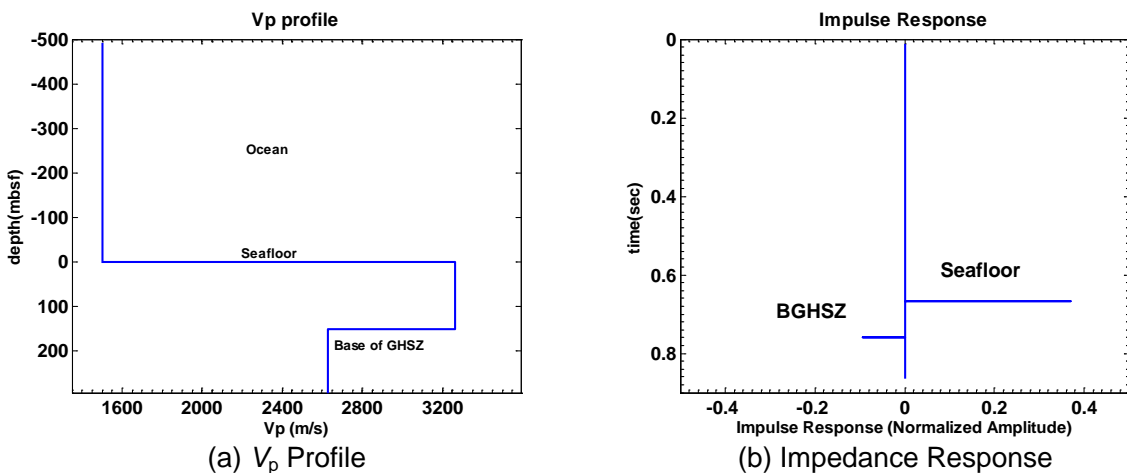
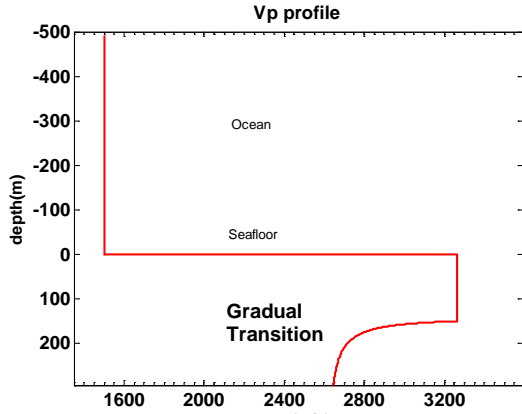
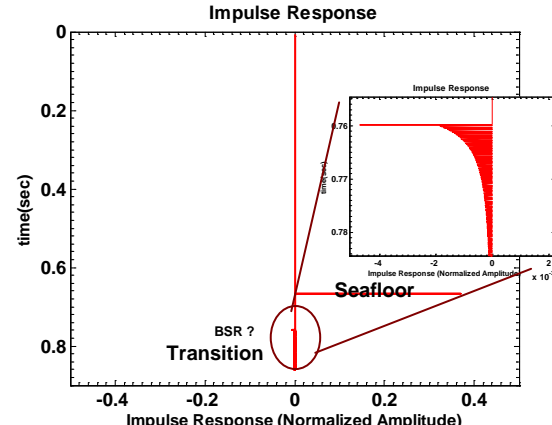


Figure 6.3.3. Abrupt V_p Change System: V_p Profile and Impedance Response

However, in a mixed hydrate system, the V_p profile varies gradually at hydrate/gas transition zone, their impulse response at this gradual transition zone, is much weaker than that at seafloor (Fig. 6.3.4.), though not zero.



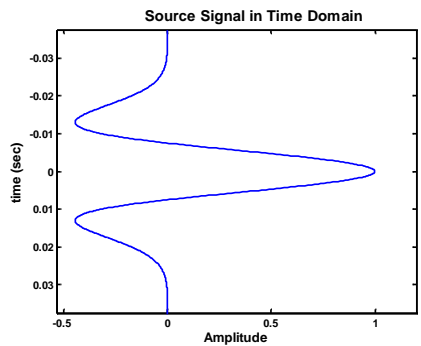
(a) V_p Profile



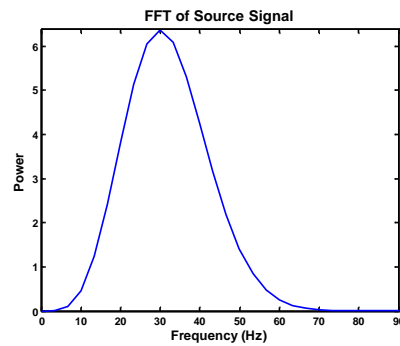
(b) Impedance Response

Figure 6.3.4. Mixed-hydrate System (Graduate V_p Change):
 V_p Profile and Impedance Response

Some certain Ricker wavelets are used to 1D synthetic seismic profile. A Ricker wavelet has a smooth power spectrum curve, with a peak frequency (Fig. 6.3.5). They are widely used in seismic simulators. In exploration seismic simulation, the peak frequency is mostly within a range from 10 to 100 Hz, and 30 Hz is a typical frequency.



(a) Source Signal in Time Domain



(b) Power Spectrum of Source Signal

Figure 6.3.5. Example of Source Signal: Ricker Wavelet (Here Peak Frequency: 30 Hz)

By using Ricker wavelets, with frequency from 10 to 100 Hz, we obtained the synthetic seismogram (Fig. 6.3.6.), both for that from a step change V_p profile (i.e., for pure methane hydrate system), and for that from a gradual transition zone. For the same thickness of the steep transition zone (shown in Fig. 6.3.2.) L_{stz} , different peak frequencies are used; for each wavelet with a certain peak

frequency, the characteristic wavelength is denoted as λ . The thickness ratio L_{stz}/λ are calculated. The seismograms are shown in Fig. 6.3.6.

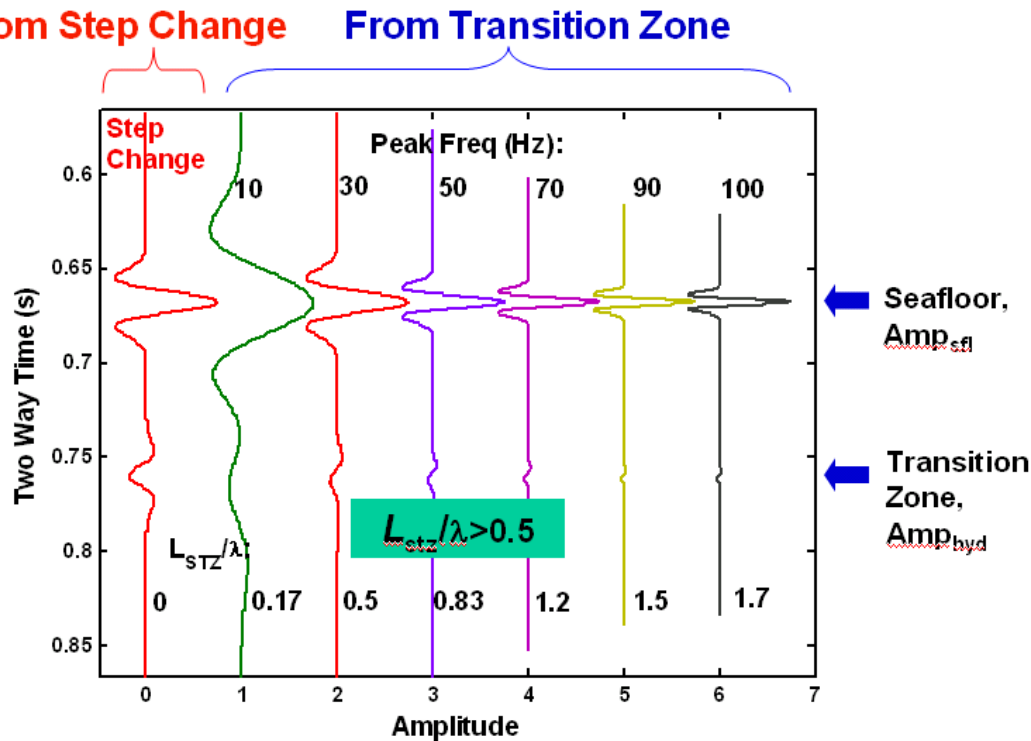


Figure 6.3.6. Reflection as a Function of L_{stz}/λ .

To quantitatively understand the seismic response, the amplitude ratio, Ratio of Amplitude at Hydrate/Gas Transition, to that at Seafloor, $A_{\text{Hd}\text{r}}/A_{\text{sfl}}$, is defined. If $A_{\text{Hd}\text{r}}/A_{\text{sfl}} \leq 0.1$, the reflection will be called a “weak reflection” (i.e., weak BSR). The relationship between $A_{\text{Hd}\text{r}}/A_{\text{sfl}}$ and thickness ratio L_{stz}/λ is plotted in Fig. 6.3.7. We can find out both qualitatively (in Fig. 6.3.6.) and quantitatively (in Fig. 6.3.7.) that:

If $L_{\text{stz}}/\lambda > 0.5$, then $A_{\text{Hd}\text{r}}/A_{\text{sfl}} \leq 0.1$, i.e., a weak reflection will be observed.

In Fig. 6.3.7., $A_{\text{Hd}\text{r}}/A_{\text{sfl}} \leq 0.1$ refers to that peak frequency is higher than 30 Hz (roughly). But 30 Hz is a typical frequency. Therefore, if a xed-hydrate transition zone exists, it's possible to observe a “weak BSR”.

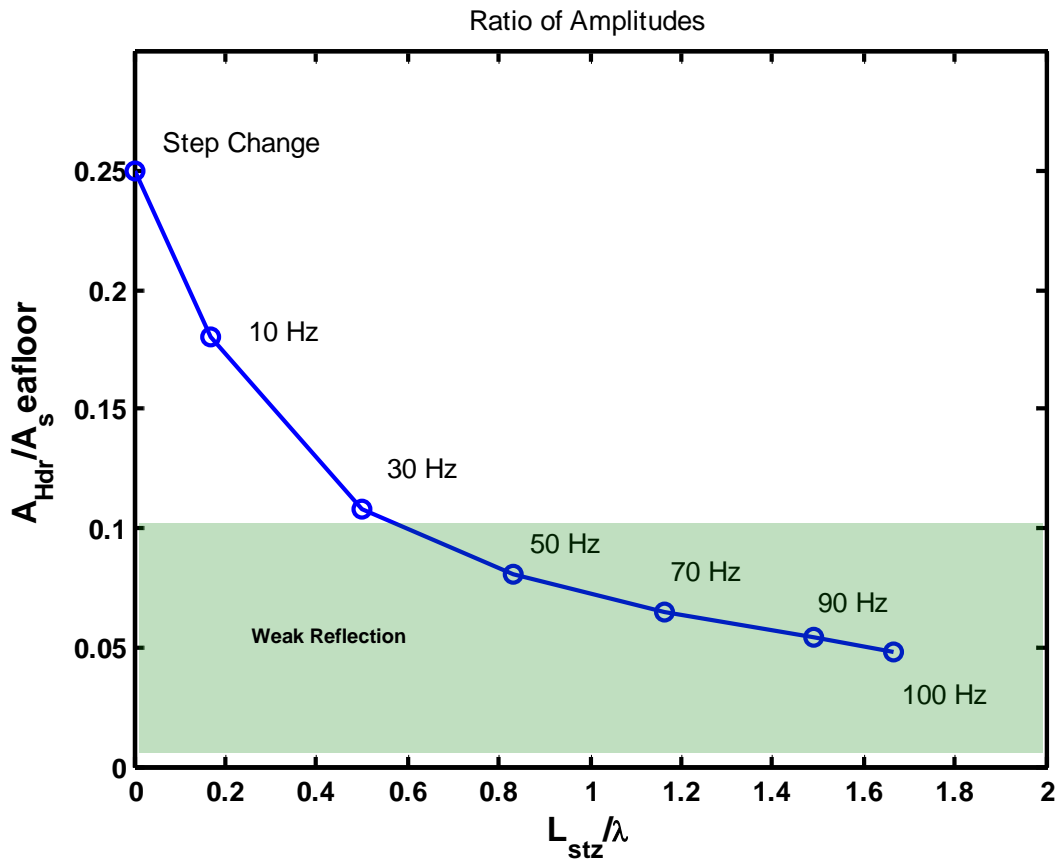


Figure 6.3.7. Amplitude Ratio as a Function of L_{stz}/λ .
 (The Ratio of Amplitude at Hydrate/Gas Transition, to that at Seafloor, $A_{Hd\bar{r}}/A_{s\ seafloor}$).
 If $A_{Hd\bar{r}}/A_{s\ seafloor} \leq 0.1$, the reflection is called a “weak reflection”, as shown in the shadowed region. The peak frequency for each point is also labeled.

(2) flash calculation for hydrate/free gas distribution

From the work we have finished, we have found that existence of another gas component in marine hydrate system can affect the hydrate and gas distribution greatly. These results are encouraging for further simulation. A manuscript on compositional effect based on these preliminary results is in progress.

We are trying to develop a code to simulate the compositional effects under seafloor. There are two important but challenging steps:

(1) Do flash calculation for a 4-phase, 3-component system. 4 phases include: Gas (or Vapor, G or V), Aqueous (Aq), Hydrate structure I (sI), Hydrate structure II (sII). In some cases, we know that there are only 3 phases, so it can be reduced to a 3-phase system. However, sometimes a liquid hydratcarbon (Liquid, L), may be involved, and it'll be a 5-phase system. 3 components include: water,

methane, and another heavier gas component (e.g., propane, ethane, or CO₂, etc.).

(2) A diffusion and convection model for multi-phase and multi-component systems. The transport model will include diffusion and convection of methane, and another heavier gas component, within one phase or among different phases. Different geothermal gradient and pressure distribution will be considered.

Flash calculation model

Since the multi-phase, multi-component flash calculation is challenging but important in this work, we are trying to apply some good flash calculation model and algorithms. The following is a possible flash model (M. L. Michelsen, 2007).

In a F-phase, C-component system, use phase F as the reference phase. In equilibrium we have:

$$y_{ij}\hat{\varphi}_{ij} = y_{iF}\hat{\varphi}_{iF}, \quad i=1,2,\dots,C; \quad j=1,2,\dots,F-1 \quad (1)$$

y_{ij} --- composition of component i , in phase j

$\hat{\varphi}_{ij}$ --- fugacity coefficients of component i , in phase j

The material balance equation for component i is:

$$\sum_{j=1}^F \beta_j y_{ij} = z_i, \quad i=1,2,\dots,C \quad (2)$$

β_j --- mole fraction of phase j with respect to overall material amount

z_i --- overall material amount of component i in the system

The mole fractions β_j satisfy a normalization property:

$$\sum_{j=1}^F \beta_j = 1$$

or:

$$\beta_F = 1 - \sum_{j=1}^{F-1} \beta_j \quad (3)$$

Substitute Eq. 3 into Eq. 2, we have the material balance as:

$$y_{iF} + \sum_{j=1}^{F-1} \beta_j (y_{ij} - y_{iF}) = z_i \quad (4)$$

Define K-factor:

$$K_{ij} = y_{ij} / y_{iF} = \hat{\rho}_{iF} / \hat{\rho}_{ij} \quad (5)$$

Substitute Eq.5 into Eq.3:

$$y_{iF} \left(1 + \sum_{l=1}^{F-1} \beta_l (K_{il} - 1) \right) = z_i \quad (6)$$

or :

$$y_{iF} = \frac{z_i}{1 + \sum_{l=1}^{F-1} \beta_l (K_{il} - 1)} \quad (7)$$

and

$$y_{ij} = \frac{z_i K_{ij}}{1 + \sum_{l=1}^{F-1} \beta_l (K_{il} - 1)} \quad (8)$$

From Eq.3~Eq.8, we can obtain $F-1$ equations with $F-1$ unknown, β_j , as:

$$\sum_{i=1}^C \frac{K_{ij} - 1}{\sum_{l=1}^{F-1} \beta_l (K_{il} - 1)} = 0, \quad j=1,2,\dots,F-1 \quad (9)$$

From properties of phases and components, fugacity coefficients, K_{ij} can be obtained from Eq.5; then, phase fractions β_j can be estimated by solving Equation set 9; finally, phase compositions y_{ij} , will be easily obtained from Eq.7 and Eq.8.

Normally, Equation set 9 can be solved by Newton method. However, many situations happen at which adjustments are required. For example, phase fraction β_j may be negative or greater than 1. So some constraints should be applied as:

$$1 \geq \beta_j \geq 0, \quad j=1,2,\dots,F-1 \quad (10)$$

Equation set 9 also may be difficult to converge.

To solve Equation set 9, a better method is as following.

Define an objective function

$$Q(\beta) = \sum_{j=1}^F \beta_j - \sum_{i=1}^C z_i \ln E_i , \quad (11)$$

where $E_i = \sum_{k=1}^F (\beta_k / \hat{\phi}_{ik})$, (12) .

It can be proved that in this case, a solution β_j will minimize Q while subjecting to Eq.14-15. So the problem becomes an optimization problem:

$$\min_{\beta \in R^F} Q(\beta) \quad (13)$$

$$\text{subject to: } \beta_j \geq 0, \quad j=1,2,\dots,F \quad (14)$$

$$\sum_{j=1}^F \beta_j = 1 \quad (15)$$

The solution is given by

$$\begin{cases} \frac{\partial Q}{\partial \beta_j} = 0 & : \beta_j > 0 \\ \frac{\partial Q}{\partial \beta_j} > 0 & : \beta_j = 0 \end{cases} \quad (16)$$

The gradient of Q is

$$g_j = \frac{\partial Q}{\partial \beta_j} = 1 - \sum_{i=1}^C \frac{z_i}{E_i} \frac{1}{\hat{\phi}_{ij}} \quad (17)$$

At solution, the mole fraction can be calculated by:

$$y_{ij} = \frac{z_i}{E_i} \frac{1}{\hat{\phi}_{ij}} \quad (18)$$

Numerical code for a 4-phase, 3-component system is in progress now. More results may be available later.

Subtask 6.4. Blanking and chaotic zones due to hydrate distribution.
Guangsheng Gu

(1) Sediment Acoustic impedance analysis:

We have started working on acoustic velocity profiles in different types of sediment layers. Due to hydrate accumulation, the velocity in different types of sediment layers can become similar with each other.

Geological settings:

We set several horizontal layers with different properties, from seafloor to deeper sediment. These layers are in 2 types: sandstone or clay/shale. Sandstone layers have higher porosity (20%~30%), and shale layers with some porosity values varying with depth (Fig. 6.4.1). Assume hydrate saturation increases gradually. Then we estimated the V_p density, and seismic impedance profiles of these two different types of layers, and made comparison between them.

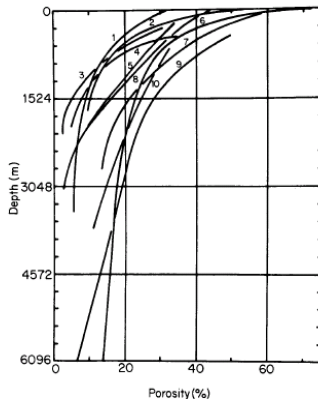


Fig 2.2 Porosity of clay/shale as a function of depth [Jenyon 1990 (Magara 1980)]

Figure 6.4.1. Porosity of Clay/shale as a function of depth [Jenyon 1990, Hirasaki, lecture note, 2006].

Parameters:

Table 6.4.1: Acoustic properties of components

Component	V_p (m/s)	ρ (kg/m ³)
Sea Water (w)	1500	1030
Hydrate (H)	3300	900
Mineral1 (m1, sandstone)	2000~4000	2500

Mineral2 (m2, shale)	2400	2600
---------------------------------------	------	------

Table 6.4.2: other parameters

Parameter	Value	
Porosity1 (in sandstone layer)	0.2 ~ 0.3	
Porosity2 (in shale layer)	Up: 0.6; Low: 0.2~0.4	
Sh	0~1	

The ranges of porosity were obtained from Hirasaki (lecture note, 2006), Jenyon (2006), Magara (1980); and those of acoustic velocities from W.J. Winters and W.F. Waite (2007).

Equations:

Estimation of average velocity is via a revised form of the Time-average Equation (Pearson *et al.*, 1983).:

$$\frac{1}{V_p} = \frac{\phi(1 - S_H - S_V)}{V_w} + \frac{\phi S_H}{V_H} + \frac{(1 - \phi)}{V_m} + \frac{\phi S_V}{V_V}$$

V_p --- average compressional velocity of the sediment;

V_H --- compressional velocity of the pure hydrate;

V_w --- compressional velocity of the fluid;

V_m --- compressional velocity of the mineral;

ϕ --- porosity (as a fraction);

S_H --- Hydrate saturation

S_V --- Vapor (Gas) saturation

Average density is estimated via:

$$\bar{\rho} = (1 - \phi)\rho_m + \phi \sum_i S_i \rho_i$$

phase $i = w, H, V$.

Impedance is: $Z = \rho V_p$

Preliminary result:

The preliminary results show that the acoustic impedance of sand layer, at $S_h=0$, is possible to be lower than that of a shale layer; then when hydrate saturation S_h increases, it's possible for impedance of sand layer to increase to higher values than that of a shale layer. In these situations, it's possible that a blanking can be achieved during the hydrate accumulation process. (Figures Figure 6.4.1 – 6.4.2.) .

As an example, in Figure 6.4.1, if S_{h_sand} (hydrate saturation in sand layer) increases to around 0.23, the impedance would be comparable to that in clay layer. (Assume $S_{h_clay} = 0$, since hydrate saturation in clay layer is often very close to 0.)

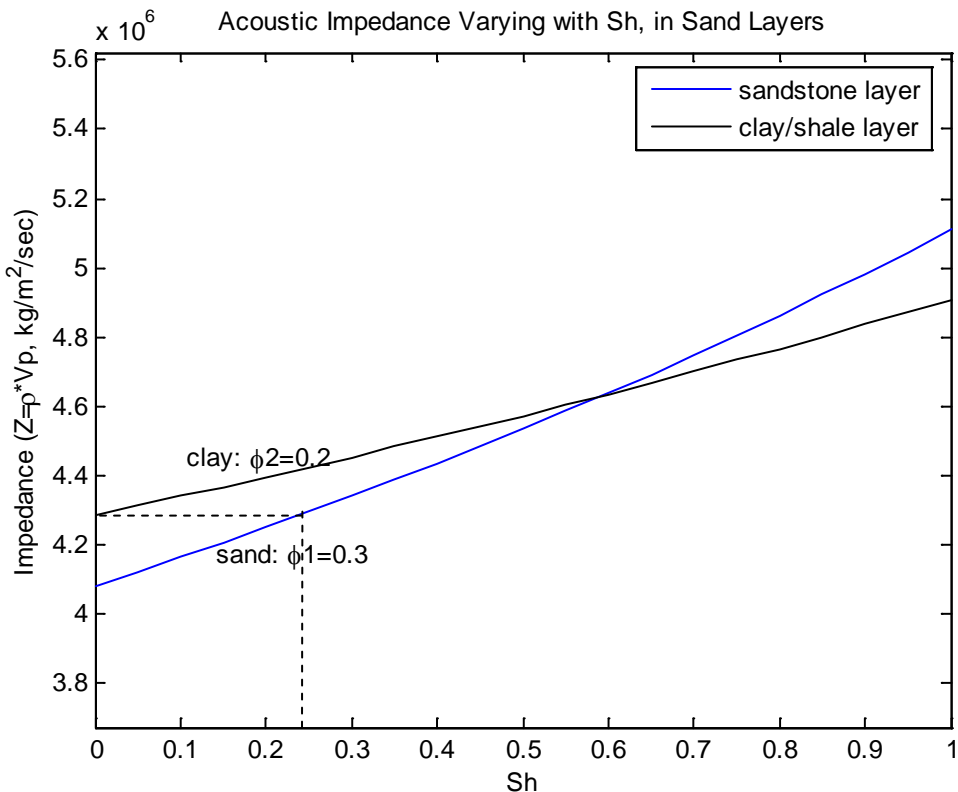


Figure 6.4.1: Impedance increase of sandstone layer due to S_h increase

Parameters: $\phi_1=0.3$; $\phi_2=0.2$; $V_{p_sand}=2300$ m/s; $V_{p_clay}=2000$ m/s. If S_{h_sand} (hydrate saturation in sand layer) increases to around 0.23, the impedance would be comparable to that in clay layer. Assume $S_{h_clay} = 0$, since hydrate saturation in clay layer is often very close to 0.

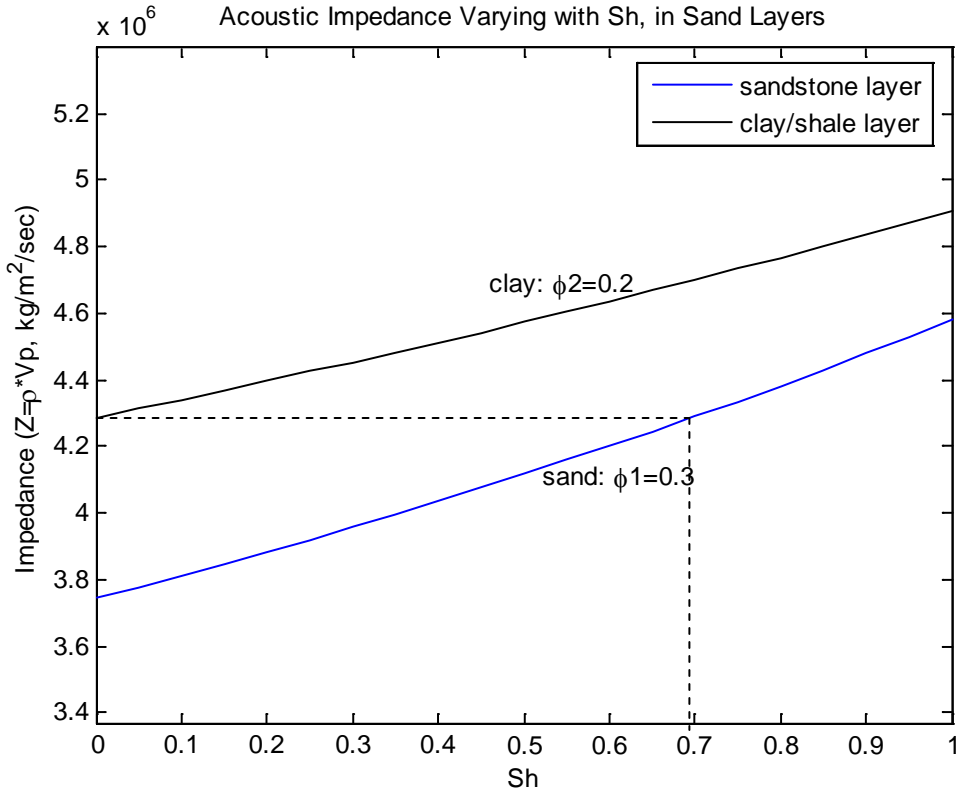


Figure 6.4.2: Impedance increase of sandstone layer due to S_h increase

Parameters: $\phi_1=0.3$; $\phi_2=0.3$; $V_{p_sand}=2000$ m/s; $V_{p_clay}=2000$ m/s. If S_{h_sand} (hydrate saturation in sand layer) increases to around 0.69, the impedance would be comparable to that in clay layer. Assume $S_{h_clay} = 0$, since hydrate saturation in clay layer is often very close to 0.

(2) 2D hydrate / free gas distribution simulation for seismic features:

To study why some seismic features exist, and to understand the mechanism and evolution process, we did some forward modeling on 2D hydrate /free gas distribution simulation.

We revised the 2D code (originally developed by Dr. Gaurav Bhatnagar in 2008) to deal with complex lithologic structures.

Mathematical model:

Water balance:

$$\frac{\partial}{\partial t} \left[\phi S_w c_w^l \rho_w + \phi S_h c_w^h \rho_h \right] + \nabla \cdot \left[\phi S_w c_w^l \rho_w \mathbf{v}_w + \phi S_h c_w^h \rho_h \mathbf{v}_s \right] = 0$$

Sediment balance:

$$\frac{\partial}{\partial t} [(1 - \phi) \rho_s] + \nabla \cdot [(1 - \phi) \rho_s \mathbf{v}_s] = 0$$

Organic balance:

$$\frac{\partial}{\partial t} [(1 - \phi) \rho_s \alpha] + \nabla \cdot [(1 - \phi) \rho_s \mathbf{v}_s \alpha] = -\rho_s \lambda (1 - \phi) \alpha$$

Methane balance:

$$\begin{aligned} & \frac{\partial}{\partial t} \left[\phi S_w c_m^l \rho_w + \phi S_h c_m^h \rho_h + \phi S_g c_m^g \rho_g \right] + \\ & \nabla \cdot \left[\phi S_w c_m^l \rho_w \mathbf{v}_w + \phi S_h c_m^h \rho_h \mathbf{v}_s + \phi S_g c_m^g \rho_g \mathbf{v}_g \right] \\ & = \nabla \cdot \left[\phi S_w D_m \rho_w \nabla c_m^l \right] + \frac{M_{CH_4}}{M_{org}} \rho_s \lambda (1 - \phi) \alpha \end{aligned}$$

where t is time, ϕ is porosity, S_j is saturation of phase j , c_i^j is the composition of component i in phase j , v_j is the velocity of phase j , ρ_j is density of phase j , λ is biogenic reaction constant, α is organic carbon content in sediment.

Darcy's law for water flux in a compacting medium (Bear, 1988)

$$S_w \phi (v_w - v_s) = -\frac{k k_{rw}}{\mu_w} \left(\frac{\partial p_w}{\partial z} - \rho_w g \right)$$

where v_w and v_s denote the velocity of water and sediment, respectively; k is the absolute permeability, k_{rw} is the relative permeability of water.

Absolute permeability of sediment is modeled as a power law function of porosity (Smith, 1971):

$$k = k_o (\phi / \phi_o)^4$$

where k_o and ϕ_o are permeability and porosity at time of deposition.

Water relative permeability model in the presence of gas hydrate is (Kleinberg et al., 2003):

$$k_{rw} = 1 - S_h^2 + \frac{2(1 - S_h)^2}{\ln(S_h)}$$

Water relative permeability model in the presence of free gas is (Bear, 1988):

$$k_{rw} = k_{rw}^0 (S_w^*)^4$$

where $S_w^* = \frac{S_w - S_{wr}}{1 - S_{wr}}$, and S_{wr} is the residual water saturation.

Capillary pressure (P_c) is the difference between gas and water pressure:

$$P_c = p_g - p_w$$

And it can be estimated that the saturation dependent capillary pressure is:

$$P_c(S_w) = P_{c,0}(S_w) \sqrt{\frac{k_o \phi}{\phi_o k}}$$

where $P_{c,0}(S_w) = P_{ce,0} S_w^{-1/n}$ is the capillary pressure curve at reference porosity ϕ_o and absolute permeability k_o , and $P_{ce,0}$ is the capillary entry pressure at ϕ_o and k_o .

Porosity-effective stress relationship is defined as (Rubey and Hubbert, 1959):

$$\phi = \phi_\infty + (\phi_0 - \phi_\infty) e^{-\frac{\sigma_v - p_w}{\sigma_\phi}}$$

Lithostatic stress σ_v is a function of depth, densities and porosity:

$$\frac{\partial \sigma_v}{\partial z} = [(1 - \phi)\rho_s + \phi\rho_w] g$$

Let L_t denote the thickness of GHSZ, and

$$L_\phi = \frac{\sigma_\phi}{(1 - \phi_\infty)(\rho_s - \rho_f)g}$$

denote the characteristic length of sediment compaction.

Define normalized variables as:

$$\begin{aligned} \tilde{x} &= x / L_t, \quad \tilde{z} = z / L_t, \quad \tilde{t} = t / (L_t^2 / D_m), \\ \tilde{\alpha} &= \alpha / \alpha_0, \quad \tilde{v}_s = v_s / \dot{S}, \\ \tilde{\phi} &= \frac{\phi - \phi_\infty}{1 - \phi_\infty}, \quad \eta = \frac{\phi_0 - \phi_\infty}{1 - \phi_\infty}, \quad \gamma = \frac{1 - \phi_\infty}{\phi_\infty}, \end{aligned}$$

and concentration of methane in phase j , is normalized with respect to $c_{m,eqb}^l$:

$$\tilde{c}_m^j = c_m^j / c_{m,eqb}^l, \quad j = \text{liquid (l), hydrate (h), gas (g)}$$

Densities are normalized with respect to ρ_w :

$$\tilde{\rho}_j = \rho_j / \rho_w, j = \text{sediment } (s), h, g$$

And all stresses are normalized with respect to $\rho_w g L_t$:

$$\tilde{\sigma}_v = \frac{\sigma_v}{\rho_w g L_t}, \quad \tilde{p}_w = \frac{p_w}{\rho_w g L_t}, \quad \tilde{p}_g = \frac{p_g}{\rho_w g L_t}, \quad \tilde{P}_c = \frac{P_c}{\rho_w g L_t}$$

and dimensionless groups:

$$\begin{aligned} Pe_1 &= U_{f,sed} L_t / D_m, \quad Da = \lambda L_t^2 / D_m, \quad \beta = \alpha_0 / c_{m,eqb}^l \\ N_{sc} &= k_o \rho_w g / (\mu_w \dot{S}) \\ N_{t\phi} &= L_\phi / L_t = (\sigma_\phi / \rho_w g) / L_t \end{aligned}$$

By substituting the above variables and parameters, the equations can be changed into dimensionless form:

Water balance:

$$\begin{aligned} \frac{\partial}{\partial \tilde{t}} \left[\frac{1 + \gamma \tilde{\phi}}{\gamma} (S_w c_w^l + S_h c_w^h \tilde{\rho}_h) \right] + Pe_1 \left(\frac{1 + \gamma}{1 - \eta} \right) \frac{\partial}{\partial \tilde{z}} \left[\left\{ \left(\frac{1 + \gamma \tilde{\phi}}{\gamma} \right) S_w \tilde{v}_s - \right. \right. \\ N_{sc} \left(\frac{1 + \gamma}{\gamma} \right) \left(\frac{1 + \gamma \tilde{\phi}}{1 + \gamma \eta} \right)^8 k_{rw} \left(\frac{\partial \tilde{p}_w}{\partial \tilde{z}} - 1 \right) \left. \right\} c_w^l + \left(\frac{1 + \gamma \tilde{\phi}}{\gamma} \right) S_h \tilde{\rho}_h \tilde{v}_s c_w^h \left. \right] + \\ Pe_1 \left(\frac{1 + \gamma}{1 - \eta} \right) \frac{\partial}{\partial \tilde{x}} \left[-N_{sc} \left(\frac{1 + \gamma}{\gamma} \right) \left(\frac{1 + \gamma \tilde{\phi}}{1 + \gamma \eta} \right)^8 k_{rw} \frac{\partial \tilde{p}_w}{\partial \tilde{x}} c_w^l \right] = 0 \end{aligned}$$

Initial and boundary conditions are as the following:

$$\text{I.C. : } \tilde{p}_w(\tilde{z}, \tilde{x}, 0) = \frac{\rho_w g D_0 + \rho_w g z}{\rho_w g L_t} = \frac{D_0}{L_t} + \tilde{z} \quad (\text{hydrostatic pressure})$$

$$\text{B.C. (1): } \tilde{p}_w(0, \tilde{x}, \tilde{t}) = \frac{D_0}{L_t} \quad (\text{hydrostatic pressure})$$

$$\text{B.C. (2): } \frac{\partial \tilde{p}_w}{\partial \tilde{x}}(\tilde{z}, 0, \tilde{t}) = \frac{\partial \tilde{p}_w}{\partial \tilde{x}}(\tilde{z}, D_x, \tilde{t}) = 0 \quad (\text{no flow boundary at sides})$$

$$\text{B.C. (3): } \frac{\partial \tilde{p}_w}{\partial \tilde{z}}(D_z, \tilde{x}, \tilde{t}) = 1 \quad (\text{hydrostatic gradient})$$

where D_0 is seafloor depth; D_z and D_x are domain bottom position and width of the domain, respectively.

Sediment balance:

$$\frac{\partial}{\partial \tilde{t}} [1 - \tilde{\phi}] + \text{Pe}_1 \left(\frac{1 + \gamma}{1 - \eta} \right) \frac{\partial}{\partial \tilde{z}} [(1 - \tilde{\phi}) \tilde{v}_s] = 0$$

$$\text{I.C. : } \tilde{v}_s(\tilde{z}, \tilde{x}, 0) = \frac{1 - \eta}{1 - \tilde{\phi}}, \text{ (hydrostatic compaction)}$$

$$\text{B.C.: } \tilde{v}_s(0, \tilde{x}, \tilde{t}) = 1$$

Organic balance:

$$\frac{\partial}{\partial \tilde{t}} [(1 - \tilde{\phi}) \tilde{\alpha}] + \text{Pe}_1 \left(\frac{1 + \gamma}{1 - \eta} \right) \frac{\partial}{\partial \tilde{z}} [(1 - \tilde{\phi}) \tilde{v}_s \tilde{\alpha}] = -\text{Da} (1 - \tilde{\phi}) \tilde{\alpha}$$

$$\text{I.C.: } \tilde{\alpha}(\tilde{z}, \tilde{x}, 0) = 0$$

$$\text{B.C. : } \tilde{\alpha}(0, \tilde{x}, \tilde{t}) = 1$$

Methane balance:

$$\begin{aligned} & \frac{\partial}{\partial \tilde{t}} \left[\frac{1 + \gamma \tilde{\phi}}{\gamma} (S_w \tilde{c}_m^l + S_h \tilde{c}_m^h \tilde{\rho}_h + S_g \tilde{c}_m^g \tilde{\rho}_g) \right] + \text{Pe}_1 \left(\frac{1 + \gamma}{1 - \eta} \right) \\ & \frac{\partial}{\partial \tilde{z}} \left[\left\{ \left(\frac{1 + \gamma \tilde{\phi}}{\gamma} \right) S_w \tilde{v}_s - N_{sc} \left(\frac{1 + \gamma}{\gamma} \right) \left(\frac{1 + \gamma \tilde{\phi}}{1 + \gamma \eta} \right)^8 k_{rw} \left(\frac{\partial \tilde{p}_w}{\partial \tilde{z}} - 1 \right) \right\} \tilde{c}_m^l + \right. \\ & \left. \left\{ \left(\frac{1 + \gamma \tilde{\phi}}{\gamma} \right) S_g \tilde{v}_s - N_{sc} \left(\frac{1 + \gamma}{\gamma} \right) \left(\frac{1 + \gamma \tilde{\phi}}{1 + \gamma \eta} \right)^8 k_{rg} \left(\frac{\mu_w}{\mu_g} \right) \left(\frac{\partial \tilde{p}_g}{\partial \tilde{z}} - \tilde{\rho}_g \right) \right\} \tilde{\rho}_g \tilde{c}_m^g + \right. \\ & \left. \left(\frac{1 + \gamma \tilde{\phi}}{\gamma} \right) S_h \tilde{c}_m^h \tilde{\rho}_h \tilde{v}_s \right] + \text{Pe}_1 \left(\frac{1 + \gamma}{1 - \eta} \right) \frac{\partial}{\partial \tilde{x}} \left[-N_{sc} \left(\frac{1 + \gamma}{\gamma} \right) \left(\frac{1 + \gamma \tilde{\phi}}{1 + \gamma \eta} \right)^8 k_{rw} \frac{\partial \tilde{p}_w}{\partial \tilde{x}} \tilde{c}_m^l - \right. \\ & \left. N_{sc} \left(\frac{1 + \gamma}{\gamma} \right) \left(\frac{1 + \gamma \tilde{\phi}}{1 + \gamma \eta} \right)^4 k_{rg} \left(\frac{\mu_w}{\mu_g} \right) \frac{\partial \tilde{p}_g}{\partial \tilde{x}} \tilde{\rho}_g \tilde{c}_m^g \right] = \frac{\partial}{\partial \tilde{z}} \left[\frac{1 + \gamma \tilde{\phi}}{\gamma} S_w \frac{\partial \tilde{c}_m^l}{\partial \tilde{z}} \right] + \\ & \frac{\partial}{\partial \tilde{x}} \left[\frac{1 + \gamma \tilde{\phi}}{\gamma} S_w \frac{\partial \tilde{c}_m^l}{\partial \tilde{x}} \right] + \frac{M_{CH_4}}{M_{org}} \tilde{\rho}_s \text{Da} (1 - \tilde{\phi}) \tilde{\alpha} \beta \end{aligned}$$

I.C. and B.C.s are:

$$\text{I.C. : } \tilde{c}_m^l(\tilde{z}, \tilde{x}, 0) = 0$$

$$\text{B.C.(1) : } \tilde{c}_m^l(0, \tilde{x}, \tilde{t}) = 0$$

$$\text{B.C.(2)} : \frac{\partial \tilde{c}_m^l}{\partial \tilde{z}}(D_z, \tilde{x}, \tilde{t}) = \frac{\partial \tilde{c}_m^l}{\partial \tilde{x}}(\tilde{z}, 0, \tilde{t}) = \frac{\partial \tilde{c}_m^l}{\partial \tilde{x}}(\tilde{z}, D_x, \tilde{t}) = 0$$

Results:

Use reference absolute permeability at time of deposition $k_o = 1.6 \text{ mD}$. Set parameters as $N_{sc} = 100$, $Pe_1 = 0.1$, $Da = 1$, $N_{t\phi} = 1$.

Structure A: Only consider a dipping sand layer in the background shale layer.

Normalized horizontal (k_h) and vertical (k_v) permeability values are:

In shale layer: $k_{h1} = 1$, $k_{v1} = 0.5$;

In sand layer: $k_{h2} = k_{v2} = 100$.

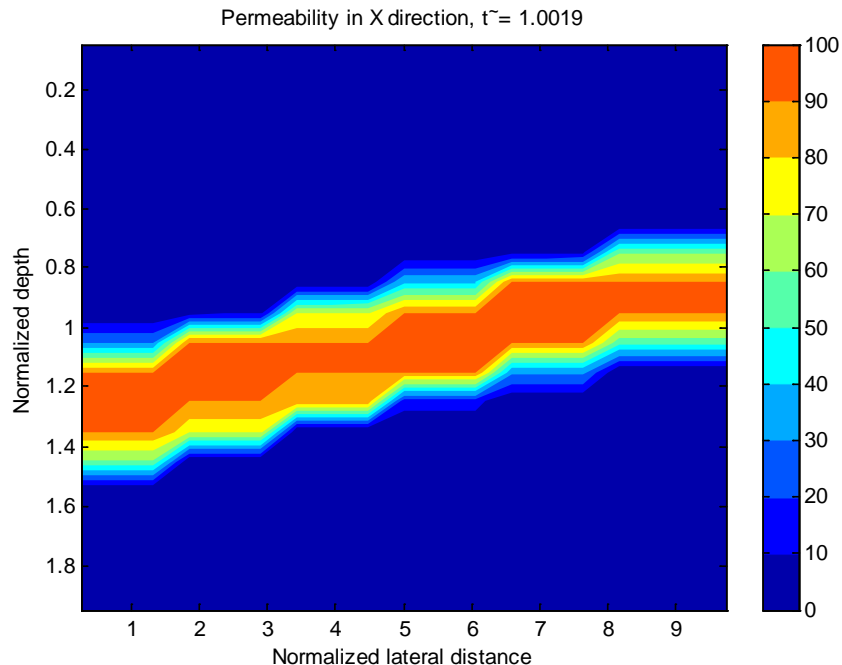


Figure 6.4.4: Lithology structure A

Structure evolution of the system:

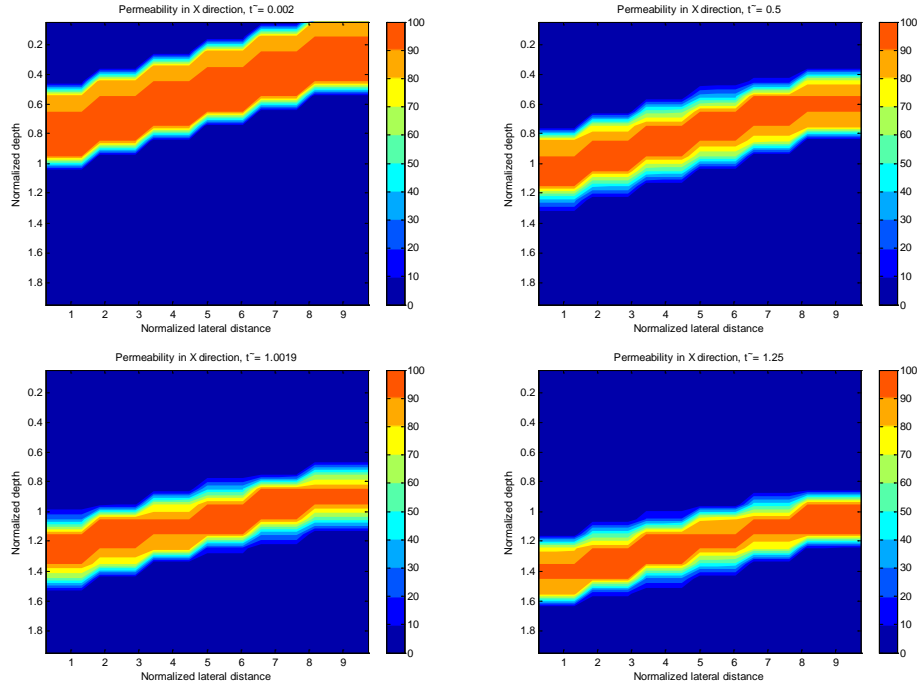


Figure 6.4.5: Lithology Structure Evolution
Normalized time = 0, 0.5, 1.0, 1.25.

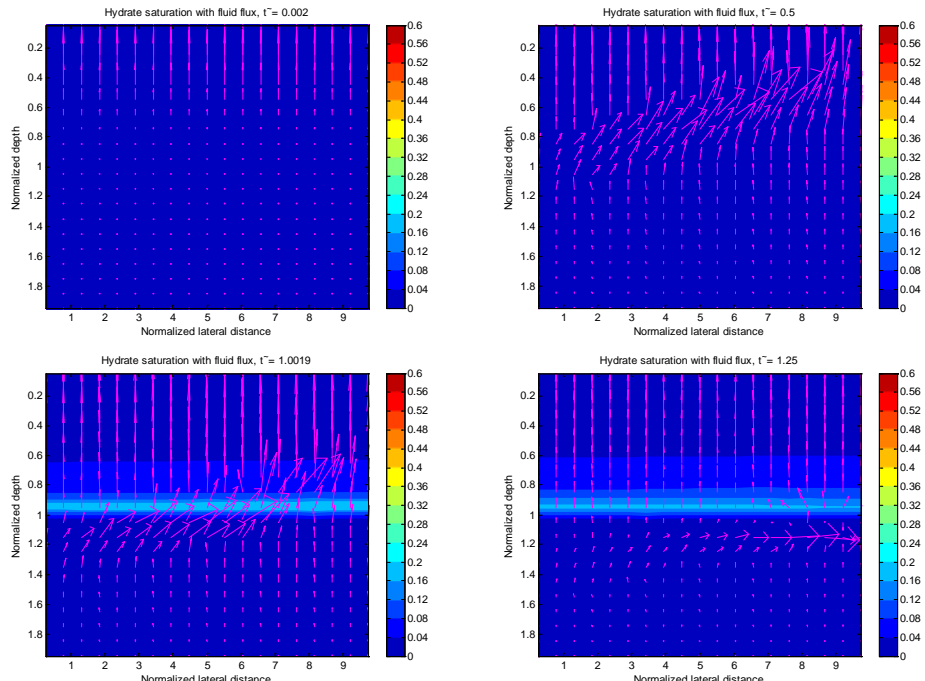


Figure 6.4.6: Hydrate Saturation (S_h) Evolution
Normalized time = 0, 0.5, 1.0, 1.25.

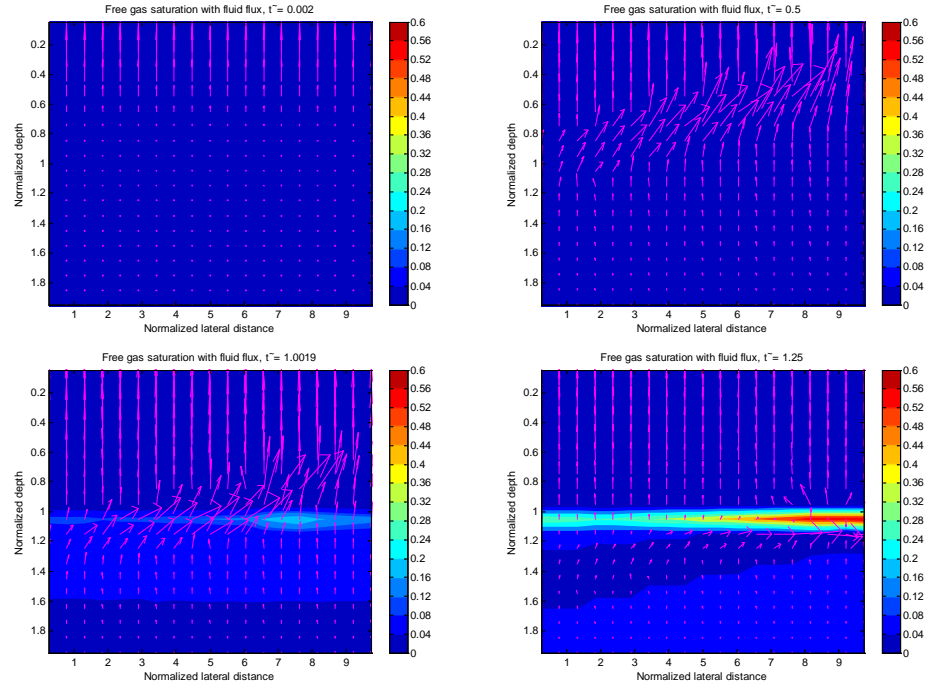


Figure 6.4.7: Free Gas Saturation (S_h) Evolution
Normalized time = 0, 0.5, 1.0, 1.25.

Structure B: Consider a dipping sand layer in the background shale layer, and some vertical fractures. Normalized horizontal (k_h) and vertical (k_v) permeability values are:

In shale layer: $k_{h1} = 1$, $k_{v1} = 0.5$;

In sand layer: $k_{h2} = k_{v2} = 100$;

In fracture: $k_{h3} = k_{v3} = 80$.

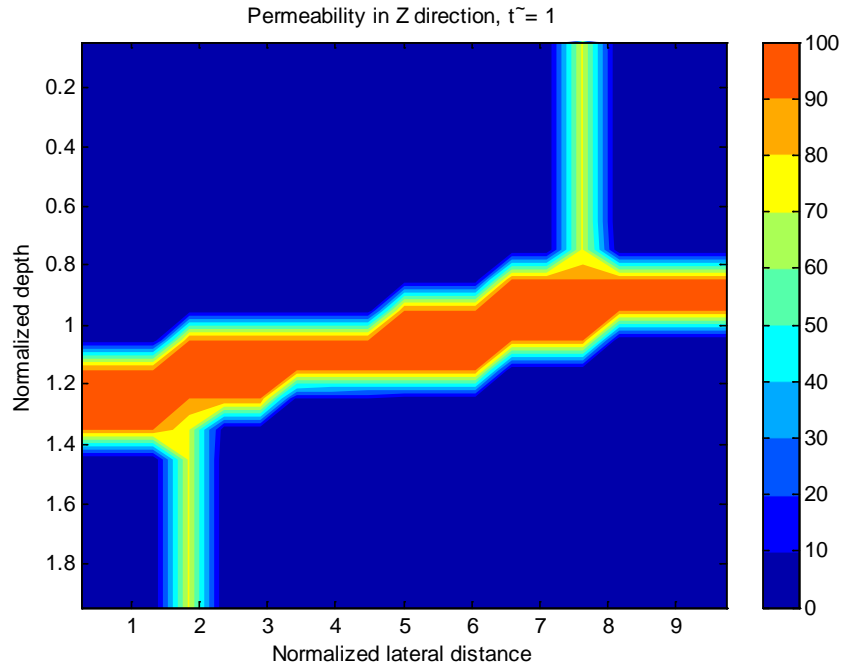


Figure 6.4.8: Lithology structure B

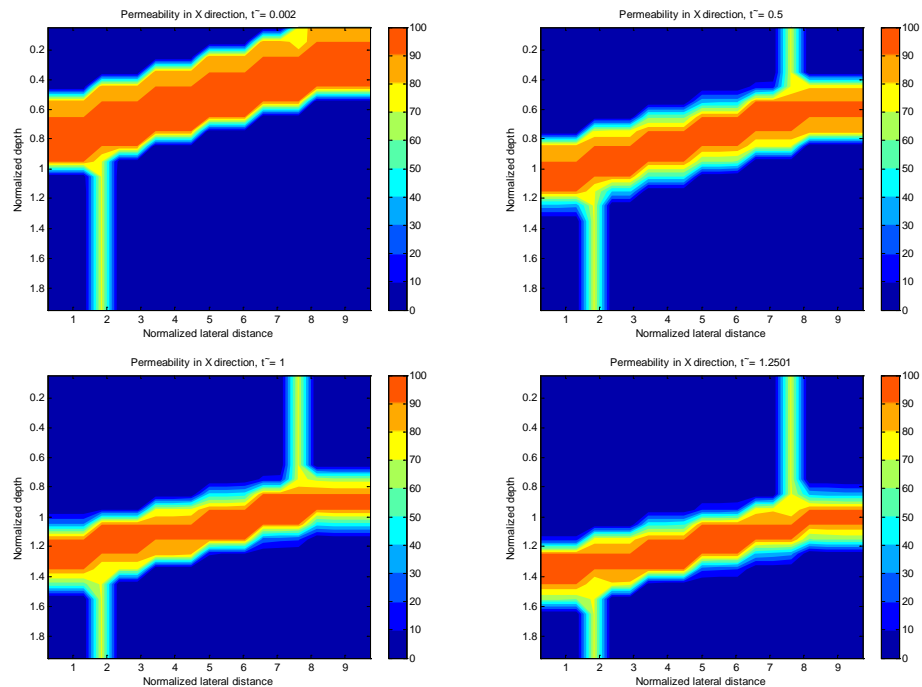
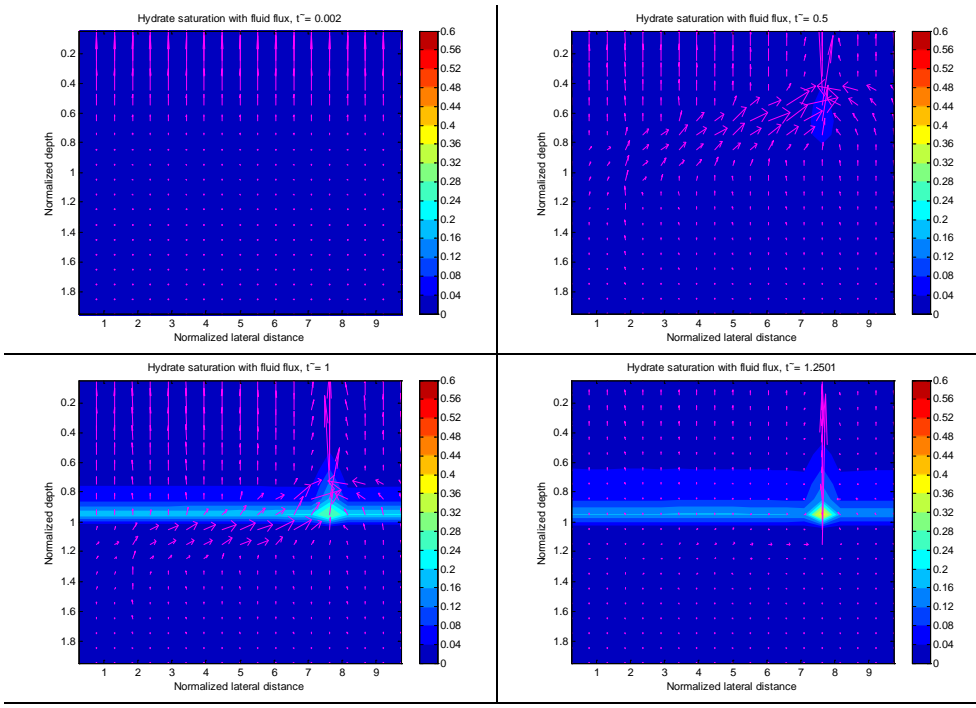
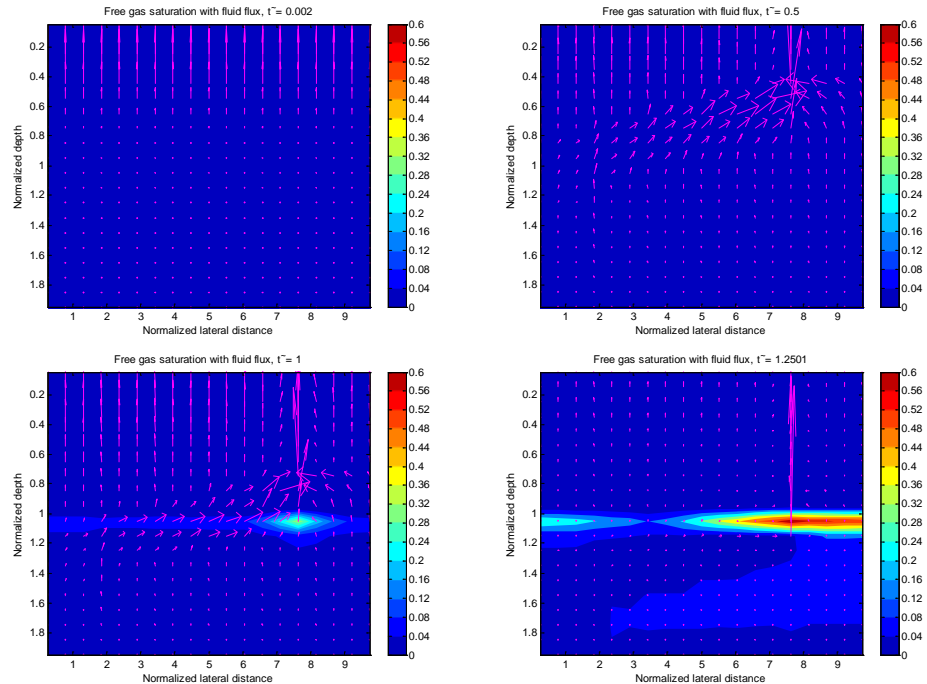


Figure 6.4.9: Lithology Structure Evolution
Normalized time = 0, 0.5, 1.0, 1.25.



**Figure 6.4.10: Hydrate Saturation (S_h) Evolution
Normalized time = 0, 0.5, 1.0, 1.25.**



**Figure 6.4.11: Free Gas Saturation (S_g) Evolution
Normalized time = 0, 0.5, 1.0, 1.25.**

Conclusion:

The above figures show the evolution of lithologic structure and hydrate/free gas saturation in the system. These preliminary results demonstrate the ability of the code to deal with simple heterogeneous structures, and to study the evolution of the hydrate / free gas distribution.

In next step, we'll develop more abilities for the code to deal with more complex structures, and to deal with gas – sediment interaction, to simulate some interested seismic cases including chimney, blanking zone, chaotic zone, and so on. Also we'll study the acoustic impedance evolution and their effects on seismic detection.

Academic Activity:

1. Effect of Hydrocarbon Components on Hydrate/Gas Distribution and BSR, Guangsheng Gu, Priyank Jaiswal, Walter Chapman, George J. Hirasaki, SPE Gulf Coast Section, Regional Student Paper Contest, Houston, TX, April 17-18, 2009, (oral presentation).
2. Massive Methane Hydrate in Sediments to Cause the Paleocene/Eocene Thermal Maximum, Guangsheng Gu, Gerald R. Dickens, Gaurav Bhatnagar, Frederick S. Colwell, Walter Chapman, George J. Hirasaki, AGU Fall Meeting, San Francisco, CA, Dec. 14-19, 2009 (poster).
3. Effect of Hydrocarbon Components on Hydrate/Gas Distribution and BSR. Guangsheng Gu, Walter Chapman, Priyank Jaiswal, George J. Hirasaki, DOE Methane Hydrate Meeting, Georgia Tech University, Atlanta, GA, Jan 25-29, 2010 (oral presentation).
4. 2-D Simulation on Hydrate Accumulation in Different Heterogenous Lithology Structures, Guangsheng Gu, Sayatan Chatterjee, George J. Hirasaki, Walter G. Chapman, Brandon Dugan, Gaurav Bhatnagar, Colin Zelt, Gerald Dickens, Priyank Jaiswal, Gordon Research Conference on Natural Gas Hydrate Systems, Waterville, ME, June 6-11, 2010 (poster).
5. Brandon Dugan, Hugh Daigle, Sayantan Chatterjee, Guangsheng Gu, George Hirasaki, Continuum models of large-scale phenomena associated with hydrate-bearing sediments, Gordon Research Conference on Natural Gas Hydrate Systems, Waterville, ME, June 6-11, 2010 (oral presentation).

Subtask 6.8 (b): Sulfate, bicarbonate, calcium and carbon isotope ($\delta^{13}\text{C}$) profiles as an indicator of methane flux above marine gas hydrate systems: Sayantan Chatterjee

Abstract

Methane flux is an important constraint on the amount of hydrate that may be present in marine sediments. One approach to determine this flux is to use the depth to the sulfate-methane transition (SMT). Pore-water sulfate concentrations deplete to zero in shallow sediments above methane hydrate systems. Many authors attributed these chemical gradients to anaerobic oxidation of methane (AOM) at the SMT and directly related the depth of the SMT to the upward methane flux at steady-state conditions. However, an alternative mechanism for sulfate consumption by particulate organic carbon (POC) has been interpreted by various authors. To reconcile these two interpretations, *Bhatnagar and others' 1D model (2008)* was extended and methane, sulfate, dissolved inorganic carbon (DIC), calcium and carbon isotope concentration profiles were computed with both advective and diffusive fluxes. In addition to the mass balances, sulfate consumption reactions following two reaction pathways (i.e.: POC driven and AOM) have been included in the model. In most marine gas hydrate systems, it is shown that cross-plot of fluxes of sulfate and DIC around the SMT lie on a 1:1 line and justifies the dominance of AOM for sulfate consumption in shallow sediment. For insignificant fluxes, relative to sulfate reduction by POC, the concentration cross-plot lie on the 2:1 line justifying the alternative reaction mechanism by POC. The numerical model developed in this report serves as a tool to interpret upward methane fluxes with the help of pore water profiles.

Introduction

The amount of gas hydrate is controlled by dynamic inputs and outputs of methane over geologic timescales (Dickens, 2003; Buffett and Archer, 2004). The upward methane flux is an important constraint on the amount and distribution of hydrates. In the shallow sediments (~30 mbsf) above all gas hydrate systems there exists a sulfate-methane transition (SMT) zone where pore water sulfate gets depleted to near-zero concentration, generally underlain by rapid increase in methane concentrations.

For most gas hydrate systems, one potential approach for determining methane flux is to use the depth to the SMT (, Figure 6.8.1). Many authors have attributed depletion in pore water sulfate at the SMT to anaerobic oxidation of methane (AOM). Indeed, if AOM dominates consumption of methane and sulfate and the system is at steady-state conditions, the depth of the SMT should be directly related to the upward flux of methane (Borowski *et al.*, 1996; Snyder *et al.*, 2007; Dickens and Snyder, 2007).

The sulfate sink in these systems involves dissolved methane to consume sulfate at the SMT as shown in (1).

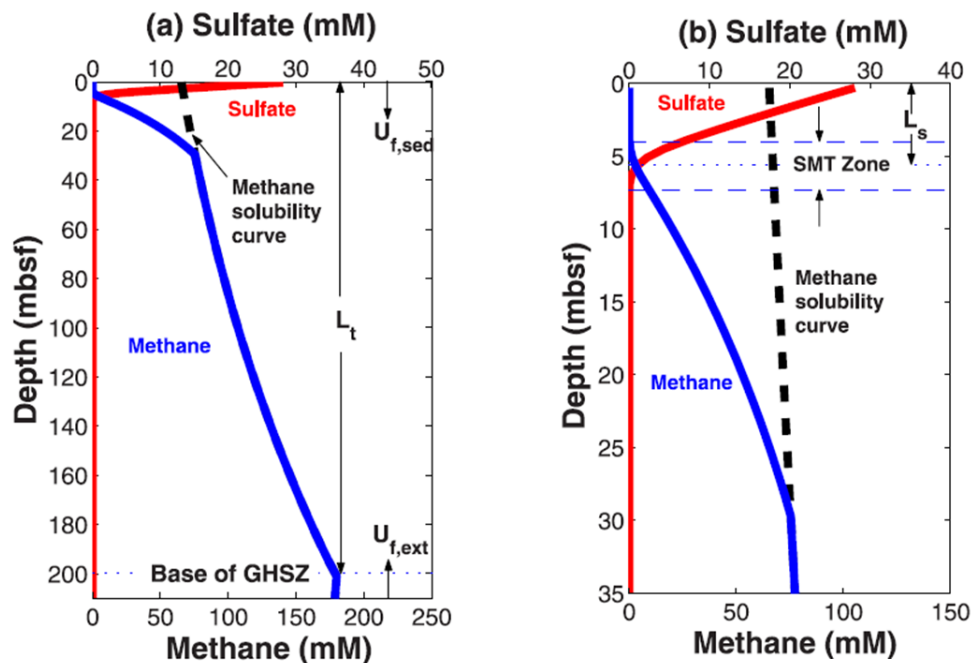
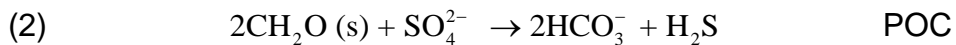


Figure 6.8.1: (a) Schematic representation of a gas hydrate system showing pore water sulfate and methane concentrations, which go to zero at shallow depths due to AOM. The dashed line represents the methane solubility curve. Fluid fluxes due to compaction driven flow and external flow are denoted as and respectively; is the depth to the base of the gas hydrate stability zone. (b) Zoomed sulfate-methane transition (SMT) zone showing an overlap of sulfate and methane profiles and its depth below the seafloor (Bhatnagar *et al.*, 2008).

Previous numerical modeling attempts have also shown that the net upward flux controls the pore water methane and sulfate concentration profiles and is thus related to the SMT depth (Bhatnagar *et al.*, 2008). Furthermore, the thickness of the hydrate zone and the gas hydrate saturation have been reported to be direct functions of the upward methane flux (Davie and Buffett, 2001; Bhatnagar *et al.*, 2008). Several studies have shown correlation between the SMT depth and the shallowest occurrence of gas hydrate (Borowski *et al.*, 1999). Few specific sites suggested a “rule of ten” where the shallowest gas hydrate occurs at a depth 10 times of the SMT (Paull *et al.*, 2005). Using a generalized one-dimensional (1D) numerical model, validated by an analytical theory (Bhatnagar *et al.*, 2010), Bhatnagar and coworkers estimated that the top of the gas hydrate layer occurs at 10-12 times of the SMT depth (Bhatnagar *et al.*, 2008). Thus, one-to-one relationships exist between the SMT depth; and the

upward methane flux, the gas hydrate layer thickness and the gas hydrate saturation within the GHSZ.

In addition to AOM, particulate organic carbon (POC) can also consume pore water sulfate in shallow sediments. In the absence of methane, bacteria use the POC as a substrate to consume sulfate (Berner, 1980; Boudreau and Westrich, 1984). This reaction involves the oxidation of organic carbon and the reduction of sulfate to produce DIC and hydrogen sulfide shown in (2):



Notably, the amounts of reactants and products in the two reactions are different. In (1) $\text{HCO}_3^- : \text{SO}_4^{2-}$ stoichiometry is 1:1, whereas in (2) it is 2:1.

Presently, the use of sulfate profiles and the SMT depth to calculate upward methane fluxes is controversial because various authors have interpreted pore water composition and carbon isotope data in shallow sediment differently, even at the same sites (Kastner et al., 2008; Dickens and Snyder, 2009). The roots of the problem are twofold: (1) sulfate consumption can occur through two reaction pathways, and (2) dissolved inorganic carbon (DIC), a reaction constituent, has multiple sources and sinks.

Bhatnagar and co-workers developed a generalized 1D numerical model for gas hydrate accumulation in marine sediments over geologic timescales (Bhatnagar et al., 2007). Previous 1D model computed methane and sulfate profiles, however, DIC, calcium and carbon isotopes were not coupled with methane and sulfate mass balance equations. In this report, both the interpretations regarding the sulfate reduction stoichiometry and the carbon isotope balance are revisited and Bhatnagar's 1D model (Bhatnagar et al., 2007, 2008) was extended. Hence, both the sulfate consumption reactions (POC and AOM) were included and mass balances of all the carbon and sulfate species in the system were coupled.

Example site – Hydrate Ridge, 1244, Cascadia margin

As an example, physical properties and seafloor conditions were chosen similar to Hydrate Ridge site 1244 from the Ocean Drilling Program (ODP) leg 204 data to simulate the pore water chemistry profiles. This site is located at 890m below sea level (mbsl) on the eastern flank of the Hydrate Ridge about 3km northeast of the southern summit (Trehú et al., 2003). The seafloor temperature (276.8 K) and pressure are well within the range for hydrate stability and occurrence and the linear geothermal gradient is 0.061°C/m. For these parameters, our calculations show that the temperature profile intersects the three-phase equilibrium curve at about 133.4 m below seafloor and marks the base of the GHSZ. Sedimentation rate is 27 cm kyr^{-1} and porosity of the sediments at the seafloor, is about 70% (Trehú et al., 2003). Other parameters that are specific to site 1244, used in this model are listed in appendix. The concentration profiles of sulfate, methane, alkalinity (DIC), and calcium in pore

water and carbon isotope $\delta^{13}\text{C}$ data in DIC obtained from leg 204 data for hole 1244 are shown in Figure 6.8.2 (Trehú *et al.*, 2003). Note methane (red) and sulfate (blue) concentrations are shown in the same plot. Methane concentrations are low because significant quantity of methane was lost during its measurement. Notably, in 1244, the SMT is located at ~8.5 mbsf, where pore water sulfate approaches zero concentration and the remaining interstitial water species show a distinguishable change in slope at the same depth.

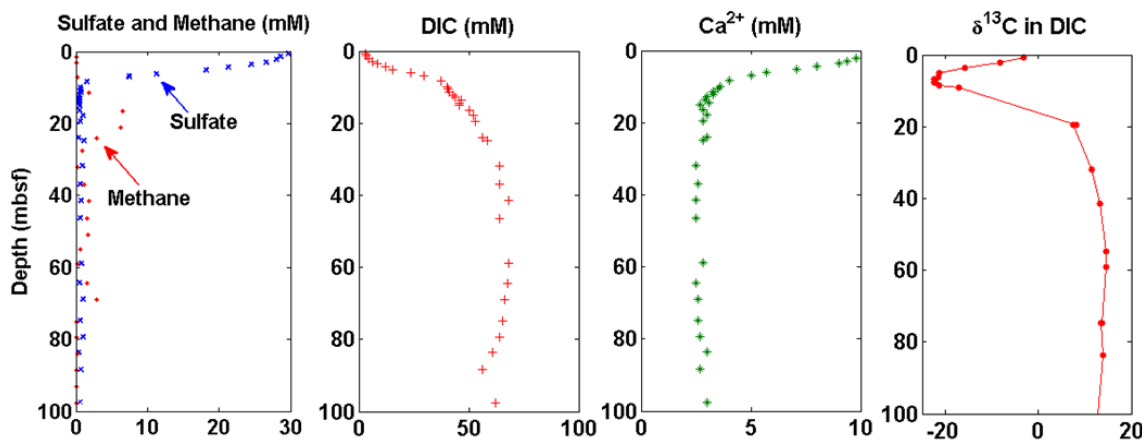


Figure 6.8.2: Sulfate, methane, alkalinity (DIC), calcium concentration profiles and carbon isotope $\delta^{13}\text{C}$ composition in DIC for shallow sediment at site 1244 on Hydrate Ridge (original data from Trehú *et al.*, 2003)

Two contradictory hypotheses

The two contradictory hypotheses revolve around the dominance of two reactions for sulfate consumption namely; AOM and POC driven consumption as stated earlier. Borowski *et al.* (1996) initially interpreted how sulfate gradients may be used as a proxy to measure in-situ methane fluxes from underlying hydrate sediments at sites where linear sulfate profiles exist. Linear sulfate profiles in shallow sediments indicate that sulfate profile is primarily driven by diffusion to the SMT where it reacts at the SMT with the methane flux from below. This is in contrast to reaction with POC which is distributed throughout the sediment. If AOM is the dominant reaction, then at steady state conditions, sulfate and methane fluxes should be balanced (Borowski *et al.*, 1996), and the pore water sulfate concentration profile is determined by the upward methane flux originating from deeper sediments.

Argument for POC reaction

Several investigators (Kastner *et al.*, 2008) have attempted to discriminate between the two reactions using pore water concentration profiles and carbon

isotope data. In particular, arguments for the dominance of POC reaction over AOM have been made using cross-plots of change in excess alkalinity versus change in sulfate concentration (Figure 6.8.3). Excess alkalinity is the amount of HCO_3^- (more commonly DIC) that would occur in pore water if authigenic carbonate had not precipitated. The change in excess alkalinity can be computed by summing the deviations in pore water alkalinity, Ca^{2+} and Mg^{2+} relative to their respective concentration in seawater. The change in pore water sulfate concentration is relative to the seawater. In the case shown here (Figure 6.8.3), there is a 2:1 slope, which Kastner and others interpret as release of two moles of DIC due to consumption of one mole of sulfate. If this interpretation is correct, this would imply POC driven sulfate consumption in a closed system (Kastner *et al.*, 2008). A closed system is one in which sulfur and carbon fluxes in and out of sediment horizons are zero. This situation does not occur in most areas with gas hydrate because fluxes through diffusion and advection are usually faster than through sedimentation.

The carbon isotope composition ($\delta^{13}\text{C}$) of DIC across the SMT has also been used to infer the POC driven reaction mechanism (Kastner *et al.*, 2008). The overall idea is that POC has a $\delta^{13}\text{C}$ of -25‰ whereas biogenic methane has a $\delta^{13}\text{C}$ of -60‰, so the isotope composition of DIC at the SMT should give the proportion generated from AOM and POC. For example, the nominally -25‰ of DIC across the SMT at site 1244 has been argued to reflect a dominance of POC consumption of sulfate.

Argument for AOM reaction

An analysis of reactants and products using fluxes is a much better approach for understanding the stoichiometry of the sulfate consumption reaction. This is particularly true because there is often a flux of DIC into the SMT from below (Dickens and Snyder, 2009). Specifically, at ODP site 1244, when one calculates fluxes of DIC, there are -6 mol/m²kyr of HCO_3^- entering the SMT from below and -22 mol/m²kyr of HCO_3^- are leaving the SMT towards the seafloor. This gives a net change of -16 mol/m²kyr of HCO_3^- across the SMT. This net change of HCO_3^- flux nicely balances the +16 mol/m²kyr of SO_4^{2-} entering the SMT, suggesting a 1:1 stoichiometry (Dickens and Snyder, 2009).

The source of deep flux of DIC is from the biogenic generation of methane occurring in deeper sediments. The methanogenesis reaction involves breakdown of two moles of POC to form one mole of methane and one mole of carbon dioxide under microbial action via a series of reactions as shown below.

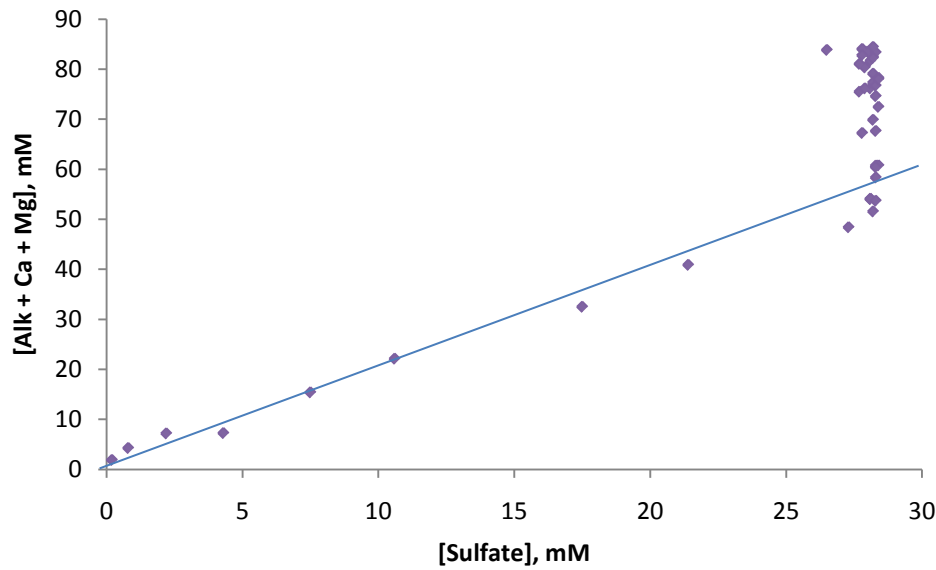
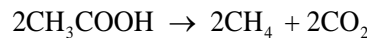
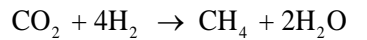
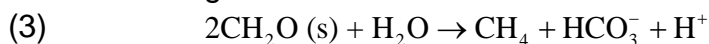


Figure 6.8.3: Concentration cross-plot of “excess alkalinity” corrected for carbonate precipitation versus SO_4^{2-} (mM) relative to the seafloor for shallow sediment at site 1244 on Hydrate Ridge (original data from Trehú *et al.*, 2003). As emphasized by Kastner *et al.* (2008), there is a 2:1 relationship for pore water concentrations above the SMT. Note, however, that excess alkalinity continues to rise below the SMT. There is an upward flux of HCO_3^- from deeper sediment, which necessarily implies that only a fraction of excess alkalinity above the SMT comes from shallow sediment

Methanogenesis reaction is a biochemical reaction and can be represented as a series of the following reactions.



The overall methanogenesis reaction is shown below in (3).



Over geologic timescales, sedimentation and deposition of older sediments buries the organic carbon to greater depths. This gives rise to the deeper DIC flux coming from below. However, DIC formed during methanogenesis typically has an isotope composition of $+10\text{\textperthousand}$ or greater. This means that, in an open system, the measured $\delta^{13}\text{C}$ of DIC across the SMT is the

net result of $\delta^{13}\text{C}$ formed by reactions at the SMT (e.g., AOM) and DIC fluxing in to and out of the SMT. A DIC of -25‰ across the SMT can result from AOM and a deep DIC flux with a $\delta^{13}\text{C}$ of +10‰ or greater (Dickens and Snyder, 2009). So, an observed value of $\delta^{13}\text{C}$ of DIC of -25‰ at the SMT need not be concluded to be a result of POC driven sulfate consumption. It could also be due to combined effect of AOM and deep source of DIC as a result of methanogenesis. To reconcile these two hypotheses, a mathematical model has been formulated and presented in the following section.

Numerical model

Gas hydrate accumulation in marine sediment has been modeled for 1D systems by Bhatnagar and others (Bhatnagar *et al.*, 2007). Their overall modeling framework incorporated phase equilibrium and methane solubility calculations in addition to sediment deposition, porosity reduction and mass conservation for methane, water, and organic content. The model included advective and diffusive fluid fluxes as a result of compaction, and upward fluid flow arising from deeper sediments. However, the model did not couple bicarbonate, calcium, and carbon isotope composition along with methane and sulfate mass balances. All gas hydrate systems harbor few primary chemical reactions involving various pore water chemical species as listed below. The following three reactions are expressed with their corresponding kinetic models defining the kinetic rate for the respective reactions; and the fourth reaction is a reversible reaction and the equilibrium model is shown as follows:

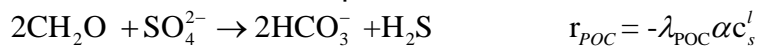
- (i) Methanogenesis and fermentation reaction in deeper sediments



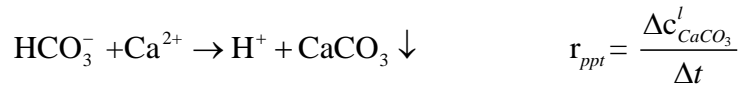
- (ii) AOM reaction at the SMT



- (iii) POC driven sulfate consumption between the seafloor and the SMT



- (iv) Calcite precipitation reaction



The methanogenesis rate of reaction is represented by λ ; whereas the rates of reaction for sulfate reduction by POC and AOM are denoted by λ_{POC} , and λ_{AOM} , respectively. Unlike the kinetic modeling for the irreversible reactions, equilibrium rate for the calcite precipitation reaction is modeled differently as a function of formation of calcium carbonate. The authigenic carbonate precipitation is an equilibrium reaction and its rate is quantified by the amount of calcium carbonate formed in unit time. The phase concentration for the different species are represented as c_m^l for methane, c_s^l for sulfate, c_b^l for DIC, c_{ca}^l for calcium, $c_{\text{CaCO}_3}^l$ for

calcium carbonate and α for POC. Hydrogen ions that are being formed in the system as a product of different reactions are assumed to be transported by advection and diffusion, thereby avoiding accumulation of hydrogen ions which would eventually make the formation acidic and the reactions would eventually stop. However, the hydrogen ion transport is not modeled in this work.

Organic Material Balance for in-situ production

The organic carbon content available for methanogenesis (α) is represented as a mass fraction of the total sediment. However, α represents only a fraction of the total organic carbon (TOC) since the entire content is not converted to methane. The sedimentation rate (v_s) and amount of degradable organic content at the seafloor is assumed to remain constant over time. Furthermore, the POC is modeled to advect downward with the sediment velocity v_s . With the above assumptions, the organic material balance is shown below.

$$\frac{\partial}{\partial t}[(1-\phi)\rho_{sed}\alpha] + \frac{\partial}{\partial z}[(1-\phi)\rho_{sed}v_s\alpha] = -\rho_{sed}\lambda(1-\phi)\alpha - \frac{\phi(1-\phi)}{M_{SO_4}}\lambda_{POC}(\rho_{sed}\alpha)(\rho_w c_s^l)$$

Further, the material balance could be rewritten in terms of sediment and fluid fluxes instead of velocities. The material balance equation can be rewritten in a dimensionless form using the scaling scheme developed by Bhatnagar *et al.* (2007) and presented as follows.

$$\frac{\partial}{\partial \tilde{t}}(\tilde{\alpha}(1-\tilde{\phi})) + Pe_1 \frac{\partial}{\partial \tilde{z}}\left[\left(\frac{1+\gamma}{\gamma}\right)\tilde{U}_s\tilde{\alpha}\right] = -Da(1-\tilde{\phi})\tilde{\alpha} - \frac{(1-\tilde{\phi})(1+\gamma\tilde{\phi})}{1+\gamma} \frac{M_{POC}c_{s,o}}{M_{SO_4}c_{m,eqb}} \frac{D_s}{D_m} Da_{POC} \tilde{\alpha} \tilde{c}_s^l$$

Methane Mass Balance

Following previous work (Bhatnagar *et al.*, 2007; 2008), the methane mass balance equations have been simplified to exclude the gas hydrate and free gas phase terms. Assuming methane generation from POC and consumption due to AOM reaction, the mass balance equations are illustrated below.

$$\frac{\partial}{\partial t}[\phi\rho_w c_m^l] + \frac{\partial}{\partial z}[U_f \rho_w c_m^l] = \frac{\partial}{\partial z}\left[\phi\rho_w D_m \frac{\partial c_m^l}{\partial z}\right] + \frac{M_{CH_4}}{M_{POC}} \rho_{sed}\lambda(1-\phi)\alpha - \frac{\phi\lambda_{AOM}(\rho_w c_m^l)(\rho_w c_s^l)}{M_{SO_4}}$$

The terms on the left are the accumulation term followed by the convection term. The terms on the right hand side represent diffusion followed by the reaction terms. The reaction terms correspond to methanogenesis from POC and AOM, respectively. The mass balance equation can be rewritten in a dimensionless form using the same scaling scheme shown above.

$$\begin{aligned} \frac{\partial}{\partial \tilde{t}} \left[\left(\frac{1+\gamma\tilde{\phi}}{\gamma} \right) \tilde{c}_m^l \right] + \left(\frac{1+\gamma}{\gamma} \right) (Pe_1 + Pe_2) \frac{\partial \tilde{c}_m^l}{\partial \tilde{z}} = \frac{\partial}{\partial \tilde{z}} \left[\left(\frac{1+\gamma\tilde{\phi}}{\gamma} \right) \frac{\partial \tilde{c}_m^l}{\partial \tilde{z}} \right] \\ + \frac{M_{CH_4}}{M_{POC}} \tilde{\rho}_{sed} Da \left(1 - \tilde{\phi} \right) \tilde{\alpha} \beta - \left(\frac{1+\gamma\tilde{\phi}}{\gamma} \right) \frac{M_{CH_4} c_{s,o}}{M_{SO_4} c_{m,eqb}} Da_{AOM} \tilde{c}_m^l \tilde{c}_s^l \end{aligned}$$

Sulfate Mass Balance

The sulfate mass balance includes both the reaction pathways for sulfate consumption in which both act as sinks for pore water sulfate and are shown below (Bhatnagar *et al.* 2008).

$$\frac{\partial}{\partial t} \left[\phi \rho_w c_s^l \right] + \frac{\partial}{\partial z} \left[U_f \rho_w c_s^l \right] = \frac{\partial}{\partial z} \left[\phi \rho_w D_s \frac{\partial c_s^l}{\partial z} \right] - \frac{\phi(1-\phi)}{M_{POC}} \lambda_{POC} (\rho_{sed} \alpha) (\rho_w c_s^l) - \frac{\phi \lambda_{AOM} (\rho_w c_m^l) (\rho_w c_s^l)}{M_{CH_4}}$$

The reaction terms correspond to sulfate consumption due to POC and AOM, respectively. The dimensionless sulfate mass balance equation is rewritten and presented using the same scaling scheme shown above.

$$\begin{aligned} \frac{\partial}{\partial \tilde{t}} \left[\left(\frac{1+\gamma\tilde{\phi}}{\gamma} \right) \tilde{c}_s^l \right] + \left(\frac{1+\gamma}{\gamma} \right) (Pe_1 + Pe_2) \frac{\partial \tilde{c}_s^l}{\partial \tilde{z}} = \frac{\partial}{\partial \tilde{z}} \left[\left(\frac{1+\gamma\tilde{\phi}}{\gamma} \right) D_s \frac{\partial \tilde{c}_s^l}{\partial \tilde{z}} \right] \\ - \frac{(1-\tilde{\phi})(1+\gamma\tilde{\phi})}{1+\gamma} \frac{D_s}{D_m} \tilde{\rho}_{sed} Da_{POC} \tilde{\alpha} \beta \tilde{c}_s^l - \left(\frac{1+\gamma\tilde{\phi}}{\gamma} \right) Da_{AOM} \tilde{c}_m^l \tilde{c}_s^l \end{aligned}$$

DIC Mass Balance

As pointed out previously, DIC mass balance is a necessary step to investigate the competing hypotheses for the loss of sulfate. Similar to the sulfate balance, DIC mass balance not only includes source terms originating from both AOM and POC reactions but also includes source terms like the methanogenesis reaction. In addition to the source terms, the DIC mass balance includes a sink term corresponding to the calcite precipitation reaction as shown below. The sink term originates from the calcium carbonate that precipitates in the reaction. When DIC (or carbonate) reacts with calcium following a 1:1 stoichiometry, both species continue to get consumed and form calcium carbonate which precipitates out of solution as long as the product of calcium and DIC concentration is greater than the solubility product (k_{sp}) of calcium carbonate. When the product of DIC and carbonate concentrations equal the solubility product, their concentrations does not reduce any further, instead precipitates an equivalent amount of calcium carbonate and the reaction reaches equilibrium. The equilibrium reaction is modeled in such a way that calcium concentration is always constrained at the equilibrium concentration. Any calcium which gets consumed in excess of the equilibrium concentration forms calcium carbonate. Consequently, DIC also gets reduced by a similar amount in the reaction. The amount of calcium carbonate generated can be computed from the mass balance equations.

$$\begin{aligned} \frac{\partial}{\partial t} [\phi \rho_w c_b^l] + \frac{\partial}{\partial z} [U_f \rho_w c_b^l] &= \frac{\partial}{\partial z} \left[\phi \rho_w D_b \frac{\partial c_b^l}{\partial z} \right] + \frac{M_{HCO_3}}{M_{POC}} \rho_{sed} \lambda (1-\phi) \alpha \\ &+ \frac{M_{HCO_3} \phi \lambda_{AOM} (\rho_w c_m^l) (\rho_w c_s^l)}{M_{CH_4} M_{SO_4}} + \frac{2M_{HCO_3} \phi (1-\phi) \lambda_{POC} (\rho_{sed} \alpha) (\rho_w c_s^l)}{M_{POC} M_{SO_4}} - \phi \rho_w \frac{\Delta c_{CaCO_3}^l}{\Delta t} \end{aligned}$$

The reaction terms represent generation of DIC due to methanogenesis, AOM reaction, POC–sulfate reaction, and DIC consumption due to calcite precipitation, respectively. The dimensionless form has been illustrated below using the same scaling scheme discussed above.

$$\begin{aligned} \frac{\partial}{\partial \tilde{t}} \left[\left(\frac{1+\gamma\tilde{\phi}}{\gamma} \right) \tilde{c}_b^l \right] + \left(\frac{1+\gamma}{\gamma} \right) (Pe_1 + Pe_2) \frac{\partial \tilde{c}_b^l}{\partial \tilde{z}} &= \frac{\partial}{\partial \tilde{z}} \left[\left(\frac{1+\gamma\tilde{\phi}}{\gamma} \right) \frac{D_b}{D_m} \frac{\partial \tilde{c}_b^l}{\partial \tilde{z}} \right] + \frac{M_{HCO_3} c_{m,eqb}}{M_{POC} c_{b,o}} \tilde{\rho}_{sed} Da (1-\tilde{\phi}) \tilde{\alpha} \beta \\ &+ \left(\frac{1+\gamma\tilde{\phi}}{\gamma} \right) \frac{M_{HCO_3} c_{s,o}}{M_{SO_4} c_{b,o}} Da_{AOM} \tilde{c}_m^l \tilde{c}_s^l + \frac{2M_{HCO_3} c_{s,o} (1-\tilde{\phi}) (1+\gamma\tilde{\phi})}{M_{SO_4} c_{b,o} (1+\gamma)} \frac{D_s}{D_m} \tilde{\rho}_{sed} Da_{POC} \tilde{\alpha} \beta \tilde{c}_s^l - \left(\frac{1+\gamma\tilde{\phi}}{\gamma} \right) \frac{c_{b,o}}{c_{Ca,o}} \frac{\Delta \tilde{c}_{CaCO_3}^l}{\Delta \tilde{t}} \end{aligned}$$

Calcium Mass Balance

Calcium mass balance is another important component including the sink term corresponding to the calcite precipitation reaction and presented as follows. The sink term is represented as the amount of calcium carbonate actually formed in the reaction.

$$\frac{\partial}{\partial t} [\phi \rho_w c_{Ca}^l] + \frac{\partial}{\partial z} [U_f \rho_w c_{Ca}^l] = \frac{\partial}{\partial z} \left[\phi \rho_w D_{Ca} \frac{\partial c_{Ca}^l}{\partial z} \right] - \phi \rho_w \frac{\Delta c_{CaCO_3}^l}{\Delta t}$$

Using the same scaling scheme developed by Bhatnagar et al., (2007), the dimensionless form is expressed as follows.

$$\frac{\partial}{\partial \tilde{t}} \left[\left(\frac{1+\gamma\tilde{\phi}}{\gamma} \right) \tilde{c}_{Ca}^l \right] + \left(\frac{1+\gamma}{\gamma} \right) (Pe_1 + Pe_2) \frac{\partial \tilde{c}_{Ca}^l}{\partial \tilde{z}} = \frac{\partial}{\partial \tilde{z}} \left[\left(\frac{1+\gamma\tilde{\phi}}{\gamma} \right) \frac{D_{Ca}}{D_m} \frac{\partial \tilde{c}_{Ca}^l}{\partial \tilde{z}} \right] - \left(\frac{1+\gamma\tilde{\phi}}{\gamma} \right) \frac{\Delta \tilde{c}_{CaCO_3}^l}{\Delta \tilde{t}}$$

Carbon isotope Mass Balance

Carbon isotope mass balance is also included in our model. A simple carbon mass balance along with its isotope composition for the different species provides an overall conservation of carbon isotopes in the system. Notably, POC, methane, and DIC are the three carbon species with different carbon isotope composition for the various reactions listed above. This motivates us to write the carbon isotope mass balance separately for methane and DIC due to all the reactions sources and sinks in the system as illustrated below. This summarizes the mass conservation for all the species necessary for the mathematical model.

Carbon isotope in Methane

$$\begin{aligned} \frac{\partial}{\partial t} \left[\phi \rho_w \delta c_m^l - {}^{13}\text{CH}_4 \right] + \frac{\partial}{\partial z} \left[U_f \rho_w \delta c_m^l - {}^{13}\text{CH}_4 \right] &= \frac{\partial}{\partial z} \left[\phi \rho_w D_m \frac{\partial (\delta_m^l - {}^{13}\text{CH}_4)}{\partial z} \right] \\ &+ \frac{M_{CH_4}}{M_{POC}} \rho_{sed} \lambda (1-\phi) \alpha - {}^{13}\text{CH}_4, \text{ meth} - \frac{\phi \lambda_{AOM} \delta \rho_w c_m^l (\rho_w c_s^l) - {}^{13}\text{CH}_4}{M_{SO_4}} \end{aligned}$$

The dimensionless mass balance equation is presented as follows.

$$\begin{aligned} \frac{\partial}{\partial \tilde{t}} \left[\left(\frac{1+\gamma\tilde{\phi}}{\gamma} \right) \tilde{c}_m^l \delta {}^{13}\text{CH}_4 \right] + \left(\frac{1+\gamma}{\gamma} \right) (Pe_1 + Pe_2) \frac{\partial}{\partial \tilde{z}} \left[\tilde{c}_m^l \delta {}^{13}\text{CH}_4 \right] &= \frac{\partial}{\partial \tilde{z}} \left[\left(\frac{1+\gamma\tilde{\phi}}{\gamma} \right) \frac{\partial (\tilde{c}_m^l \delta {}^{13}\text{CH}_4)}{\partial \tilde{z}} \right] \\ &+ \frac{M_{CH_4}}{M_{POC}} \tilde{\rho}_{sed} Da (1-\tilde{\phi}) \tilde{\alpha} \beta - {}^{13}\text{CH}_4, \text{ meth} - \left(\frac{1+\gamma\tilde{\phi}}{\gamma} \right) \frac{M_{CH_4} c_{s,o} \delta Da_{AOM} \tilde{c}_m^l \tilde{c}_s^l - {}^{13}\text{CH}_4}{M_{SO_4} c_{m,eqb}} \end{aligned}$$

Carbon isotope in DIC

$$\begin{aligned} \frac{\partial}{\partial t} \left[\phi \rho_w c_b^l \delta {}^{13}\text{HCO}_3 \right] + \frac{\partial}{\partial z} \left[U_f \rho_w c_b^l \delta {}^{13}\text{HCO}_3 \right] &= \frac{\partial}{\partial z} \left[\phi \rho_w D_b \frac{\partial (\delta_b^l - {}^{13}\text{HCO}_3)}{\partial z} \right] + \frac{M_{HCO_3}}{M_{POC}} \rho_{sed} \lambda (1-\phi) \alpha \delta {}^{13}\text{HCO}_3, \text{ meth} \\ &+ \frac{M_{HCO_3} \phi \lambda_{AOM} (\rho_w c_m^l) - {}^{13}\text{CH}_4}{M_{CH_4} M_{SO_4}} + \frac{2M_{HCO_3} \tilde{\phi} (1-\phi) \lambda_{POC} (\rho_{sed} \alpha) (\rho_w c_s^l) - {}^{13}\text{HCO}_3, \text{ POC}}{M_{POC} M_{SO_4}} - \phi \rho_w \frac{\Delta c_{CaCO_3}^l \delta {}^{13}\text{HCO}_3}{\Delta t} \end{aligned}$$

The dimensionless form can be represented as follows:

$$\begin{aligned} \frac{\partial}{\partial \tilde{t}} \left[\left(\frac{1+\gamma\tilde{\phi}}{\gamma} \right) \tilde{c}_b^l \delta {}^{13}\text{HCO}_3 \right] + \left(\frac{1+\gamma}{\gamma} \right) (Pe_1 + Pe_2) \frac{\partial}{\partial \tilde{z}} \left[\tilde{c}_b^l \delta {}^{13}\text{HCO}_3 \right] &= \frac{\partial}{\partial \tilde{z}} \left[\left(\frac{1+\gamma\tilde{\phi}}{\gamma} \right) D_b \frac{\partial (\tilde{c}_b^l \delta {}^{13}\text{HCO}_3)}{\partial \tilde{z}} \right] \\ &+ \frac{M_{HCO_3} c_{m,eqb} \tilde{\rho}_{sed} Da (1-\tilde{\phi}) \tilde{\alpha} \beta - {}^{13}\text{HCO}_3, \text{ meth}}{M_{POC} c_{b,o}} + \left(\frac{1+\gamma\tilde{\phi}}{\gamma} \right) \frac{M_{HCO_3} c_{s,o} \delta Da_{AOM} \tilde{c}_m^l \tilde{c}_s^l - {}^{13}\text{CH}_4}{M_{SO_4} c_{b,o}} \\ &+ \frac{2M_{HCO_3} c_{s,o} (1-\tilde{\phi}) (1+\gamma\tilde{\phi}) D_s}{M_{SO_4} c_{b,o} (1+\gamma)} \frac{D_s}{D_m} \tilde{\rho}_{sed} Da_{POC} \tilde{\alpha} \beta \tilde{c}_s^l - {}^{13}\text{HCO}_3, \text{ POC} - \left(\frac{1+\gamma\tilde{\phi}}{\gamma} \right) \frac{c_{b,o}}{c_{Ca,o}} \frac{\Delta (\tilde{c}_{CaCO_3}^l)^3 - {}^{13}\text{HCO}_3}{\Delta \tilde{t}} \end{aligned}$$

During the AOM reaction, the carbon isotope ($\delta^{13}\text{C}$) composition in methane and

DIC is represented by $\delta^{13}_{\text{CH}_4}$. During calcite precipitation, the $\delta^{13}C$ value in DIC and calcium is $\delta^{13}_{\text{HCO}_3}$.

The vertical depth is scaled by the depth of the base of the gas hydrate stability zone (BHSZ) L_t , and time is normalized by a combination of depth of the BSHZ L_t and diffusivity of methane D_m .

$$\tilde{z} = z/L_t \quad \tilde{t} = \frac{t}{L_t^2/D_m}$$

The degradable content of POC in the sediment is normalized relative to the initial content deposited at the seafloor (α_0). Normalized organic content in sediment is defined:

$$\tilde{\alpha} = \frac{\alpha}{\alpha_0}$$

Methane mass fraction in phase i is normalized by methane solubility in the liquid phase at the base of GHSZ $\tilde{c}_{m,eqb}^l$, while sulfate, DIC, and calcium mass fractions are normalized by their respective seawater values $c_{s,o}$ (=28 mM), $c_{b,o}$ (=2.29 mM) and $c_{ca,o}$ (=10 mM) to get their corresponding normalized variables. The normalized variables are defined:

$$\tilde{c}_m^l = \frac{c_m^l}{\tilde{c}_{m,eqb}^l} \quad \tilde{c}_s^l = \frac{c_s^l}{\tilde{c}_{s,o}^l} \quad \tilde{c}_b^l = \frac{c_b^l}{\tilde{c}_{b,o}^l} \quad \tilde{c}_{ca}^l = \frac{c_{ca}^l}{\tilde{c}_{ca,o}^l}$$

The reduced porosities, $\tilde{\phi}$, η and γ , normalized sediment flux \tilde{U}_{sed} , are defined:

$$\tilde{\phi} = \frac{\phi - \phi_\infty}{1 - \phi_\infty} \quad \eta = \frac{\phi_0 - \phi_\infty}{1 - \phi_\infty} \quad \gamma = \frac{1 - \phi_\infty}{\phi_\infty} \quad \tilde{U}_{\text{sed}} = \frac{U_{\text{sed}}}{U_{f,\text{sed}}}$$

where the porosity of sediment is ϕ , ϕ_0 is the initial porosity at the seafloor, ϕ_∞ is the minimum porosity attained at greatest depth, and $U_{f,\text{sed}}$ is the fluid flux due to sedimentation and compaction. Porosity changes with depth, seafloor porosity $\phi_0 = 0.7$ and minimum porosity attained at greatest depth $\phi_\infty = 0.1$ representing occurrence of compaction.

The fluid flux $U_{f,\text{sed}}$ can be defined as a combination of seafloor sedimentation rate \dot{S} and porosities.

$$U_{f,\text{sed}} = \frac{1 - \phi_0}{1 - \phi_\infty} \dot{S} \phi_\infty$$

The flux of sediment is represented by U_{sed} and is scaled with respect to the fluid flux due to sedimentation $U_{f,\text{sed}}$, which equals to a constant, γ .

$$\tilde{U}_s = \frac{U_{sed}}{U_{f,sed}} = \frac{1-\phi_o}{U_{f,sed}} \dot{S} = \frac{\left(\frac{1-\phi_\infty}{\phi_\infty} \right) U_{f,sed}}{U_{f,sed}} = \left(\frac{1-\phi_\infty}{\phi_\infty} \right) = \gamma$$

The numerical model incorporates two fluid fluxes to characterize the compaction driven and external fluid flow relative to diffusion; defined by two independent dimensionless groups known as Peclet numbers. The dimensionless group Peclet number Pe_1 is characterized by the ratio of sedimentation-compaction driven fluid flux to methane diffusion.

$$Pe_1 = \frac{U_{f,sed} L_t}{D_m}$$

Similarly, Pe_2 is characterized by the ratio of external fluid flux from deeper sediments relative to methane diffusion.

$$Pe_2 = \frac{U_{f,ext} L_t}{D_m}$$

Crucially, Pe_1 and Pe_2 act in downward and upward directions respectively, and have opposite signs.

The dimensionless group Damkohler number is characterized by the ratio of reaction to diffusion. The three Damkohler numbers for the three main reactions mentioned above are defined.

$$\text{Methanogenesis Reaction} \quad Da = \frac{\lambda L_t^2}{D_m}$$

$$\text{Anaerobic Oxidation of Methane} \quad Da_{AOM} = \frac{\rho_w c_{m,eqb}^w}{M_{CH_4}} \frac{\lambda_{AOM} L_t^2}{D_m}$$

$$\text{POC dominated sulfate reduction} \quad Da_{POC} = \frac{\rho_w c_{m,eqb}^w}{M_{POC}} \frac{\lambda_{POC} L_t^2}{D_s}$$

All the parameters and dimensionless groups are specified as shown (Appendix C). To obtain finite solutions, the initial and boundary conditions are specified in addition to the mass balance equations.

Initial Conditions

Organic content, methane, sulfate, DIC, calcium and carbon isotope concentration are assumed to be zero at initial time $\tilde{t} = 0$ for any depth \tilde{z} .

$$\begin{aligned} \tilde{\alpha}(\tilde{z}, 0) &= 0 & \tilde{c}_m^l(\tilde{z}, 0) &= 0 & \tilde{c}_s^l(\tilde{z}, 0) &= \tilde{c}_b^l(\tilde{z}, 0) = \tilde{c}_{Ca}^l(\tilde{z}, 0) = 0 \\ \delta^{13}C_{CH_4}(\tilde{z}, 0) &= 0 & \delta^{13}C_{HCO_3}(\tilde{z}, 0) &= 0 \end{aligned}$$

Boundary Conditions

Methane is assumed to form biogenically from POC and organic concentration is normalized with the seafloor value, thereby specifying the normalized POC concentration at the seafloor to unity. Methane concentration is normalized relative to the triple point concentration of methane $\tilde{c}_{m,eqb}^l$ at the base of GHSZ. Since, there is no methane at the seafloor, normalized methane concentration at the seafloor is zero. Sulfate, DIC and calcium are normalized with its seawater values and the normalized sulfate, DIC and calcium concentrations are unity at the seafloor. Carbon isotope compositions are normalized relative to a standard marine carbonate Pee-Dee-Belemnite, therefore the normalized carbon isotope compositions at the seafloor are zero.

$$\begin{aligned}\tilde{\alpha}(0, \tilde{t}) &= 1 & \tilde{c}_m^l(0, \tilde{t}) &= 0 & \tilde{c}_s^l(0, \tilde{t}) = \tilde{c}_b^l(0, \tilde{t}) = \tilde{c}_{ca}^l(0, \tilde{t}) &= 1 \\ \delta^{13}C_{CH_4}(0, \tilde{t}) &= \delta^{13}C_{HCO_3}(0, \tilde{t}) = 0\end{aligned}$$

Upward methane flux is assumed to originate in deeper sediments due to methane generated as a result of methanogenesis. In order to incorporate the upward methane flux, an methane concentration is specified at the base of the simulation domain.

$$\begin{aligned}\tilde{c}_m^l(0, \tilde{t}) &= 0 \\ \tilde{c}_m^l(\tilde{L}_z, \tilde{t}) &= \tilde{c}_{m,ext}^l = \tilde{c}_{m,eqb}^l(\tilde{L}_z)\end{aligned}$$

where $\tilde{c}_{m,ext}^l$ is the specified methane concentration, at the bottom of the domain, L_z , and is equal to the solubility methane concentration $\tilde{c}_{m,eqb}^l$ at L_z . $\tilde{c}_{m,ext}^l$ is also normalized with the triple point concentration of methane.

Similarly, a deep flux of DIC and calcium are specified in the model and therefore an equivalent DIC and calcium molar concentration are specified at the base of the domain whereas sulfate does not have any upward flux in the system. Therefore, zero sulfate concentration and known methane $\tilde{c}_{m,ext}^l$, DIC $\tilde{c}_{b,ext}^l$, and calcium $\tilde{c}_{ca,ext}^l$ concentrations are specified at the base of the simulation domain. During the methanogenesis reaction, equal amounts of methane and DIC are formed, so their molar fluxes are equated at the bottom boundary. DIC molar concentration are specified equal to the molar concentration of methane at the bottom of our simulation domain. For a corresponding DIC concentration, calcium concentration is computed from the solubility product at the bottom boundary. Dirichlet boundary conditions are assumed at the seafloor and bottom of the domain.

$$\tilde{c}_s^l(\tilde{L}_z, \tilde{t}) = \tilde{c}_{s,ext}^l = 0 \quad \tilde{c}_b^l(\tilde{L}_z, \tilde{t}) = \tilde{c}_{b,ext}^l \quad \tilde{c}_{ca}^l(\tilde{L}_z, \tilde{t}) = \tilde{c}_{ca,ext}^l$$

where $\tilde{c}_{s,ext}^l$, $\tilde{c}_{b,ext}^l$, and $\tilde{c}_{ca,ext}^l$ are specified concentrations of sulfate, DIC, and calcium at the bottom of the domain \tilde{L}_z normalized with the seawater concentrations $\tilde{c}_{s,o}^l$, $\tilde{c}_{b,o}^l$ and $\tilde{c}_{ca,o}^l$ respectively. Methanogenesis is assumed to occur through CO₂ reduction pathway and follows 70% isotope fractionation ($\alpha =$

1.07) (Whiticar, 1999). The organic carbon (nominally -25‰) fractionates into lighter methane (-60‰) and heavier DIC (+10‰) as it gets buried into deeper sediments. The carbon isotope compositions $\delta^{13}C_{CH_4}$ and $\delta^{13}C_{HCO_3}$ in methane and DIC at the bottom boundary are specified based on their fractionated isotope compositions in deeper sediments.

$$\delta^{13}C_{CH_4}(\tilde{L}_z, \tilde{t}) = \delta^{13}C_{CH_4,ext} = -60\text{‰} \quad \delta^{13}C_{HCO_3}(\tilde{L}_z, \tilde{t}) = \delta^{13}C_{HCO_3,ext} = +10\text{‰}$$

Results and discussions

The hyperbolic organic material balance differential equation is numerically solved using an implicit block centered finite difference scheme. To simulate steady state concentration profiles of methane, sulfate, bicarbonate, calcium, carbon isotopes an explicit numerical scheme is formulated and the organic content profile is updated in time. A single point upstream weighting was used to formulate the sediment and fluid advection terms. Steady state methane and sulfate profiles are shown in Figure 6.8.4(a). For close-up view, the profiles are zoomed into and concentration profiles are shown until normalized depth $\tilde{z} = 0.5$ even though the simulated profiles extend till $\tilde{z} = 2$ which is twice the thickness of the hydrate stability zone. With finite Pe_1 (related to burial and sedimentation) and varying external fluid flux (i.e. varying Pe_2), different profiles are plotted corresponding to different SMT depths. On increasing external fluid flux, SMT is observed to be shallower as previously reported by various authors (Borowski *et al.*, 1996; Bhatnagar *et al.*, 2008). Sulfate concentrations are normalized to seafloor values and methane concentrations are normalized to triple point concentration of methane. The arrow indicates increase in external flux. The profiles show that methane concentration increases with depth and on exceeding local solubility concentration, forms hydrates with the excess methane. Thus, methane gets constrained at the saturated value at the top of gas hydrate layer. The methane coming from below is transported towards the seafloor due to diffusive and fluid flux. The fluid flux increases with increase in magnitude of Pe_2 and the methane transports towards the seafloor before it gets constrained at the SMT to zero methane concentration due to the AOM reaction. Near the SMT the diffusion gradients build up and methane profiles tend to bend towards the zero concentration at the SMT.

The sulfate concentrations have the seawater value at the seafloor and when the concentrations are normalized with the seawater value, they attain a unit value at the seafloor $\tilde{z} = 0$. The pore water sulfate is consumed to near-zero concentrations at the SMT by dissolved methane as a result of the AOM reaction. In this work, pore water sulfate consumption has also been modeled to occur through POC driven reduction occurring in the region between the seafloor and the SMT.

In one case, the methane and sulfate profiles constrain the SMT depth to ~8 mbsf ($\tilde{z} = 0.06$) and the top of gas hydrate to ~80 mbsf ($\tilde{z} = 0.6$) matching the real data from site 1244 represented by red curves ($Pe_2 = -1.0$) in Figure 6.8.4a. The model also computes the DIC, calcium and carbon isotope composition simultaneously with the methane and sulfate concentration profiles. The light blue curves (Figure 6.8.4) represent a case with zero external fluid flux, no AOM, and only POC to consume sulfate in shallow sediments. The red, green and dark blue curves correspond to another case with methanogenesis and AOM reactions, finite fluid flux, but without POC-sulfate reaction. There is a change in slope observed in these profiles at the SMT; which might be explained due to generation of DIC due to the AOM. In these plots, the DIC concentration is normalized to the seawater concentration, therefore, the normalized DIC concentration is unity at the seafloor.

Calcium present in the system precipitates out in the presence of DIC in shallow sediments forming calcium carbonate. The calcium carbonate formation is the sink for DIC and calcium has been modeled as an equilibrium reaction in this work. Calcium is consumed and finally constrained by the finite equilibrium concentration calculated from the solubility product of calcium carbonate. Increased flux results in increased DIC and reduced pore water calcium resulting in increased authigenic carbonate precipitation. The calcium profiles are normalized to seawater calcium concentration and therefore constrained to unity at the seafloor (Figure 6.8.4c).

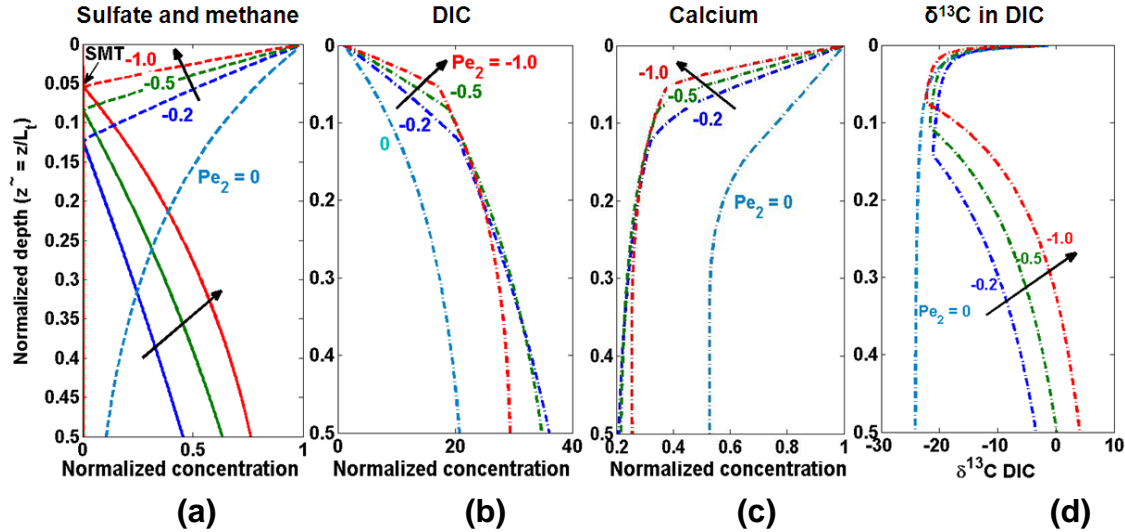


Figure 6.8.4: Normalized concentration profiles at dimensionless time $\tilde{t} = 2.0$. (a) methane, and sulfate, (b) DIC, (c) calcium, (d) $\delta^{13}\text{C}$ in DIC. The arrow shows the direction of increasing fluid flux. Parameters: $\text{Pe}_1=0.04$. The light blue curves represent an example of no fluid flux ($\text{Pe}_2=0$), no AOM ($\text{Da}_{\text{AOM}}=0$), no methanogenesis ($\text{Da}=0$), with just POC reaction. The red, green and blue curves represent concentration profiles for different fluid fluxes with AOM ($\text{Da}_{\text{AOM}}=10^8$), POC ($\text{Da}_{\text{POC}}=10$) and methanogenesis ($\text{Da}=0.86$) reaction.

The carbon isotope composition $\delta^{13}\text{C}$ in DIC is also computed and plotted in Figure 6.8.4d. The normalized carbon isotope in DIC is zero at the seafloor. This reduces to a nominal negative value of $-25\text{\textperthousand}$ as a net result of DIC ($-60\text{\textperthousand}$) generated at the SMT and a deep bicarbonate ($+10\text{\textperthousand}$) source due to methanogenesis in deeper sediments. The $\delta^{13}\text{C}$ in DIC value increases with depth below the SMT and finally gets constrained to more positive values since deeper DIC is enriched in ^{13}C as shown in Figure 6.8.4d. The carbon isotope composition in DIC has something very interesting to note. For zero external fluid flux, no methanogenesis, and no AOM, $\delta^{13}\text{C}$ in DIC value is $-25\text{\textperthousand}$ suggesting dominance of POC reaction. Alternatively, it is observed that with AOM and methanogenesis, and finite flux, $\delta^{13}\text{C}$ in DIC is also $-25\text{\textperthousand}$, as opposed to $-60\text{\textperthousand}$ suggested by various authors (Kastner *et al.*, 2008). The deep flux of DIC from below of $+10\text{\textperthousand}$ mixes with DIC of $-60\text{\textperthousand}$ from the AOM reaction at the SMT and brings the carbon isotope composition to a nominal value of $-25\text{\textperthousand}$.

From our simulation profiles, the deviation of concentration relative to seawater values is plotted. Similar to the zero external fluid flux interpretation (Only POC, no AOM, no fluid flux), the concentration cross-plot lies on the 2:1 line as shown in red circles in Figure 6.8.5a. The 2:1 concentration cross-plot could also result from a combination of AOM, and methanogenesis with very low fluid flux as shown in blue circles (Figure 6.8.5a). AOM generates 1 mole of DIC and consumes 1 mole of sulfate. On the other hand, methanogenesis generates 1 mole of DIC. Overall, these two reactions form 2 moles of DIC and consume 1 mole of sulfate in the system. In fact, below the SMT, the concentration of DIC

increases with no change in sulfate (Figure 6.8.5a). This is due to the DIC flux due to a deep source of DIC as a result of methanogenesis.

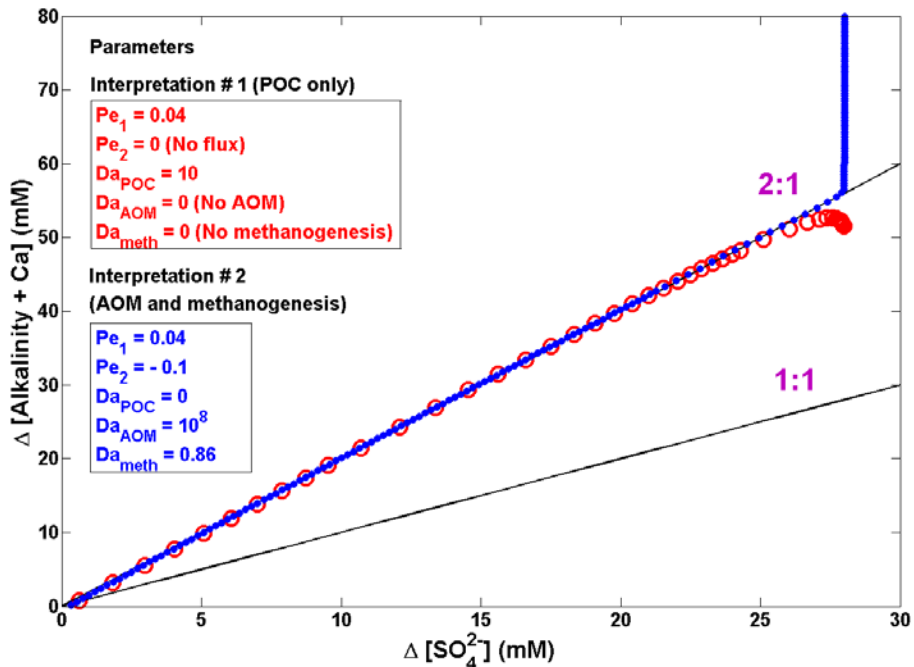


Figure 6.8.5a: Concentration cross-plots for sulfate and DIC relative to seafloor with zero or low upward fluid flux. Parameters: $Pe_1=0.04$. The red circles represent an example of no fluid flux ($Pe_2=0$), no AOM ($Da_{AOM}=0$), no methanogenesis ($Da=0$), with just POC reaction ($Da_{POC}=10$). The blue curve represents an example of low finite flux ($Pe_2=-0.1$), with AOM ($Da_{AOM}=10^8$), methanogenesis ($Da=0.86$), but no POC ($Da_{POC}=0$) reaction. 2:1 correspondence could not only be achieved by POC alone, but also by a combined effect of AOM and methanogenesis.

Therefore, 2:1 slope for DIC and sulfate concentration cross-plot does not necessarily suggest POC driven sulfate consumption reaction. It could also result from combinations of AOM and a deep bicarbonate source (methanogenesis) and fluid flux.

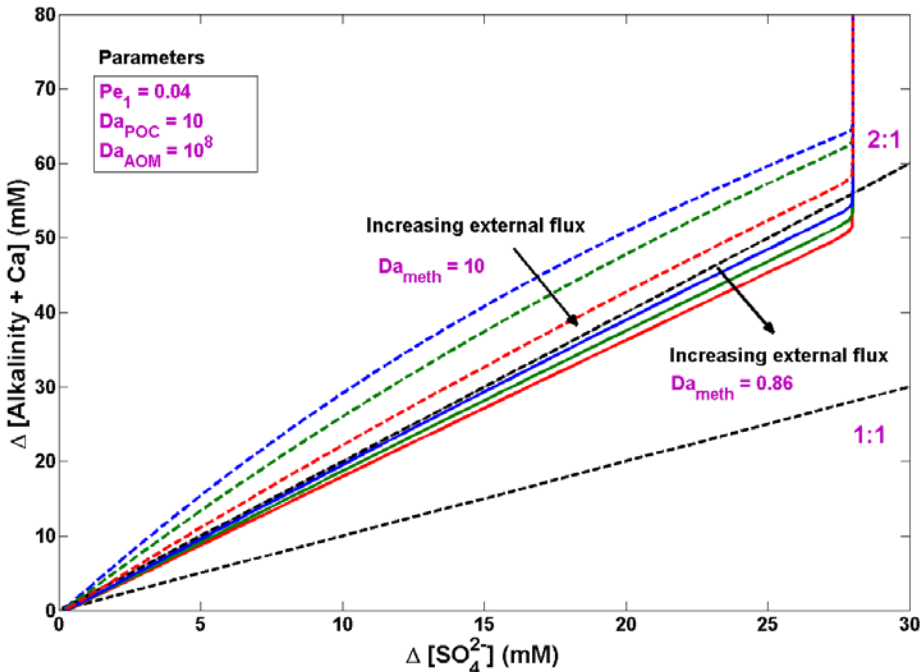


Figure 6.8.5b: Concentration cross-plots for sulfate and DIC relative to seafloor with finite flux and rate of methanogenesis. Parameters: $Pe_1=0.04$, $Da_{AOM}=10^8$, $Da_{POC}=10$. The bold curves represent lower rate of methanogenesis, $Da=0.86$ and dashed curves correspond to a higher rate $Da=10$. On increasing fluid flux the slope of the cross-plot decreases. Higher rate of methanogenesis results in more DIC generation hence the curves are shifted with an increased slope.

On increasing the external fluid flux, the slope of the concentration cross-plots decreases (Figure 6.8.5b). On increasing the rate of methanogenesis, the slope of the concentration cross-plots increases. This increase is because more of DIC is generated with increased methanogenesis (Figure 6.8.5b).

From the computed concentration profiles, gradients are calculated and the diffusive fluxes of DIC and methane relative to sulfate diffusive fluxes at the SMT are plotted in Figure 6.8.6. The red markers represent DIC and blue correspond to methane. Both methane and DIC fluxes show 1:1 correspondence with the sulfate fluxes. This is obviously due to the AOM at the SMT as reported by several authors in the past (Borowski *et al.*, 1996). Even on increasing the rate for POC reaction from zero to 10 does not shift the flux cross-plot from 1:1 line. Squares ($Da_{POC}=10$) and circles ($Da_{POC}=0$) show the two different rates for POC reaction. Notably, that the net DIC flux at the SMT is calculated as a difference in flux coming from deeper sediments and shallow flux going towards the seafloor.

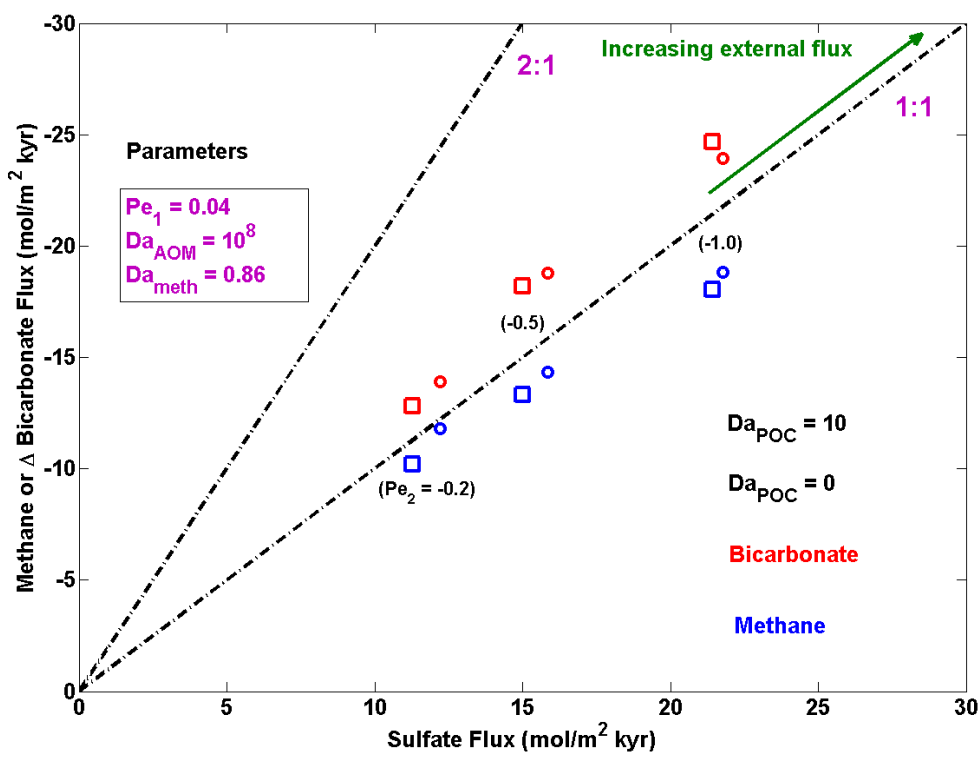


Figure 6.8.6: Flux cross-plots of methane (blue) versus sulfate or DIC (red) versus sulfate across the SMT showing 1:1 correspondence for AOM dominated system. Squares ($D_{a,POC}=10$) and circles ($D_{a,POC}=0$) show the two different rates for POC reaction. Changing the rate of POC reaction does not alter the flux correspond of the above species.

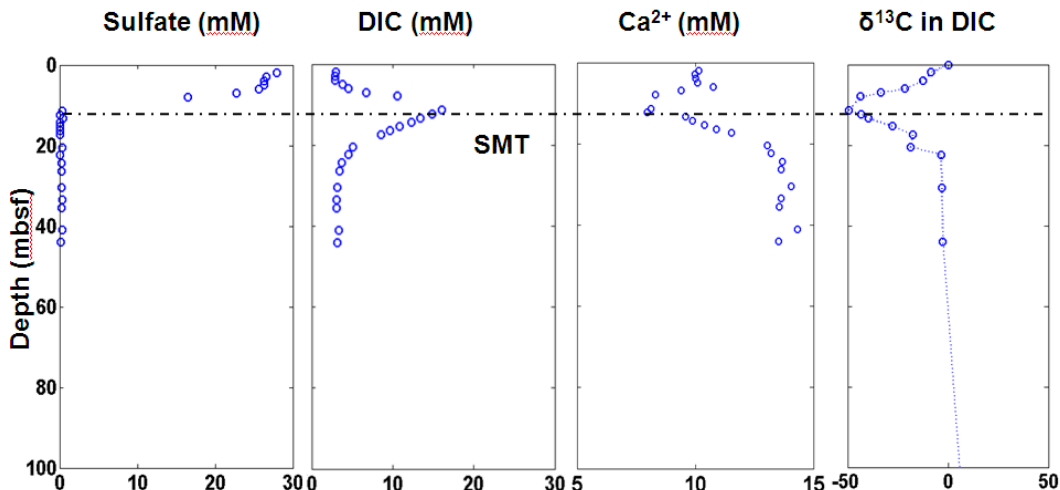


Figure 6.8.7: Sulfate, methane, alkalinity (DIC), calcium concentration profiles and carbon isotope $\delta^{13}\text{C}$ composition in DIC for shallow sediment at site KC151 on Gulf of Mexico (original data from Kastner *et al.*, 2008)

Example site – Gulf of Mexico Keathley Canyon 151

A second example site is simulated from the Gulf of Mexico Keathley Canyon 151 where DIC is the limiting species and calcium is in excess as shown in observed data (Figure 6.8.7). Due to high calcium concentration, DIC gets consumed in deeper sediments. There exists a change in slope at the SMT in the profiles shown in Figure 6.8.7. The DIC concentration increases in the region between the seafloor and the SMT but drops below the SMT. With the help of the numerical model, the concentration profiles were simulated for site KC151 for a given set of parameters (see appendix). From the simulated concentration profiles, the change in DIC and sulfate concentration was cross-plotted, with respect to seawater values as shown in Figure 6.8.8. The concentration cross-plot lie away from the 2:1 line (closer to 1:1 line) and in fact, on increasing the external fluid flux the slope of the cross-plot decreases, similar to what was found at Hydrate Ridge site example (Figure 6.8.5b).

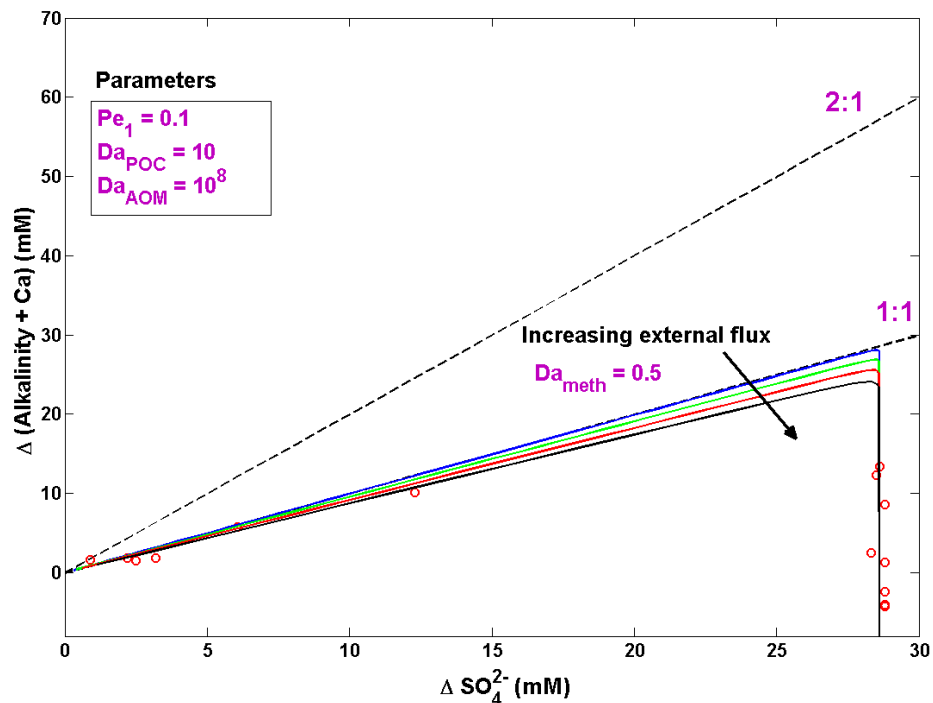


Figure 6.8.8: Concentration cross-plots for sulfate and DIC relative to seafloor with finite flux and rate of methanogenesis. Parameters: $\text{Pe}_1=0.05$, $\text{Da}_{\text{AOM}}=10^8$, $\text{Da}_{\text{POC}}=10$, $\text{Da}=0.5$. The bold curves represent concentration cross-plots for Gulf of Mexico, Keathley Canyon KC151. On increasing fluid flux, the slope of the bold curves decreases. Note that the concentration of DIC drops below the SMT because calcium consumes the DIC at greater depths. Therefore, the concentration cross-plot slope is significantly lower than 2:1.

Conclusions

The modeling shows us that a 2:1 correspondence in concentration cross-plot for alkalinity and sulfate is not limited to POC driven sulfate reduction. The 2:1 concentration cross-plot could also result from combinations of AOM, methanogenesis, and fluid flux.

On increasing the external fluid flux the slope of the concentration cross-plot decreases. Higher rate of methanogenesis results in more DIC generation hence the curves are shifted with an increased slope. A trade-off of fluid fluxes and rate of methanogenesis decides whether the concentration cross-plot lies on 2:1 or not.

The $\delta^{13}\text{C}$ values in DIC are significantly more positive than -60‰ (e.g. -22‰) and can result from the combined input of AOM and a deep bicarbonate source (from methanogenesis).

Flux cross-plot of methane versus sulfate or DIC versus sulfate across the SMT lie on the 1:1 slope, if dominated by AOM. For AOM dominated systems, the SMT depth can be used as a proxy to determine the upward methane flux above marine gas hydrate sediments.

References

- Berner, R. A. (1980), *Early Diagenesis: A Theoretical Approach*, Princeton Univ. Press, 213 Princeton, NJ
- Bhatnagar, G., Chatterjee, S., Chapman, W. G., Dickens, G. R., Dugan, B., and Hirasaki, G. J. (2010), Analytical theory for relating depth of the sulfate-methane transition to gas hydrate saturation (in preparation), to be submitted to *Geochemistry, Geophysics, Geosystems*
- Bhatnagar, G., Chapman, W. G., Dickens, G. R., Dugan, B., and Hirasaki, G. J. (2008), *Sulfate-methane transition as a proxy for average methane hydrate saturation in marine sediments*, *Geophys. Res. Lett.*, 35, L03611, doi:10.1029/2007GL032500
- Bhatnagar, G., Chapman, W.G., Dickens, G.R., Dugan, B. and Hirasaki, G.J. (2007), *Generalization of gas hydrate distribution and saturation in marine sediments by scaling of thermodynamic and transport processes*, *Am. J. Sci.*, 307: p 861-900
- Boudreau, B. P., and J. T. Westrich (1984), *The dependence of bacterial sulfate reduction on sulfate concentration in marine sediments*, *Geochim. Cosmochim. Acta*, 48, 2503-2516
- Borowski, W. S., Paull, C. K., and Ussler III, W. (1999) *Global and local variations of interstitial sulfate gradients in deep-water, continental margin sediments: Sensitivity to underlying methane and gas hydrates*, *Mar. Geol.*, 159:131–154
- Borowski, W. S., C. K. Paull, and W. Ussler III (1996), *Marine pore-water sulfate profiles indicate in situ methane flux from underlying gas hydrate*, *Geology*, 24(7), 655-658

Buffett, B. A. and Archer, D. (2004), *Global inventory of methane clathrate: Sensitivity to changes in the deep ocean*, *Earth Planet. Sci. Lett.*, 227:185–199

Davie, M. K. and Buffett, B. A. (2001), *A numerical model for the formation of gas hydrate below the seafloor*, *J. Geophys. Res.*, 106:497–514

Dickens, G.R., Snyder, G. (2009), *Interpreting upward methane flux*, *Fire in the Ice*, Winter, p 7-10

Dickens, G. R. (2001), *The potential volume of oceanic methane hydrates with variable external conditions*, *Org. Geochem.*, 32:11791193

Kastner, M., Torres, M., Solomon, E., and Spivack, A. J. (2008), *Marine pore fluid profiles of dissolved sulfate: do they reflect in situ methane fluxes?* *Fire in the Ice*, Summer, p 6-8

Li, Y., and Gregory, S., 1974, Diffusion of ions in sea water and in deep-sea sediments: *Geochimica et Cosmochimica Acta*, v. 38: 703–714

Paull, C. K., W. Ussler III, T. Lorenson, W. Winters, and J. Dougherty (2005), *Geochemical constraints on the distribution of gas hydrates in the Gulf of Mexico*, *Geo. Mar. Lett.*, 25: 273-280

Tréhu, A. M., Long, P. E., Torres, M. E., Bohrmann, G., Rack, F. R., Collett, T. S., et al., (2004), *Three-dimensional distribution of gas hydrate beneath southern Hydrate Ridge: Constraints from ODP Leg 204*, *Earth Planet. Sci. Lett.*, 222: 845–862

Tréhu A. M., Bohrmann G., Rack F. R., Torres M. E., et al., (2003), *Proc. ODP, Init. Repts.*, vol. 204; College Station, TX (Ocean Drilling Program), 1–132 doi:10.2973/odp.proc.ir.204.103.2003

Whiticar M., J., (1999), Carbon and hydrogen isotope systematics of bacterial formation and oxidation of methane, *Chemical Geology*, 161: 291–314

Appendix C

Table 1 – Model parameters

Symbol	Definition (units)	Hydrate Ridge 1244	Keathley Canyon 151
-	Seafloor depth (m)	890	1300
T_0	Seafloor temperature ($^{\circ}$ C)	3.8	4
G	Geothermal gradient ($^{\circ}$ C/m)	0.061	0.038
L_t	Depth to GHSZ (mbsf)	133.4	316.5
L_s	Depth to SMT (mbsf)	8.5	9
$C_{m,eqb}$	Methane solubility at base of hydrate stability zone	1.701×10^{-3}	2.11×10^{-3}
D_m	Methane diffusivity (m^2/s)	0.87×10^{-9}	

D_s	Sulfate diffusivity (m^2/s)	0.56×10^{-9}	
D_b	DIC diffusivity (m^2/s)	0.60×10^{-9}	
D_{ca}	Calcium diffusivity (m^2/s)	0.40×10^{-9}	
λ	Rate of methanogenesis	5×10^{-14}	
\dot{S}	Sedimentation rate (cm/kyr)	27	25
$U_{f,sed}$	Fluid flux due to sedimentation (m/s)	2.85×10^{-13}	2.64×10^{-13}
$\tilde{\rho}_{sed}$	Normalized sediment density	2.57	
α_o	TOC (%)	1.5	0.5
β	Normalized organic content in seafloor	2.2	0.59
Pe_1	Peclet number	0.04	0.1
Pe_2	Peclet number	-0.2, -0.5, -1.0	-1.0, -2.0, -5.0
Da	Damkohler number (methanogenesis)	0.86	0.5
Da_{POC}	Damkohler number (POC)	10	
Da_{AOM}	Damkohler number (AOM)	10^8	

Table 2 - Notations

c_i^j, \tilde{c}_i^j	Mass fraction of component i and corresponding normalized value in phase j
$c_{m,eqb}$	Methane mass fraction in pore water at the base of gas hydrate stability zone (BHSZ)
D_m, D_s, D_b, D_{Ca}	Diffusivities of methane, sulfate, DIC, and calcium
Da_{AOM}, Da_{POC}, Da	Damkohler number for AOM, POC and methanogenesis reactions
L_t, L_s	Depth to base of GHSZ, Depth to SMT
$M_{CH_4}, M_{SO_4}, M_{HCO_3}, M_{Ca}, M_{POC}$	Molecular weight of methane, sulfate, DIC, calcium, and POC, respectively
Pe_1, Pe_2	Peclet numbers for compaction driven and external fluid flow
t, \tilde{t}	Dimensional time and dimensionless time, respectively
U_f, U_s	Net fluid flux and sediment flux, respectively
\tilde{U}_f, \tilde{U}_s	Dimensionless net fluid flux and sediment flux, respectively
$U_{f,sed}, U_{f,ext}$	Fluid flux due to sedimentation-compaction and upward external flow, respectively
v_s	Sediment velocity
z, \tilde{z}	Vertical depth and normalized vertical depth, respectively

$\alpha, \tilde{\alpha}$	Organic content in sediment and normalized value, respectively
α_o, β	Organic content in seafloor and normalized value, respectively
$\delta^{13}_{\text{CH}_4}, \delta^{13}_{\text{HCO}_3}$	$\delta^{13}\text{C}$ in methane and DIC, respectively
$\delta^{13}_{\text{CH}_4, \text{meth}}$	$\delta^{13}\text{C}$ in methane in methanogenesis reaction
$\delta^{13}_{\text{HCO}_3, \text{meth}}, \delta^{13}_{\text{HCO}_3, \text{POC}}$	$\delta^{13}\text{C}$ in DIC for methanogenesis and POC driven sulfate consumption reaction, respectively
$\phi, \tilde{\phi}$	Sediment porosity and reduced sediment porosity, respectively
ϕ_o, ϕ_∞	Sediment porosity at seafloor and minimum porosity at depth, respectively
γ, η	Reduced porosity parameters
$\lambda, \lambda_{\text{AOM}}, \lambda_{\text{POC}}$	Rate of methanogenesis, AOM and POC driven sulfate consumption
$\rho_i, \tilde{\rho}_i$	density of the phase i and normalized value, respectively

Table 3 - Subscripts and superscripts

$m, s, b, Ca, CaCO_3, w, sed$	methane, sulfate, DIC, calcium, calcium carbonate, water and sediment components, respectively
l	liquid phase

Journal articles (draft manuscript) - Prepared the first draft for our manuscripts

1. "Pore water chemistry profiles across SMT above marine gas hydrates systems: A numerical modeling perspective" to be submitted to *Journal of Geophysical Research* (Chatterjee et al.)
2. "Analytical theory for relating depth of the sulfate-methane transition to gas hydrate saturation" to be submitted to *Geochemistry, Geophysics, Geosystems* (Bhatnagar et al.)

Conference presentations

1. S. Chatterjee, G. Bhatnagar, W. G. Chapman, G. R. Dickens, B. Dugan, G. J. Hirasaki, "Sulfate, Alkalinity, Calcium and Carbon isotope $\delta^{13}\text{C}$ profiles as an indicator of upward methane flux", (oral presentation) American Geophysical Union (AGU) Fall meeting, San Francisco, CA, December 2009

2. S. Chatterjee, G. Bhatnagar, W. G. Chapman, B. Dugan, G. R. Dickens, G. J. Hirasaki, "Carbon cycling across sulfate-methane transition above marine gas hydrate systems", (oral presentation) Society of Petroleum Engineers (SPE) Gulf-coast regional student paper contest, Lubbock, TX, April 2010
3. S. Chatterjee, G. Bhatnagar, W. G. Chapman, B. Dugan, G. R. Dickens, G. J. Hirasaki, "Sulfate-Methane Transition depth as a proxy for methane flux above gas hydrate systems", (poster) Gordon Research Conference – Natural gas hydrate systems, Waterville, ME, June 2010
4. G. Gu, G. J. Hirasaki, W. G. Chapman, S. Chatterjee, B. Dugan, G. Bhatnagar, C. Zelt, Gerald Dickens, Priyank Jaiswal, 2-D Simulation on Hydrate Accumulation in different heterogenous lithology Structures, (Poster), Gordon Research Conference – Natural gas hydrate systems, Waterville, ME, June 2010
5. B. Dugan, H. Daigle, S. Chatterjee, G. Gu, G. Hirasaki, Continuum models of large-scale phenomena associated with hydrate-bearing sediments, (oral presentation) Gordon Research Conference – Natural gas hydrate systems, Waterville, ME, June 2010

DOE methane hydrate meeting, Georgia Tech University, Atlanta, GA

6. *Carbon cycling across SMT above marine gas hydrates systems: A numerical modeling perspective* – Monday Jan 25, 2010
7. *Effect of lithologic heterogeneity on gas hydrate distribution* – Wednesday Jan 27, 2010

Subtask 6.5: *Processes leading to overpressure*

Modeling (in)stability by including slope stability calculations during hydrate accumulation and collaborating with Task 8.

Subtask 6.6: *Concentrated hydrate and free gas*

Accumulation of gas hydrate and free gas is being modeled in heterogeneous marine sediments over geologic time scales. The two-dimensional numerical model incorporates deposition and compaction of heterogeneous sediments, methane generation, and migration of water with dissolved gas. Fracture network systems and dipping sand layers are common examples of lithologic heterogeneities in natural gas hydrate systems, and are simulated using the current 2-D model. Increased fluid flux within these high permeability conduits results in concentrated hydrate deposits. Simulations are also currently being done with multiple fracture network column and parallel sand layers.

The student revisited subtask 6.8 and this work was temporarily stalled for a year. We have now completed subtask 6.8(b) and reverted back to this task. It is expected to complete this subtask by summer 2011.

Subtask 6.8 (b): Sulfate, bicarbonate, calcium and carbon isotope ($\delta^{13}\text{C}$) balance as an indicator of methane flux

Revisited the 1-D model to resolve the conflict between Kastner and Dickens to understand how sulfate, bicarbonate, calcium and carbon isotope act as indicators for upward methane flux in marine sediments. Revisiting the 1-D problem was a good preparation for Sayantan Chatterjee who was trying to learn the simulation code developed by the former student, Gaurav Bhatnagar. It was also helpful for the more complex 2-D work (subtask 6.6) we are committed to do.

Completed this subtask and drafted our manuscript to be published by the end of summer 2010.

Task 7: Analysis of Production Strategy

J. Phirani & K. K. Mohanty, University of Texas at Austin

1. Summary of Research Completed in Budget Period 4

In this work, we have developed mechanistic models for transport properties for hydrate bearing sediments. Hydrate deposition and dissociation is modeled in a single pore to develop pore-scale laws of hydrate occupancy. Pore size distributions are found for sediments containing different particle size distributions. Pore size distribution is modified due to hydrate deposition. Percolation theory is used to numerically calculate effective transport properties at different hydrate and water saturations. The transport properties calculated from these mechanistic models can replace the empirical correlations in reservoir simulations of hydrate reservoirs.

A large deposit of gas hydrate was discovered last year in the Gulf of Mexico (GOM) block AC 818. We have worked on assessing the production from this block using a thermal, compositional, 3-D simulator in an equilibrium mode. Four components (water, methane, hydrate and salt) and four phases (gas, aqueous-phase, hydrate and ice) are considered where salt is assumed to be in aqueous phase only. The reservoir GOM, block AC 818 is reported to be an unconfined reservoir. For these types of reservoirs, depressurization is ineffective and warm water flooding is necessary for production. We study different well configurations for production from this hydrate reservoir using warm water flooding. Vertical wells, horizontal wells and a combination of both are considered. Horizontal wells increase the area of sweep by warm water in hydrate bearing sediments and increase the gas production to 48% of original gas in place as compared to 15% produced by using vertical wells. Positions of horizontal wells with respect to the aquifer also play an important role in production.

1.1 Subtask 7.1: Pore-scale Model for Lithology, Petrophysical and Thermophysical Parameters

Spherical particles of Gaussian radius distributions were packed using the DEM method. The pore throat radius distribution was determined after Delaunay triangulation. The pore throat distribution of the porous medium formed by the particles having Gaussian particle radius distribution is given by Rayleigh distribution. Table 1 shows the different distributions studied.

Particle size distribution		Radius distribution
Mean (μm)	Variance (μm)	σ (μm)
200	50	33.71
200	75	58.46
200	100	157.4
100	50	88.1
50	50	13.86

Table 1: Particle and pore radius distribution of sphere packs

Figure 1 shows the water and gas relative permeabilities from percolation theory for the base case porous medium with zero hydrate saturation when variance σ for Rayleigh distribution is 157.

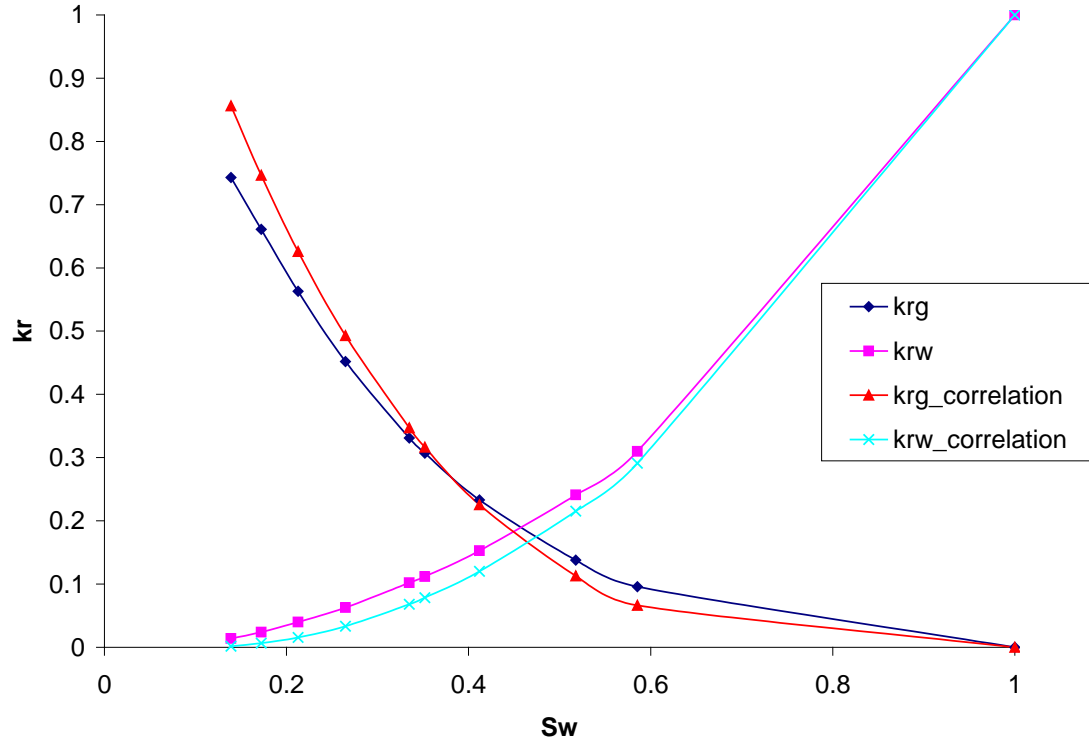


Figure 1: Relative permeability of the sediment without hydrate

The following correlation is developed for relative permeability by matching the results of the percolation theory:

$$k_{rw} = \left(\frac{S_w - S_{wr}}{1 - S_{wr}} \right)^2 \quad (1a)$$

$$k_{rg} = \left(\frac{1 - S_w}{1 - S_{wr}} \right)^{3.5} \quad (1b)$$

where k_{rw} is relative permeability of water or the wetting phase and k_{rg} is relative permeability of gas or the nonwetting phase.

Figure 2 shows the relative permeability obtained from percolation theory for the base case at different hydrate saturations. The curvature of relative permeability curves increase with increasing hydrate saturation.

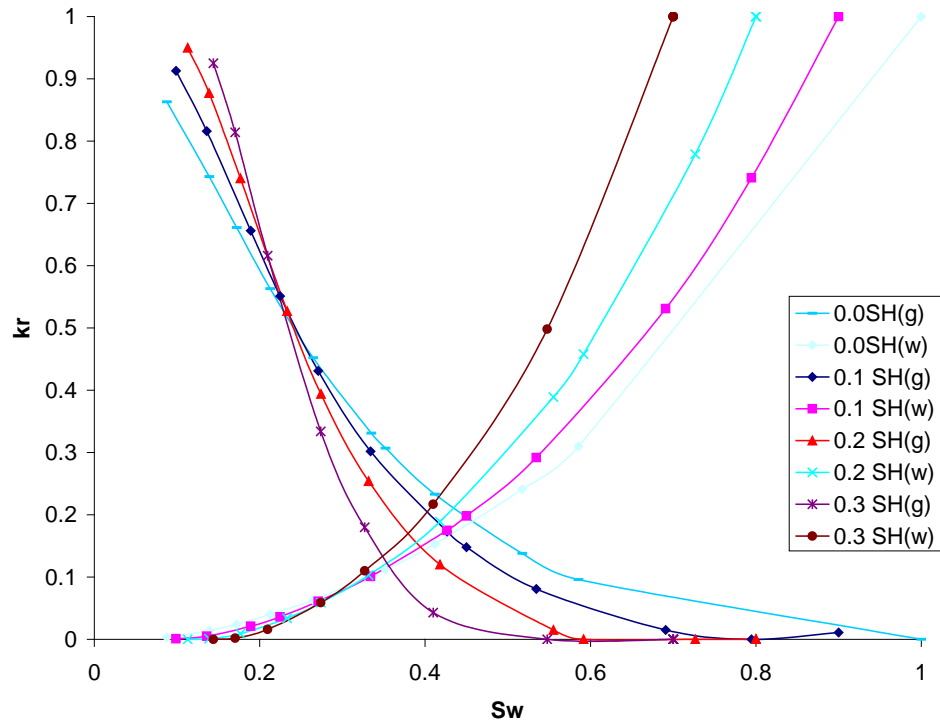


Figure 2(a): Relative permeability curves for different hydrate saturations

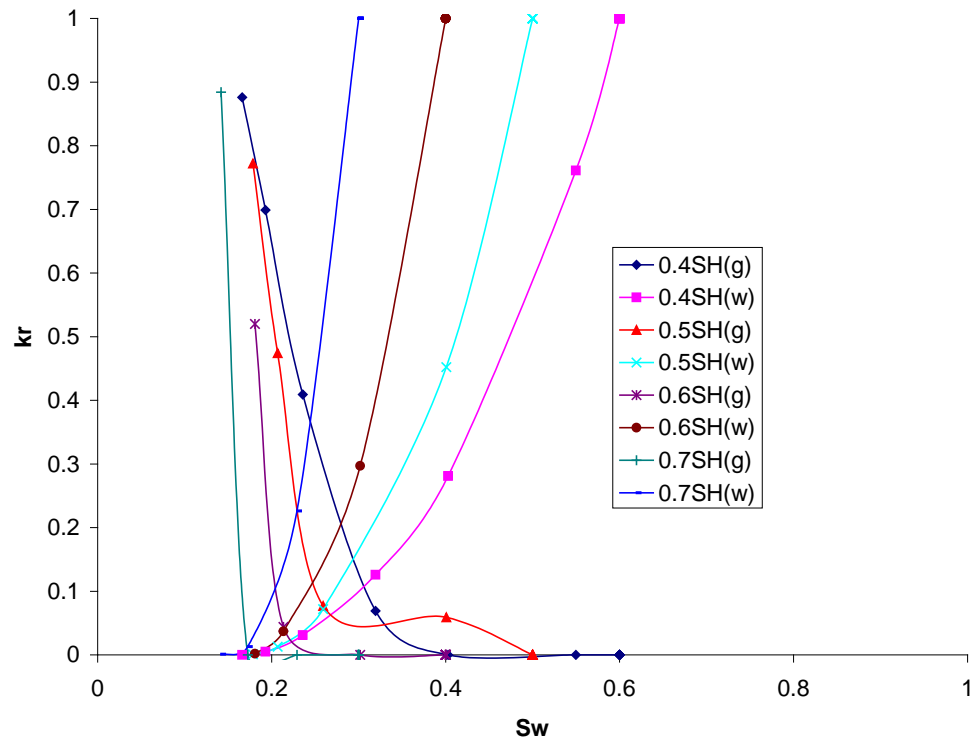


Figure 2(b): Relative permeability curves for different hydrate saturations

A correlation was developed between the computed relative permeability and hydrate saturation. The following correlation finds the best fit with the percolation theory results.

$$k_{rw} = \left(\frac{S_w - S_{wr}}{1 - S_H - S_{wr}} \right)^{(2+2S_H)}$$

(2a)

$$k_{rg} = \left(\frac{1 - S_H - \beta S_w^\alpha}{1 - S_H - S_{wr}} \right)^{(3.5-S_H)}$$

(2b)

$$\begin{aligned} \alpha &= 2, S_H \geq 0.5 \\ &= 1, S_H \leq 0.2 \end{aligned}$$

(2c)

$$\begin{aligned} &= 3.25S_H + 0.425, 0.2 < S_H < 0.5 \\ \beta &= 10S_H - 1, S_H > 0.1 \\ &= 1, S_H \leq 0.1 \end{aligned}$$

(2d)

Figure 3 shows comparison of relative permeability curves for 2 hydrate saturations (0.4 and 0.6) obtained from percolation theory and the correlations developed in Eq. (2).

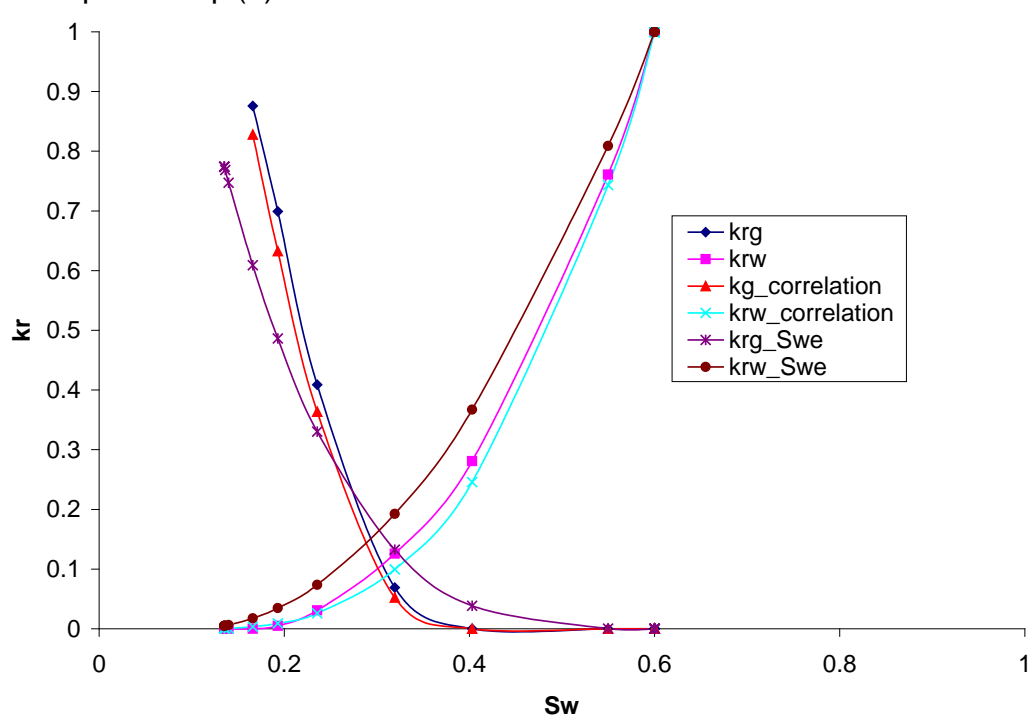


Figure 3(a): Relative permeability of the sediment for hydrate saturation 0.4

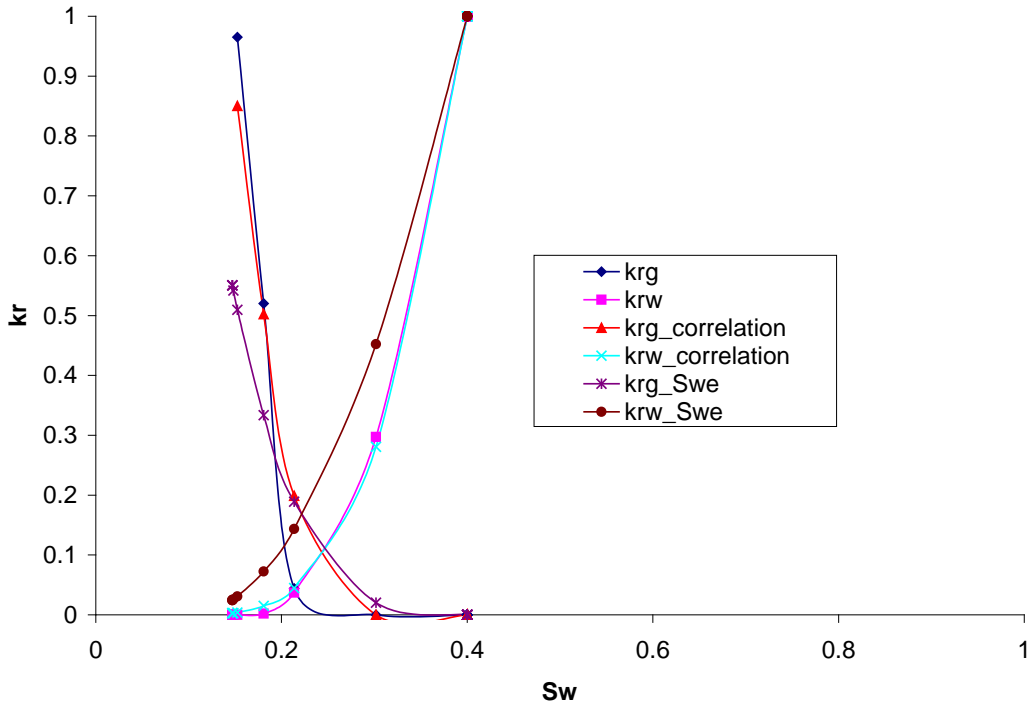


Figure 3(b): Relative permeability of the sediment for hydrate saturation 0.6
This shows that the correlation in equation 2 is valid for normal distribution of particle size which gives Rayleigh pore radius distribution.

1.2 Subtask 7.2: Evaluation of Production Strategy

The block AC 818 in the Gulf of Mexico is a 1200m long and 500m wide reservoir. It has an 18m thick hydrate layer which is underlain by an infinite aquifer. In the hydrate zone, hydrate saturation is 0.75 and water saturation is 0.25. Initial pressure at the bottom of the reservoir is 31.4MPa and initial temperature is 294.88K which vary in the reservoir according to hydrostatic pressure drop and geothermal gradient, respectively. To model the infinite aquifer a 12m thick aquifer zone is considered for simulation in which the bottom most 3m layer was assumed to have a permeability 1/10th of the hydrate layer absolute permeability. The water saturation is 1.0 for the aquifer layer. For overburden, no mass flow is allowed while heat can transfer with a specified heat transfer coefficient. At the under-burden, we have an infinite aquifer, so, heat transfer is allowed and the pressure is specified at the bottom boundary. The water can come into the reservoir or go out according to the pressure difference between the bottom most grid layer and the boundary pressure. For lateral boundaries no heat or mass flow is considered, due to symmetry.

Different well configurations considered for production from this reservoir are described below:

1. Vertical wells: It is assumed that the reservoir will be developed in a 5-spot pattern and a quarter of a 5-spot pattern is studied. The reservoir is discretized by $50 \times 25 \times 10$ gridlocks.
2. Horizontal wells: Horizontal injectors and producers are considered along the length which are 250m apart. Different positions for horizontal wells are considered.
3. Vertical injector and horizontal producer: The gas dissociated from hydrates rises due to gravity. So, a horizontal production well is considered at the top of the hydrate layer while a vertical injector is placed at the corner of the reservoir, as shown in the figure. The reservoir is discretized by $25 \times 12 \times 10$ gridlocks.
4. Vertical producer and horizontal injector: The injected water drains down due to gravity. So, a horizontal injector at the top of the reservoir and a vertical producer at the corner are considered, as shown in the figure.

Figure 4 shows the production as a percentage of the original gas in place for different well configurations. For all the well configurations, the well temperature and pressure conditions are kept the same. The injection well injects water at 50°C and at a pressure of 50MPa. The producer well pressure is maintained at 4 MPa. With a five spot pattern, the total production is similar to the warm water flooding of an unconfined reservoir, as shown by Phirani et al. (2009), even though the reservoir, injection and production conditions are entirely different. We are able to produce about 15% of the original gas in place when the vertical wells penetrate or do not penetrate the aquifer layer as shown by ‘vertical_wells’ and ‘short_vertical_wells’, respectively. We are able to produce more gas when horizontal wells are used. Different configurations for horizontal wells are used. In hydrate reservoir, for warm water injection we inject water and produce gas. The water drains down due to gravity and gas rises up due to gravity. So the first case we study is with both the injector and producer wells on the top of hydrate bearing zone, shown by ‘horizontal_wells_top’. The horizontal wells are 1200m long and are located in the 3rd grid block layer from the longitudinal sides. The production curve shows that the gas production in the first 700 days is negligible; so different positions of the horizontal wells are studied. The case ‘horizontal_wells_mid’ shows the production curve when both the horizontal wells in the middle of the hydrate bearing zone. In this case the production begins a little earlier than the previous case. Though we are injecting water, because the temperature of injection water is more than reservoir temperature, the water injected also rises due to the density difference. So we simulate the case where the production well is at the top of hydrate bearing zone while the injection well is below the hydrate bearing zone, as shown by ‘producer_up_injector_down’. In this case we are able to produce from the beginning but the final gas production is similar to the previous cases with about 47% of OGIP produced. If we increase the distance between the horizontal wells and the wells are located on the extremes, then the production rate and total production decreases as shown in the case ‘producer_up_injector_down_onsides’.

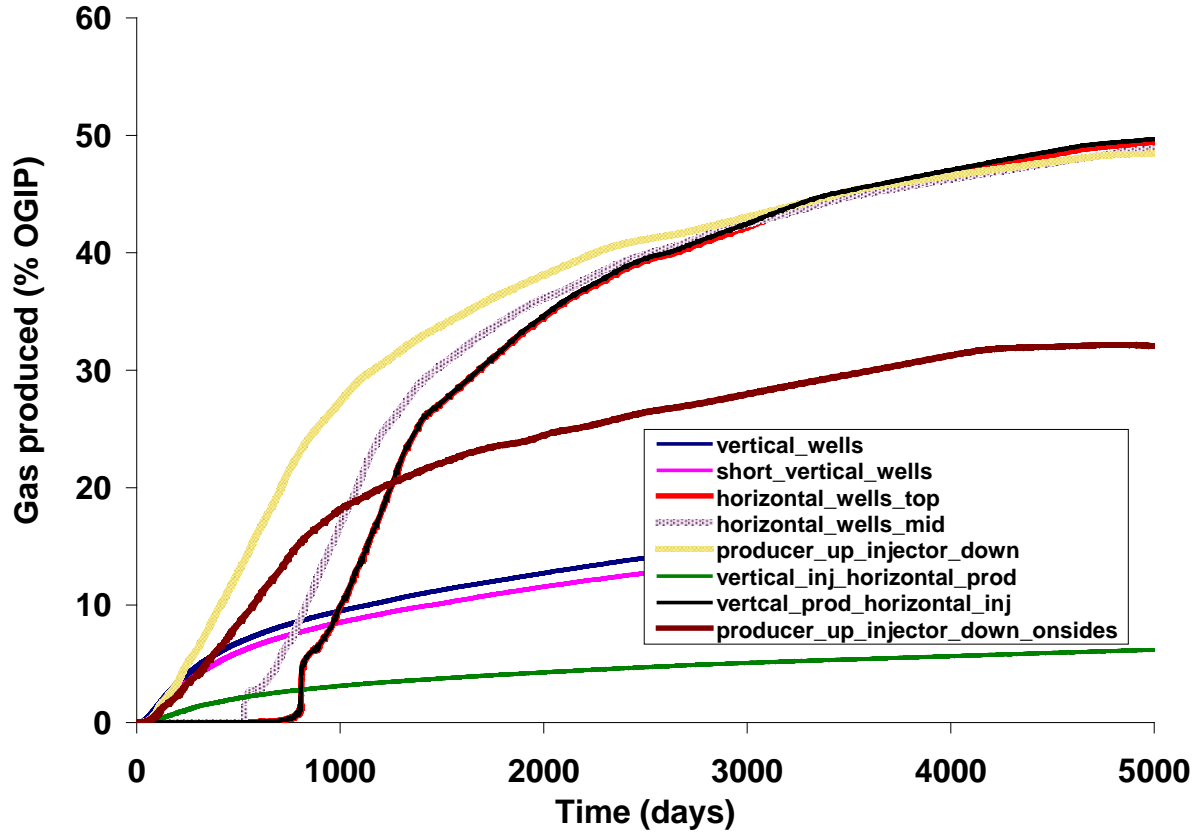


Figure 4: Production curves for different well configurations

Two more cases are studied where a combination of vertical and horizontal wells is considered. The production curve for ‘vertical injector and horizontal producer’ is shown by ‘vertical_inj_horizontal_prod’. The total production for this case is least of all the cases. But when we have horizontal injector and vertical producer shown by ‘vertical_prod_horizontal_inj’ the production curve is similar to the horizontal well case.

Vertical Wells

When both wells are vertical, we consider a 5-spot pattern in the reservoir and simulate a quarter of the pattern. In the simulation domain, we have one injection and one production well in the reservoir. We simulate two cases of the 5-spot

pattern. In one case, the vertical wells penetrate the aquifer zone ('vertical_wells' in Figure 4) and in another, they do not penetrate the aquifer zone ('short_vertical_wells' in Figure 4). We are able to produce about 18% of the OGIP. This is because both the vertical wells are connected to the infinite aquifer and water flow is easier in the aquifer as compared to hydrate bearing layer because the presence of hydrates reduces the permeability. The easier water flow helps in warm water convection in the first case and the production is a little higher than the second case. But after about 500 days most of the water goes into the infinite aquifer and horizontal sweep of warm water slows down.

Horizontal wells

Injector and producer at the top

Figure 4 shows that we can get about 48% of OGIP if we use horizontal wells. Different configurations of horizontal wells are studied. Figure 1c shows the position of the horizontal wells when both the wells are at the top. The production curve for this configuration is shown in Figure 4 as 'horizontal_wells_top'. Before 700 days, the gas production is negligible. This is because the injector is in hydrate bearing low permeability zone. This decreases the injectivity of warm water in the system and initial heating of the reservoir happens by only conduction. After some of the hydrates near the well region dissociate, the convection of warm water becomes easy and hydrate dissociation rate increases.

Horizontal wells in the middle

To increase the initial production, we move the horizontal wells near the aquifer layer to the middle of the hydrate bearing zone. The production curve for this case is shown by 'horizontal_wells_mid'. The production in this case starts at about 500 days. Injection water is lighter than the water present in the reservoir and hence water rises; final production of gas is again about 48% of OGIP. As the warm water rises due to gravity, we can use injection well at the bottom of the hydrate bearing layer and producer at the top as gas also rises due to gravity.

Injector at bottom-producer at top

In this case the injection well is near the infinite aquifer which makes the warm water flow easy. Figure 4 shows that we are able to produce significant amount of gas from the beginning but the final production is about 48% of OGIP (case 'producer_up_injector_down'). The final production is similar in all the cases of horizontal wells. The total production is governed by the hydrate bearing area that warm water is able to sweep, which depends on horizontal convection of warm water. In all the cases this is similar. We also study the production from combinations of vertical and horizontal wells, which includes two cases: vertical injector-horizontal producer and vertical producer-horizontal injector.

Vertical and Horizontal Wells

Vertical injector-horizontal producer

In this case, we have a horizontal producer, which tries to depressurize the reservoir at 4MPa and the producer is not directly connected to the infinite aquifer. The injector injects water at 50C at a pressure of 50MPa. The initial hydrate saturation is 0.75, which is very high and decreases the permeability of hydrate bearing zone to a great extent. This reduces the water productivity of the horizontal well and the pressure does not drop to gas stable zone even in the near well regions. The production well is at the top of hydrate bearing layer about 120m from the right side. In this case warm water can not reach faces away from the vertical injection well leading to low gas production as shown in Figure 4. Another reason of low production in this case is that the wells are not aligned as in the case of two vertical wells where pressure drop along the wells help in horizontal convection of the warm water. The total gas production in this case is less than 10% of OGIP.

Vertical producer-horizontal injector

Figure 4 shows that for this case ‘vertical_prod_horizontal_inj’, the production curve is similar to that of the horizontal wells at top. In this case, we have injector at the top. This is because most of the production is due to the thermal stimulation by warm water. With a horizontal injection well, we are able to sweep the same area of the reservoir.

Sensitivity to distance between the horizontal wells

If the horizontal wells are on the extreme ends of the reservoir, i.e., we increase the distance between the wells. Figure 4 case ‘producer_up_injector_down_onsides’ shows that the total production decreases as the area swept by the wells decrease. We compare the case ‘producer_up_injector_down’.

1.3 Significant Accomplishments

1. Development of a pore-level model to estimate the petrophysical properties of hydrate bearing sediments (**Subtask 7.1**)
2. Evaluation of gas production from an unconfined Gulf of Mexico hydrate reservoir by warm water injection. (**Subtask 7.2**)
3. We have written four papers (SPE 124882, SPE134178, Energy & Fuels, Chemical Engineering Science).

1.4 Conclusions

- When hydrates deposit from a solubilized brine phase, hydrates deposit on walls of pore and pore-scale hydrate saturation is independent of size.

- Normal distribution of particle size of spherical sediments gives Rayleigh distribution of pore throat radius.
- For Rayleigh throat radius distribution, relative permeability matches Corey correlation with $n_g = 3.5$ and $n_w = 2$.
- With increasing hydrate saturation, the gas exponent n_g decreases and water exponent n_w increases.
- Using effective fluid saturations to calculate relative permeability in the presence of hydrates does not agree with calculated relative permeabilities.
- The vertical wells for the unconfined case are less efficient than the horizontal wells. Horizontal wells increase the area of sweep of hydrate bearing sediments leading to more production.
- If the wells are located in the hydrate-bearing zone, the low permeability of the region leads to a low gas production in the initial period. If the injection well is near the aquifer layer, the convection of water becomes easy and the gas production is nonzero from the beginning.
- Increasing the distance between the horizontal wells decreases the amount of hydrate dissociated in the whole reservoirs and gas production decreases.

1.5 Publications

1. Phirani, J., Mohanty, K. K. & G. Hirasaki, "Warm Water Flooding of Unconfined Gas Hydrate Reservoirs," *Energy & Fuels* (2009), doi:10.1021/ef900291j.
2. Phirani, J., Pitchumani, R., & Mohanty, K. K., "Transport Properties of Hydrate Bearing Formations from Pore-Scale Modeling," SPE 124882, Proceedings of SPE ATCE, New Orleans, LA, Oct. 4-7, 2009.
3. Phirani, J. & Mohanty, K. K., "Kinetic Simulation of CO₂ Flooding of Methane Hydrates," SPE 134178, Proceedings of SPE ATCE, Florence, Italy, September 19-22, 2010.
4. Phirani, J., Hirasaki, G., & Mohanty, K. K., "Production Strategy for an Unconfined Marine Hydrate Reservoir," submitted to *Chem. Eng. Sci.* (2010).

Task 8: Seafloor and Borehole Stability: Hugh Diagle and Brandon Dugan

Summary

We focused on modeling of sediment instability associated with hydrate accumulations (Subtask 8.2) that builds on our work of sediment-hydrate properties (Subtask 8.1) because the models use these properties as inputs. We have submitted a database of papers on physical properties (Subtask 8.1). We are continually extending our collaborations and data integration (Subtask 8.3) as we test the instability models against field data collected by DOE, IODP, and other international programs.

Subtask 8.2 has been the most prosperous building on data from Subtask 8.1 and discussions associated with Subtask 8.3. From the information gathered, we have concentrated on different scales of failure in gas hydrate systems ranging from bed-scale fracture genesis to regional-scale slope failure (Subtask 8.2). This work is providing constraints on what drives different types of failure, and helping us characterize the controls on heterogeneous hydrate accumulations. For example, we are quantifying how permeability contrasts enhance hydrate accumulations in coarse, permeable sediment and also increases the potential for failure in finer-grained systems. This has led to our involvement in other hydrate collaborations with the Chevron Gulf of Mexico JIP, hydrate studies in China, and hydrate studies in Cascadia (building on Subtask 8.3 and general collaborations within DOE and outside of DOE).

Milestone Status

- 8.1c Complete database – a review paper of physical properties of gas hydrate bearing sediment has been published (Waite et al., 2009) and a digital database has been submitted to NETL.
- 8.2a Link database with models – models for slope stability and fracture genesis are using properties based on the database. We have employed 1D and 2D models for slope stability and fracture genesis based on observed and characterized properties. This has led to a general understanding on failure that is being tested against field data. It has also emphasized the necessity for reliable permeability models to accurately understand hydrate distribution, accumulation, and saturation.
- 8.2b Add sediment stability to models – initial stability models for slope failure and fracture genesis have been implemented and are being tested. We are now testing against field data and will soon begin sensitivity analysis and summary. Fracture genesis models have been developed in 1D for dissolved-phase and free-gas phase models; slope failure models exist in 2D and are being extended to include advective flux for deep-sourced methane as initial studies suggest this is important. Presentations on these stability models are planned for the Gordon Conference on Natural Gas Hydrate in June 2010 at which time sensitivity/parameter studies

based on observations. A fracture-genesis manuscript has been accepted in the Journal of Geophysical Research (Daigle and Dugan, accepted).

8.2c Conditions for (in)stability – We developed new models on fracture genesis that were not in the original proposal, but that were deemed important when looking at hydrate distribution in fine-grained systems based on numerous field observations of fracture-hosted hydrate in fine-grained sediments. These fractures are part of the failure process and may be important flow pathways for methane. These fracture models are the focus of one manuscript that has been accepted (Daigle and Dugan, accepted). Full-scale stability and slope failure models will incorporate our fracture work but will not be completed until 2010. We are now focusing on 2D models for failure and will submit at least two manuscripts in the upcoming phase of the project: one will be discussion on the general conditions for failure; the second will be assessment of observed failures at Cascadia in collaboration with researchers at the Pacific Geoscience Centre and the University of Victoria.

Subtask 8.1: Sediment-Hydrate Properties

This task has been completed with a digital database submitted to NETL and a paper published in Reviews of Geophysics (Waite et al., 2009).

Subtask 8.2: Modeling (In)stability

Modeling (in)stability in hydrate systems has resulted in three key advancements in our geological, hydrate accumulation models: (1) we have developed a fracture genesis model to explain localized failures; (2) we have incorporated salt production from hydrate formation which helps to explain some fracturing phenomena as well as free gas within the regional hydrate stability zone; and (3) we continue to explore 2D geometries that may lead to regional slope failures based on hydrate occurrence, fluid overpressure, and accumulation of free gas beneath the hydrate stability zone. This work has helped explain fracture distribution at the base of the hydrate stability zone, fracture distribution isolated within the stability zone, free gas flow through the stability zone, enhanced hydrate accumulations in permeable zones relative to low permeability confining units, and is at the cusp of isolating the pressure response of hydrates related to regional slope failures. Regional slope failures will be the focus of our work through the end of the DOE-funded research as we explore generalized slope failures to understand the mechanics and two known slope failures offshore Cascadia that may be related to gas hydrate.

The motivation to understand fractures as an instability in hydrate systems has been motivated by numerous field observations, including Hydrate Ridge, Keathley Canyon Block 151, and the Krishna-Godavari Basin offshore India. The goal was to determine how hydrate formation can cause fractures by pore pressure buildup or by frost heave (Daigle and Dugan, accepted).

Fracture Models

We simulate a one-dimensional system where methane-saturated water flows upwards. We prescribe a seafloor depth, seafloor temperature, geothermal gradient, porosity-depth profile, permeability-depth profile, and vertical fluid flow rate. Formation of methane hydrate is simulated by determining methane solubility for the given temperature and pressure conditions, and then performing a mass balance for water and methane. The methane solubility curve is computed using the methodology of Bhatnagar et al. (2007) assuming a constant NaCl concentration of 33.5%. We determine the hydrate saturation S_h by solving the mass balance for methane.

As hydrate forms, the pore space available to fluid flow is occluded based on the permeability of a series of cylindrical capillary tubes with hydrate forming a uniform coating on the walls (Nimblett and Ruppel, 2003), which is supported by the work of Yun et al. (2005) and Lee et al. (2007). The pore fluid pressure is computed from Darcy's Law. We maintain a constant flux as hydrate forms and permeability evolves.

We consider fracture formation by hydraulic fracturing driven by water pressure, and hydrate-induced heave. In a passive sedimentary basin, the maximum principal stress at a given depth is vertical and can be defined by integrating the bulk density. We assume that the total vertical stress is equal to the maximum principal stress, and that the horizontal stress is equal to the minimum principal stress. Hydraulic fractures form when the pore fluid pressure exceeds the horizontal effective stress. We define the overpressure ratio λ as the ratio of excess pore pressure to vertical effective stress under hydrostatic conditions. During normal, K_0 consolidation, the horizontal effective stress under hydrostatic conditions is typically 60% of the vertical hydrostatic effective stress (Karig and Hou, 1992); for fractures to occur, the excess pore pressure P^* must exceed the horizontal effective stress - fracturing to occurs where $\lambda \geq 0.6$.

Hydrate-induced heave is a process similar to frost heave where the formation of lenses of hydrate forces sediment grains apart (Krause, 2000). During growth of a hydrate lens, the solid hydrate will occupy pore space along with some fluid. The force which the hydrate lens exerts on the surrounding sediment is proportional to the volume of hydrate which can be formed from the remaining liquid volume; this concept is known as thermomolecular buoyancy and is analogous to Archimedes' Principle (Rempel, 2007). The net outward force per unit area \vec{F} which is exerted over the surface of the lens is given by (Rempel et al., 2004; Rempel, 2007). The dimensionless variable $H^* = \vec{F}/\sigma_v$ represents the positive ratio of heave force to vertical effective stress. Vertical hydrate-filled fractures are thus possible when $H^* \geq 0.6$, and horizontal hydrate-filled fractures are possible when $H^* \geq 1$.

We simulated hydrate formation at four field sites: Keathley Canyon Block 151 (KC151), Blake Ridge (Site 997), Hydrate Ridge (Site 1250), and NGHP Site 10 in the Krishna-Godavari Basin offshore India. At each site we simulated a homogeneous (reference) case, with single trends of porosity and permeability with depth, and a heterogeneous case, where porosity and permeability were varied based on lithology determined from petrophysical logs. We assumed

vertical flow rates of 0.4 mm yr⁻¹ at KC151, 0.2 mm yr⁻¹ at Blake Ridge, 300 mm yr⁻¹ at Hydrate Ridge, and 35 mm yr⁻¹ at NGHP Site 10. In the homogeneous cases, we found that fractures formed after 9x10⁵ years at KC151, 8x10⁶ years at Blake Ridge, 9000 years at Hydrate Ridge, and 10⁵ years at NGHP Site 10. Fractures in all cases form first near the base of the MHSZ, where the dissolved methane concentrations are highest and initial λ^* values are largest (Figure 1). Hydrate heave is a viable fracturing mechanism over all but the lowermost few tens of meters at each site. In the heterogeneous cases, we found that fractures formed after 3x10⁵ years at KC151, 8x10⁶ years at Blake Ridge, 1600 years at Hydrate Ridge, and 10⁵ years at NGHP Site 10. At KC151 and Blake Ridge, the location of fracture initiation was not changed from the homogeneous cases; at Hydrate Ridge and NGHP Site 10, fractures initiated at the base of some of the lower-permeability layers in the sequence (Figure 2).

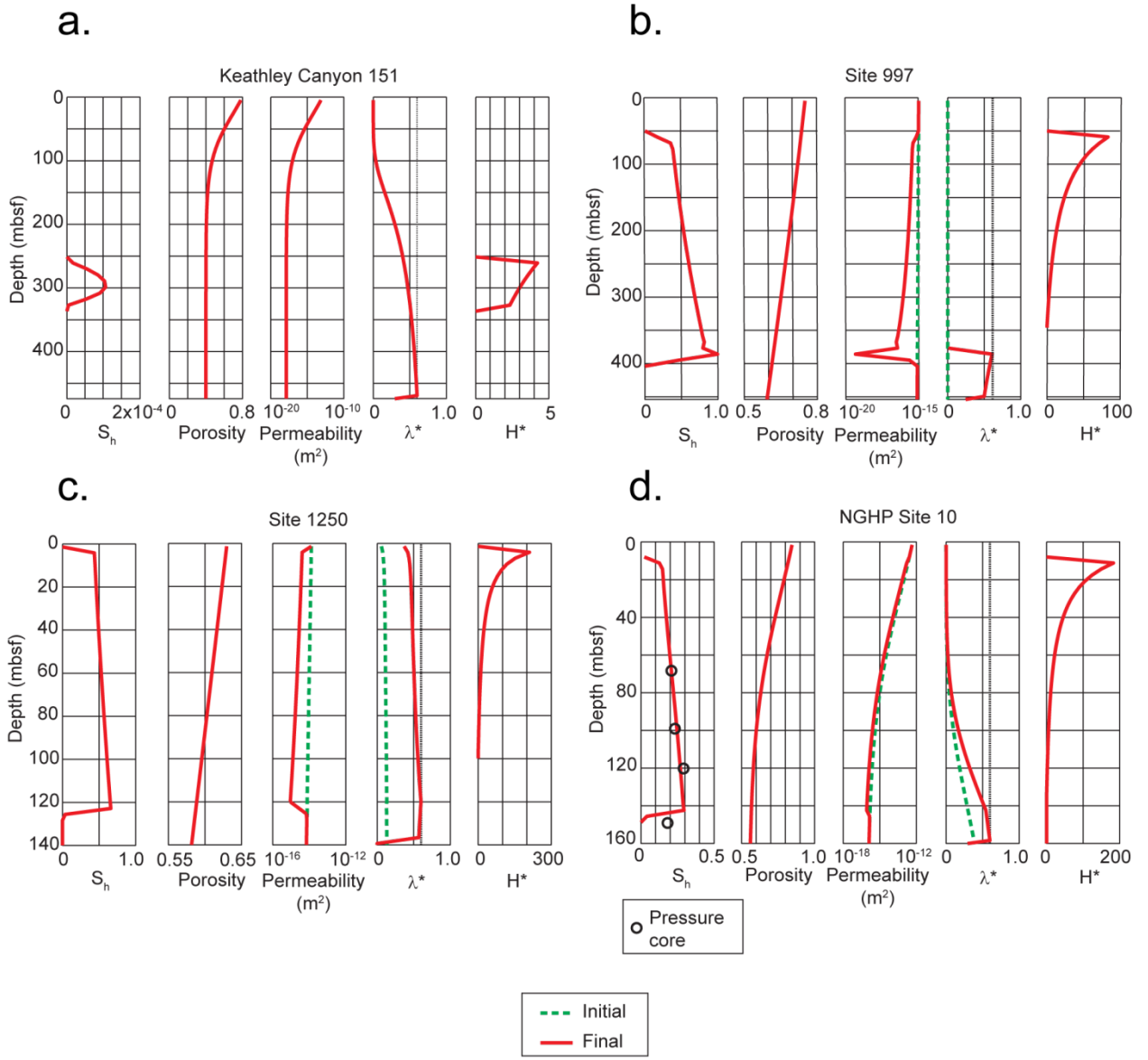


Figure 1. (a) Hydrate saturation, porosity, permeability, overpressure ratio λ^* , and ratio of hydrate heave force to vertical effective stress H^* results for KC151. The fracture criterion is $\lambda^* = 0.6$. The hydraulic fracturing criterion is achieved after 9×10^5 years at the base of the MHSZ. The hydrate heave force is sufficient to produce subvertical veins and fractures in the interval 250-340 mbsf. (b) Model results for Blake Ridge. The fracture criterion is achieved after 8×10^6 years near 390 mbsf where $S_h = 0.99$. The hydrate heave force is sufficient to produce subvertical veins and fractures in the interval 50-310 mbsf. (c) Model results for Hydrate Ridge. The fracture criterion is achieved after 9×10^3 years near 122 mbsf. The hydrate heave force is sufficient to produce subvertical veins and fractures above 90 mbsf. (d) Model results for NGHP Site 10. Pressure core data are from Lee and Collett (2009). The hydraulic fracturing criterion is achieved after 10^5 years. The hydrate heave force is sufficient to produce subvertical veins and fractures in the interval 10-135 mbsf. Note how the computed S_h profile closely matches the pressure core saturations; we use this match as a constraint on vertical flow rates.

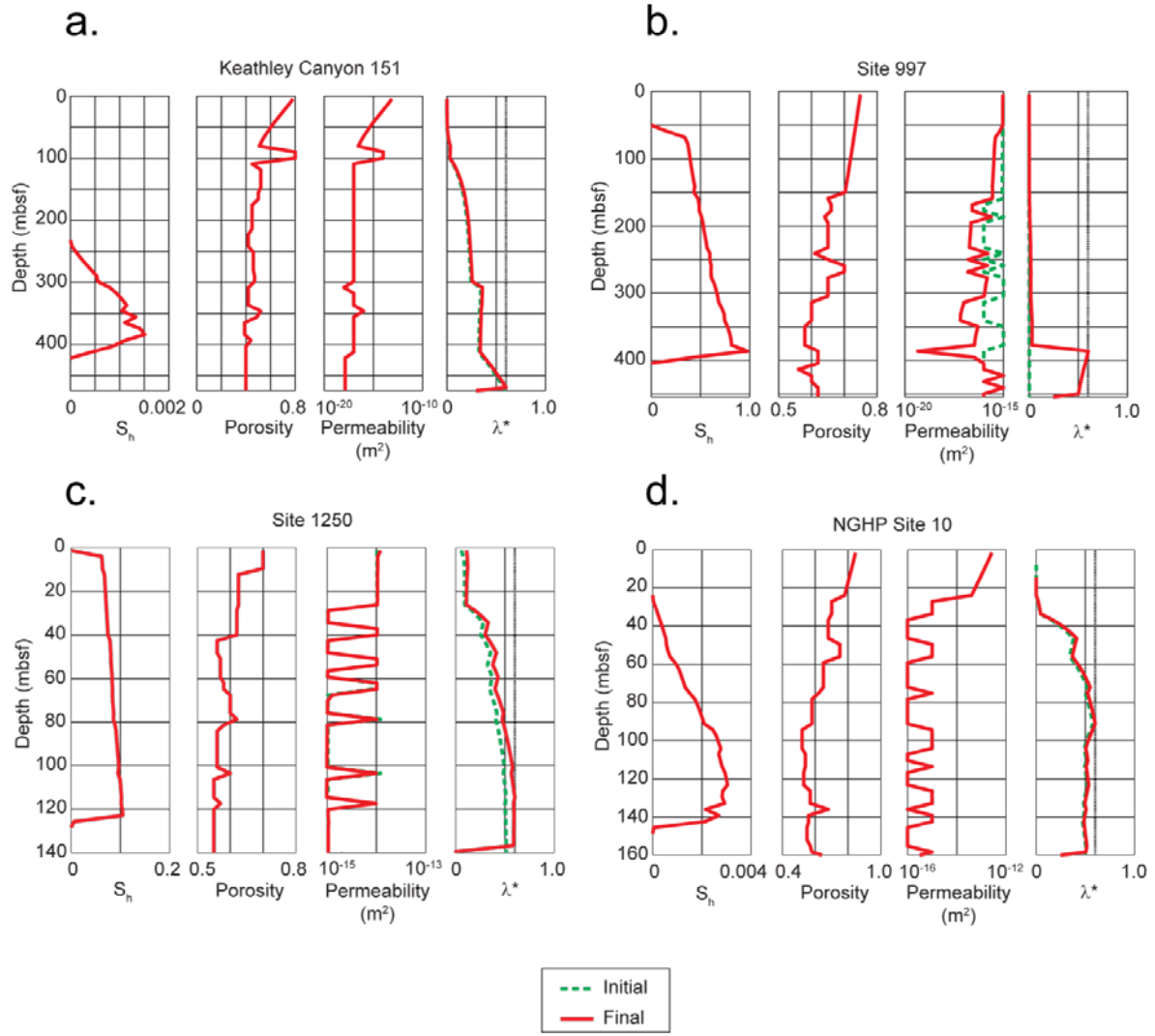


Figure 2. (a) Hydrate saturation, porosity, permeability and overpressure ratio results for KC151 with heterogeneities derived from the log data. The fracture criterion was achieved after 3×10^5 years at the base of the MHSZ. (b) Results for Blake Ridge with heterogeneities derived from the log data. Fracture criterion was achieved after 8×10^6 years at 386 mbsf, which is the same as predicted for the homogeneous case (Figure 1b). (c) Results for Hydrate Ridge with heterogeneities derived from the log data. Fracture criterion was achieved after 1600 years at the base of the MHSZ and at the base of a low-permeability layer near 115 mbsf illustrating how low-permeability layers can cause fracturing throughout the MHSZ. (d) Results for NGHP Site 10 with lithologic heterogeneities derived from the log data. The fracture criterion is achieved after 6×10^3 years at the base of a clay layer at 87 mbsf.

Fractures tend to initiate first in locations which have high initial λ^* values. Initial λ^* values are determined by permeability and fluid flux, and will be higher in areas with low permeability and/or high flux. In the case of KC151 and Blake Ridge, the fluid fluxes are so low that lithologic heterogeneities are not sufficient to cause fractures to nucleate in locations other than the base of the MHSZ.

Hydrate Ridge and NGHP Site 10 represent the other end-member, where the combination of high fluxes and low-permeability layers is sufficient to cause fracture initiation in the low-permeability layers. Hydrate heave is more likely to be a significant fracturing mechanism at low-flux sites like KC151 or Blake Ridge.

Free Gas in the MHSZ and Fractures

We are now extending this work by investigating the effect of free gas within the MHSZ on fluid pressures. To accomplish this, we have developed a model, which couples a chloride mass balance relation with hydrate and free gas stability conditions. As hydrate forms, salts are excluded from the water, which is incorporated into the hydrate crystals. This has the effect of increasing the salinity in the remaining pore fluid (Liu and Flemings, 2006). The increased salinity in the pore fluid causes a depression of the liquid+hydrate+free gas triple point (Sloan, 1990), and it is possible to increase salinity within the MHSZ to the point where free gas is stable along with dissolved methane and hydrate.

We solve the mass balance equation for methane dissolved in pore fluid and methane in free gas. We assume a constant pressure at the base of the domain rather than a constant flux as before. Fluxes are computed from Darcy's law. Gas viscosity is calculated from the Lennard-Jones potential (Bird et al., 2007). Relative permeabilities are calculated using Corey's model (Bear, 1972). The difference between the gas phase pressure and the water pressure is the capillary pressure, which we compute using a J-function (Bear, 1972) based on mercury injection capillary pressure measurements on a marine mudstone.

Our initial simulations show two striking results: (1) water flux is crucial to the location of fractures within the MHSZ and the ability of free gas to migrate into the MHSZ and (2) gas accumulation in the MHSZ affects the gas hydrate saturation profile in the MHSZ (Figure 3).

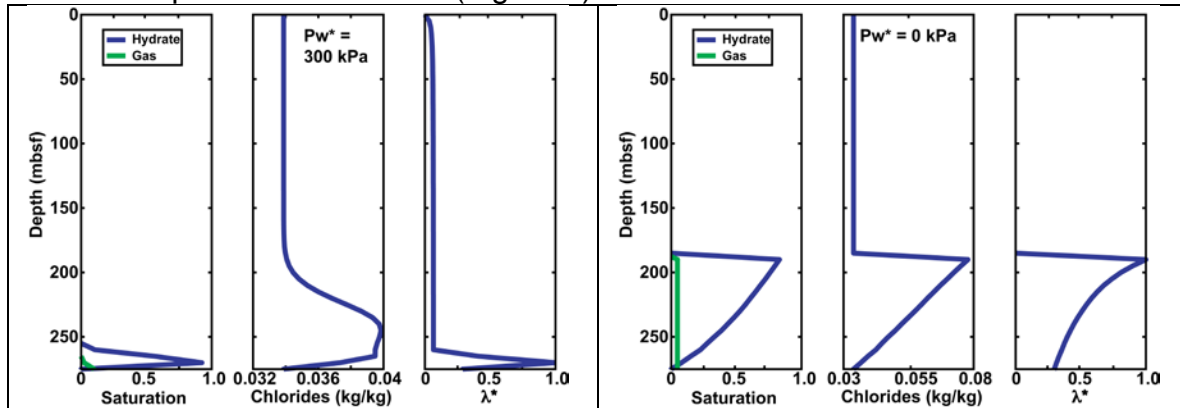


Figure 3. Model results for free gas in the MHSZ with homogeneous lithology but varying water fluxes. (Left) Basal water overpressure of 300 kPa drives water flux vertically upward flushing away salt formed during hydrate formation yielding high hydrate saturation and fractures at the base of the MHSZ (275 mbsf). (Right) No water flux ($P^* = 0$ kPa) to flush salts away so free gas migrates into the MHSZ, hydrate saturation increases with decreasing depth, and fractures are formed at the top of the hydrate and free gas.

These results suggest that the background water flux is a dominant control on the hydrate saturation and distribution and the ability for free gas to pass through the regional MHSZ. In essences when water flux is high (Figure 3, left), the water can flush away produced salts so the triple point does not change, and free gas will not migrate into the MHSZ. When water flux is low (Figure 3, right), salts resulting from hydrate precipitation remain in the regional MHSZ allowing gas to migrate upward and increasing the hydrate saturation with decreasing depth. Fractures then occur within the MHSZ where hydrate saturation is highest.

We are now exploring gas within the MHSZ with our model and comparing it to filed observations. Preliminary results for Hydrate Ridge indicate that free gas does not significantly alter the time required to achieve the fracture criterion, and that lithologic heterogeneities have the same effect as before, namely reducing the time to fracture and causing fractures to nucleate in low-permeability layers. We ran simulations to reach a fracture criterion where the gas phase pressure equals the vertical effective stress; in the homogeneous case, the simulation took 6018 years (Figure 4) and 2262 years in the heterogeneous case (Figure 5). These fast results suggest that steady-state flows may be valid at Hydrate Ridge for short time periods. The predicted chloride profiles and hydrate saturation profiles (Figure 4) are qualitatively similar to those observed at Hydrate Ridge and we are continuing to explore how well we can predict the timing of hydrate accumulations at Hydrate Ridge.

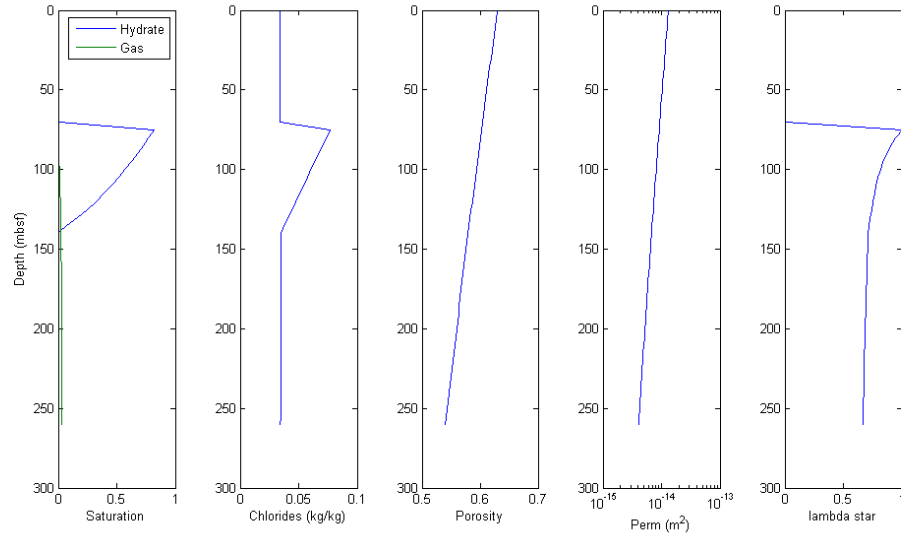


Figure 4. Model results for Hydrate Ridge with free gas in the MHSZ with homogeneous lithology. Simulation took 6018 years to achieve the fracture criterion. Left to right, saturations, chloride mass fraction, porosity, permeability, and λ^* . Fractures nucleate near 70 mbsf where the hydrate saturation is near 80%.

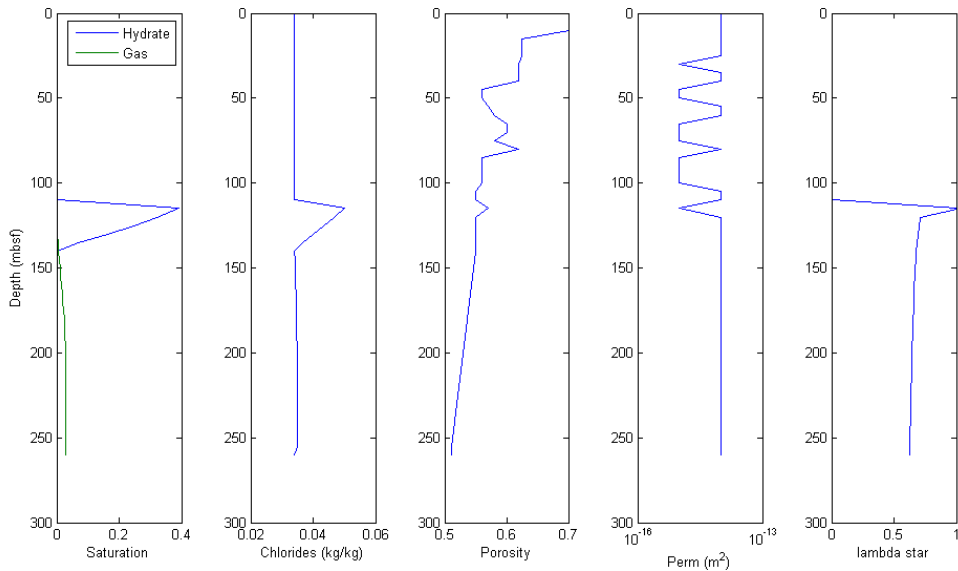


Figure 5. Model results for Hydrate Ridge with free gas in the MHSZ and heterogeneous lithology. Simulation took 2262 years to achieve the fracture criterion. Hydrate saturation at fracture is less than in Figure 3, and fracture initiate in the low-permeability layer near 120 mbsf.

Heterogeneity and Hydrate Accumulation

These models have also allowed us to study preferential hydrate accumulation in higher-permeability layers. Observations from Hydrate Ridge (Su et al., 2006; Weinberger & Brown, 2006) and the northern Cascadia margin (Malinverno et al., 2008; Torres et al., 2008) indicate that hydrates in these areas are located preferentially in layers with larger grains and higher permeability. Recent experimental data suggest that the triple point is depressed in sediments with small pore throats because of capillary effects (Henry et al., 1999; Uchida et al., 2004; Torres et al., 2008). This has the effect of increasing the solubility of methane in these sediments, so that higher concentrations of dissolved methane are required to form methane in lower-permeability layers than in higher-permeability layers. Malinverno (2010) modeled hydrate formation in an interbedded silt-clay sequence from methane produced in situ by biogenic processes, and found that the higher solubility in the clay layers produced a relative oversaturation in these layers relative to the silts, resulting in a diffusive flux of methane from the clays to the silts. This diffusive flux was found to be sufficient to produce the observed hydrate distributions from IODP311 Site U1325. However, this location is interpreted to be an advective methane system based on porewater chlorinity observations (Riedel et al., 2006). We are interested in determining if similar hydrate saturation profiles can be obtained by advective transport of methane.

Our preliminary modeling results indicate that advective methane transport can result in preferential hydrate formation in silts relative to clay because of the higher solubility of methane in the clays. We modeled flow through a 50 m-thick domain of alternating 10 m-thick layers of silt and clay. Temperature, pressure,

permeability, and porosity conditions were based on Hydrate Ridge Site 1250; we assumed permeabilities of 10^{-15} m^2 in the clays and 10^{-14} m^2 in the silts. Solubility was computed by increasing the triple point temperature T_{3P} by an increment $\Delta T_{3P} = (0.0016 - 0.23/d)T_{3P}$, where d is the pore diameter in nanometers (Uchida et al., 2004; Torres et al., 2008). Hydrate forms near the tops of the clay layers and throughout the silt layers; fractures propagate upwards through the clay layers but not in the silt layers. After ~60,000 years of simulation time, fractures propagate through the lower two clay layers, bypassing the intervening silt layer (Figure 6). We plan to model the turbidite sequence encountered in IODP 311 and modeled by Malinverno (2010) once we find suitable permeability and fluid flow constraints.

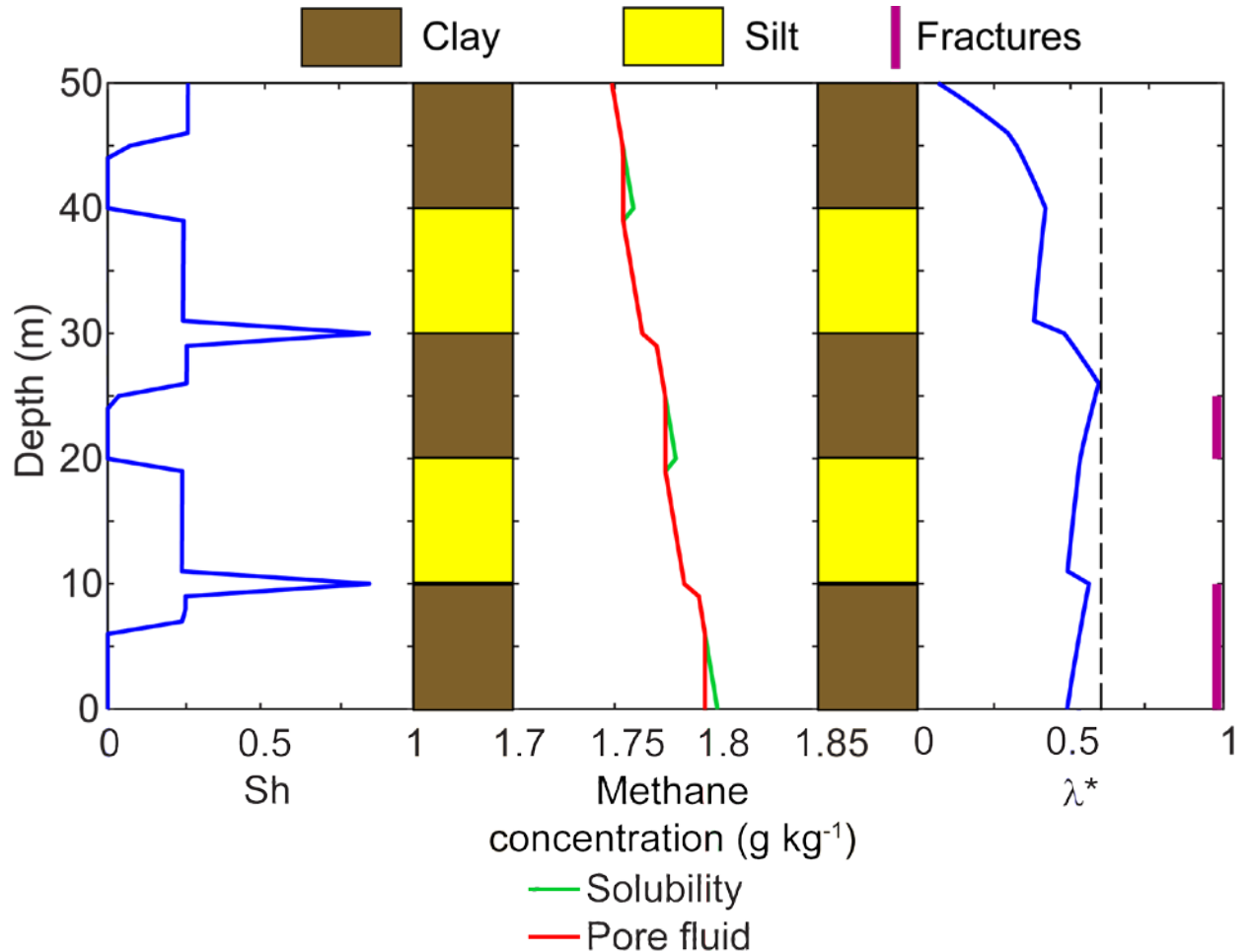


Figure 6. Model results for flow through interbedded silts and clays with capillary effects on solubility. Left to right, hydrate saturation, solubility and concentration of methane in pore fluid, overpressure ratio. Lithology column is indicated between tracks in yellow and brown. Fractures shown on the far right as purple bars. After 60,000 years, fractures have propagated upwards through the lowermost clay and partway through the next clay, but have bypassed the intervening silt. Hydrate forms preferentially in the silts and near the top of the clay layers.

Beyond 1D models, we have also been exploring 2D models to look at stability and gas hydrate accumulations. We are moving forward on this front at two levels: heterogeneity and stability. Heterogeneity has shown that permeable conduits increase the ability to capture methane thus increasing hydrate saturation (Figure 7). Simply, the larger the permeability contrast, the more likely hydrate and gas are to accumulate in the more permeable conduits. This may help explain saturations in high flux conduits like pipes, vents, and dipping reservoirs in advective systems. We will continue to test these models as we continue to establish contacts with colleagues working on related field programs.

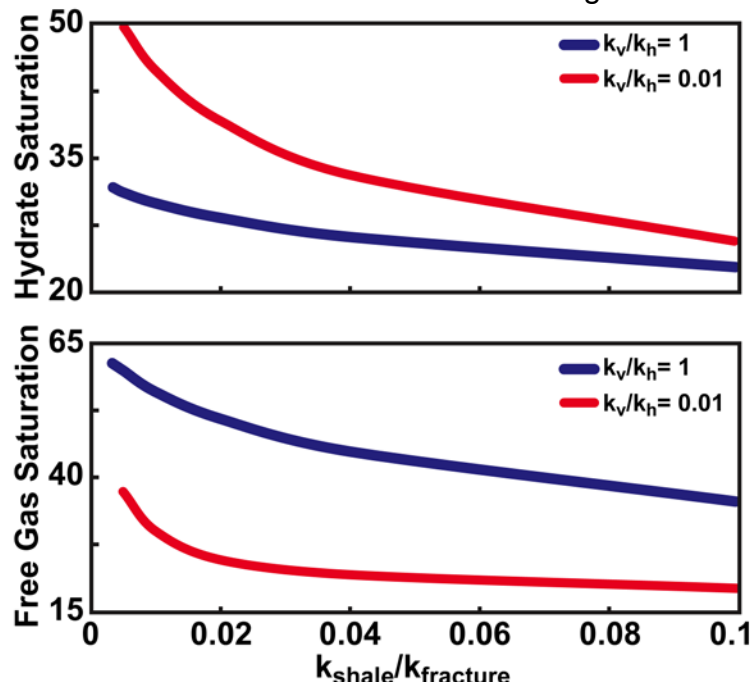


Figure 7. Model results showing the importance of permeability contrasts and permeability anisotropy on the accumulation and saturation of methane hydrate and free gas saturations. As permeability contrast between a shale and fracture (or sand) becomes smaller ($k_{\text{shale}} \ll k_{\text{fracture}}$ or $k_{\text{shale}} \gg k_{\text{fracture}}$) the hydrate and free gas saturations in the permeable unit increases. As anisotropy decreases (k_v/k_h) in the shale, the saturations also increase.

Last, we continue to explore hydrate-related slope failures. We have functional 1D and 2D stability models that have been benchmarked. We have run sensitivity studies but have yet to find any geologically reasonable hydrate systems that drive or control slope failure. We are now extending these models to look at the role gas may play in failures. The leading ideas are as free gas accumulates, effective stress decreases and drives slope failure at the base of the MHSZ. The second idea is gas pressures increase during dissociation which will drive failure at sensitive regions (e.g. updip limit) of the MHSZ. These failures will be one of the primary focuses in the upcoming phase of research.

Subtask 8.3: Integrating geomechanical studies

This task has been coupled with Subtask 8.2 as we use geomechanical field data to test our stability and fracture models. Based on recent results presented at the

Gordon Research Conference on Natural Gas Hydrate Systems, we have learned of new strength measurements and models for hydrate saturated sandstones. This work will be incorporated into our stability models as their results become publically available. In addition we are working with other lab groups to obtain capillary entry pressure data for fine- and coarse-grained systems that we can include in our models. These properties affect fracture genesis, gas distribution, and hydrate saturations; these data, however, are limited.

Presentations

- Daigle, H., Dugan, B., 2009, Fracture genesis in methane hydrate systems, Rice University Department of Earth Science seminar, Houston, TX (17 November 2009).
- Daigle, H., Dugan, B., 2009, Fracture genesis and fracture filling in methane hydrate systems, American Geophysical Union Fall Meeting, San Francisco, CA (17 December 2009).
- Daigle, H., 2009, Fracture genesis and fracture filling in methane hydrate systems, DOE/NETL Methane Hydrate Workshop, Atlanta, GA (26 January 2010).
- Daigle, H., Dugan, B., 2010, Origins of fracture-hosted methane hydrates, Chevron technology talk, Houston, TX (11 March 2010).
- Daigle, H., 2010, Lithologically partitioned hydrates in advective systems, Gordon Research Conference: Natural Gas Hydrate Systems, Waterville, ME (6-11 June 2010).
- Dugan, B., 2010, Physical properties studies: flow, fractures, and failures, DOE/NETL Methane Hydrate Workshop, Atlanta, GA (26 January 2010).
- Dugan, B., 2010, Continuum Models of Large-Scale Phenomena Associated with Hydrate-Bearing Sediments, Gordon Research Conference: Natural Gas Hydrate Systems, Waterville, ME (6-11 June 2010).

Publications

- Daigle, H., Dugan, B., accepted pending revision, Origin and evolution of fracture-hosted methane hydrate deposits, *Journal of Geophysical Research*.
- Waite, W.F, C. Santamarina, D. Cortes, B. Dugan, N. Espinoza, J. Germaine, J. Jang, J. Jung, T. Kneafsey, H. Shin, K. Soga, W. Winters, T-S. Yun, accepted pending revision, Physical properties of hydrate-bearing sediments, *Reviews of Geophysics*, 47, RG4003, doi:10.1029/2008RG000279.

Hydrate Collaborations and Community Service

Dugan was a member of the panel discussion on Gas Hydrates and Slope Stability at the Submarine Mass Movements and Their Consequences Symposium, Austin, TX, November 7-12, 2009.

Dugan has opened hydrate-related collaborations with M. Riedel (Pacific Geoscience Center, British Columbia, Canada) and N. Scholz (University of Victoria, British Columbia, Canada) to model the hydrate formation and slope failure along the Cascadia margin and with Xiujuan Wang (Institute of Oceanology, Chinese Academy of Sciences) to study flow systems related to heterogeneous hydrate accumulations in the South China Sea and to compare them with the Gulf of Mexico.

Dugan has also been collaborating with the Chevron Gulf of Mexico JIP team to develop the science plan for Leg III in 2011. Dugan is leading the physical properties science plan initiative that will be integrated with the overall science plan to meet the objectives of the JIP in 2011.

References

- Bear, J. (1972), *Dynamics of Fluids in Porous Media*, 784 pp, Dover, Mineola, New York.
- Bhatnagar, G., Chapman, W.G., Dickens, G.R., Dugan, B., and G.J. Hirasaki (2007), Generalization of gas hydrate distribution and saturation in marine sediments by scaling of thermodynamic and transport processes, *Am. J. Sci.*, 307, 861-900, doi:10.2475/06.2007.01.
- Bird, R.B., Stewart, W.E., Lightfoot, E.N. (2007), *Transport Phenomena* (2nd Ed.), 905 pp, John Wiley & Sons, New York.
- Daigle, H., and B. Dugan (2009), Extending NMR data for permeability estimation in fine-grained sediments, *Mar. Petrol. Geol.*, 26(8), 1419-1427, doi:10.1016/j.marpetgeo.2009.02.008.
- Henry, P., Thomas, M., and M.B. Clennell (1999), Formation of natural gas hydrates in marine sediments 2. Thermodynamic calculations of stability conditions in porous sediments, *J. Geophys. Res.*, 104(B10), 23005-23022.
- Karig, D.E., and G. Hou (1992), High-stress consolidation experiments and their geologic implications, *J. Geophys. Res.*, 97(B1), 289-300.
- Krause, F.F. (2000), Genesis and geometry of the Meiklejohn Peak lime mud-mound, Bare Mountain Quadrangle, Nevada, USA: Ordovician limestone with submarine frost heave structures – a possible response to gas clathrate hydrate evolution, *Sed. Geol.*, 145, 189-213.

- Lee, J.Y., Yun, T.S., Santamarina, J.C., and C. Ruppel (2007), Observations related to tetrahydrofuran and methane hydrates for laboratory studies of hydrate-bearing sediments, *Geochem. Geophys. Geosyst.*, 8(6), Q06003, doi:10.1029/2006GC001531.
- Lee., M.W., and T.S. Collett (2009), Gas hydrate saturations estimated from fractured reservoir at Site NGHP-01-10, Krishna-Godavari Basin, India, *J. Geophys. Res.*, 114, B07102, doi:10.1029/2008JB006237.
- Liu, X., Flemings, P.B., 2006. Passing gas through the hydrate stability zone at southern Hydrate Ridge, offshore Oregon. *Earth Planet. Sci. Lett.*, 241, 211-226, doi:10.1016/j.epsl.2005.10.026.
- Malinverno, A. (2010), Marine gas hydrates in thin sand layers that soak up microbial methane, *Earth Planet. Sci. Lett.*, 292, 399-408, doi:10.1016/j.epsl.2010.02.008.
- Malinverno, A., Kastner, M., Torres, M.E., Wortmann, U.G. (2008), Gas hydrate occurrence from pore water chlorinity and downhole logs in a transect across the northern Cascadia margin (Integrated Ocean Drilling Program Expedition 311), *J. Geophys. Res.*, 113, B08103, doi:10.1029/2008JB005702.
- Nimblett, J., and C. Ruppel (2003), Permeability evolution during the formation of gas hydrates in marine sediments, *J. Geophys. Res.*, 108(B9), doi:10.1029/2001JB001650.
- Rempel, A.W. (2007), Formation of ice lenses and frost heave, *J. Geophys. Res.*, 112, F02S21, doi:10.1029/2006JF000525.
- Rempel, A.W., Wettlaufer, J.S., and M.G. Worster (2004), Premelting dynamics in a continuum model of frost heave, *J. Fluid Mech.*, 498, 227-244, doi:10.1017/S0022112003006761.
- Riedel, M., Collett, T.S., Malone, M.J., Expedition 311 Scientists (2006), *Proc. IODP*, 311, Integrated Ocean Drilling Program, Washington, DC, doi:10.2204/iodp.proc.311.2006.
- Sloan, E.D. Jr. (1990), *Clathrate Hydrates of Natural Gases*, 641 pp., M. Dekker, New York.

- Su, X., Song, C.-B., Fang, N.-Q. (2006), Relationship between sediment granulometry and the presence of gas hydrate on Hydrate Ridge, edited by A.M. Tréhu et al., *Proc. Ocean Drill. Program Sci. Results*, 204, 1-30, doi:10.2973/odp.proc.sr.204.115.2006.
- Tan, B., Germaine, J.T., and P.B. Flemings (2006), Data report: Consolidation and strength characteristics of sediments from ODP Site 1244, Hydrate Ridge, Cascadia continental margin, edited by A.M. Tréhu et al., *Proc. Ocean Drill. Program Sci. Results*, 204, 1-148, doi:10.2973/odp.proc.sr.204.102.2006.
- Torres, M.E., Tréhu, A.M., Cespedes, N., Kastner, M., Wortmann, U.G., Kim, J.-H., Long, P., Malinverno, A., Pohlman, J.W., Riedel, M., Collett, T. (2008), Methane hydrate formation in turbidite sediments of northern Cascadia, IODP Expedition 311, *Earth Planet. Sci. Lett.*, 271, 170-180, doi:10.1016/j.epsl.2008.03.061.
- Uchida, T., Nagao, J., Yakushev, V.S., Istomin, V.A., Minagawa, H., Ebinuma, T., Narita, H., Takeya, S., Chuvalin, E.M., Ohmura, R. (2004), Decomposition of methane hydrates in sand, sandstone, clays and glass beads, *J. Geophys. Res.*, 109, B05206, doi:10.1029/2003JB002771.
- Waite, W.F., C. Santamarina, D. Cortes, B. Dugan, N. Espinoza, J. Germaine, J. Jang, J. Jung, T. Kneafsey, H. Shin, K. Soga, W. Winters, T-S. Yun, 2009, Physical properties of hydrate-bearing sediments, *Reviews of Geophysics*, 47, RG4003, doi:10.1029/2008RG000279.
- Weinberger, J.L., Brown, K.M. (2006), Fracture networks and hydrate distribution at Hydrate Ridge, Oregon, *Earth Planet. Sci. Lett.*, 245, 123-136, doi:10.1016/j.epsl.2006.03.012.
- Winters, W.J., B. Dugan, T.S. Collett, 2008, Physical Properties of Sediments from Keathley Canyon and Atwater Valley, JIP Gulf of Mexico Gas Hydrate Drilling Program, *Marine and Petroleum Geology*, 25, 896-905, doi:10.1016/j.marpetgeo.2008.01.018.
- Yun, T.S., Francisca, F.M., Santamarina, J.C., and C. Ruppel (2005), Compressional and shear wave velocities in uncemented sediment

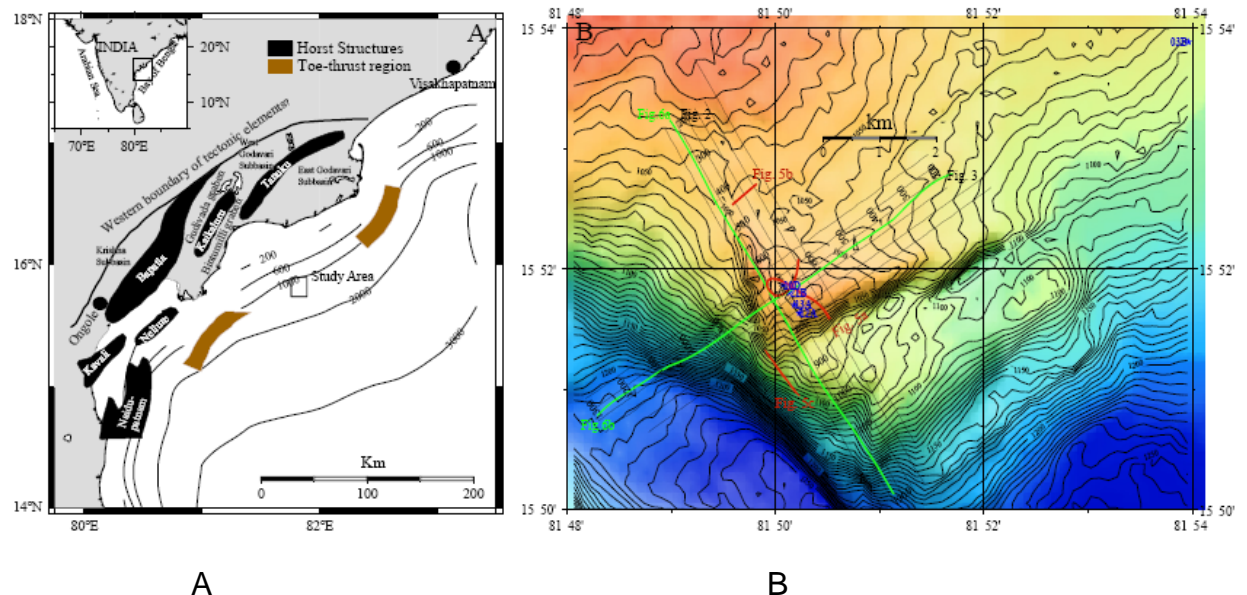
containing gas hydrate, *Geophys. Res. Lett.*, 32, L10609,
doi:10.1029/2005GL022607.

Task 9: Geophysical Imaging of Gas Hydrate and Free Gas Accumulations

P. Jaiswal and C.A. Zelt

1. The seismic data that is being used for Task 9 comes from Krishna-Godavari (K-G) Basin in the Indian east coast. The well data were collected during the NGHP drilling expedition in 2005. The PI is successfully collaborating with National Institute of Oceanography (NIO), India.
2. In the previous budget period, subtask 9.1: Preliminary processing and traveltime inversion of the data were accomplished. A pre-stack depth migrated image was generated using velocity model from composite inversion/migration that agreed very well with the sonic log suggesting that the velocity model and the depth image were geologically accurate.
3. In the current budget period, subtask 9.2: 2-D acoustic waveform inversion is being performed. However, due to a delay of 6 months in setup of computational facilities at Oklahoma State University, this task could not meet its deadline. Results are anticipated by December 2010.
4. We are at the initial stages of waveform inversion currently. So far we have performed numerous tests with synthetic data to ensure that the data have adequate frequency bandwidth to resolve features of interest, mainly the fractured stratigraphy at a length scale of ~100m.
5. In the current budget period while we were waiting on computation setup for waveform inversion, we looked at critical issues related to fluid flow using seismic data along with our colleagues in NIO. A paper titled "Fault controlled focused fluid flow in the vicinity of NGHP-01-10 site, Krishna-Godavari basin, Bay of Bengal" was prepared and submitted to Marine and Petroleum Geology.
6. Although, estimation of fluid flow using seismic data is not within the scope of subtask 9.2, it will serve as a critical input in the overall goal of this subtask - quantification and interpretation of the hydrates in the K-G basin.

Fluid flow estimates from seismic data



A

B

Figure 1. Study Area. A. KG basin is located offshore east coast of India. The horst and graben structures and the toe-thrusts have been interpreted after Rao (2001) and Bastia (2006). Study area with multibeam bathymetry is shown in B. Seismic lines used in this study are indicated in solid black lines; seismic lines in green are displayed in Figures 2a (NW-SE) and 2b (SW-NE). Stars denote location of NGHP-01-10/12/13/21 sites.

In passive continental margins such as K-G basin the formation and distribution of gas hydrates appears to be closely related with the fluid/gas flow into the base of hydrate stability zone (BHSZ) from deeper region that can perturb the geo-thermal gradient (Ruppel and Kinoshita, 2000). In passive settings, anomalous flow occurs in areas with rapid sedimentation and compaction that prevents the fluids to be expelled during sedimentation (Judd and Hovland, 2007) and leading to perturbations in BHSZ (Pecher et al., 2009). It is also a common practice to use BSR derived heat flow to understand the thermal profile along the continental margins (Ganguly et al., 2000). In this study, we estimate the geothermal gradient (GTG) from the seismic data to understand the thermal regime around NGHP-01-10 site. We identify zones of abnormal GTG and establish a relationship between abnormal GTG with the observed surface and subsurface structures.

Our understanding is that large (> 10 m throw) scale faulting near the NGHP-01-10 site enables a focused fluid flow which in turn controls the growth and accumulation of the gas hydrate within the faults themselves. We suspect that the fluid flow also perturbs (increases by 15-20%) the regional geo-thermal gradient ($38^{\circ}\text{C}/\text{km}$) and final concentration of hydrates is from interplay between the volume of the advecting fluid, their temperature and methane concentration, and permeability of the faults. Using a suite of geophysical data we show that that high concentration of hydrates could be limited to parts of the stratigraphy

that are close to the faults. It is possible that hydrate in the K-G basin in sites that have similar fault patterns as NGHP-01-10 are controlled by the faults and therefore have high spatial variability. Our findings have significant implication on the future of hydrate exploitation in the K-G basin.

Datasets used for fluid flow estimation comprise multi-channel seismic (MCS), high resolution sparker (HRS), Multi-beam bathymetry, and sub-bottom profiler (SBP). Fault pattern in the vicinity of the NGHP-10-01 is interpreted simultaneously on all datasets. Bottom-Simulating Reflector (BSR) is interpreted only in the MCS time and depth stacks. Increase in the interval velocity over a background velocity of 1.6 km/s is considered as a proxy for increase in hydrate concentration above the BSR. Similarly, decrease in interval velocity is considered as a proxy for free gas. Heat flow and GTG are calculated using the temperature at the seafloor and at the BSR from the NGHP-01-10 well core/logs.

Data

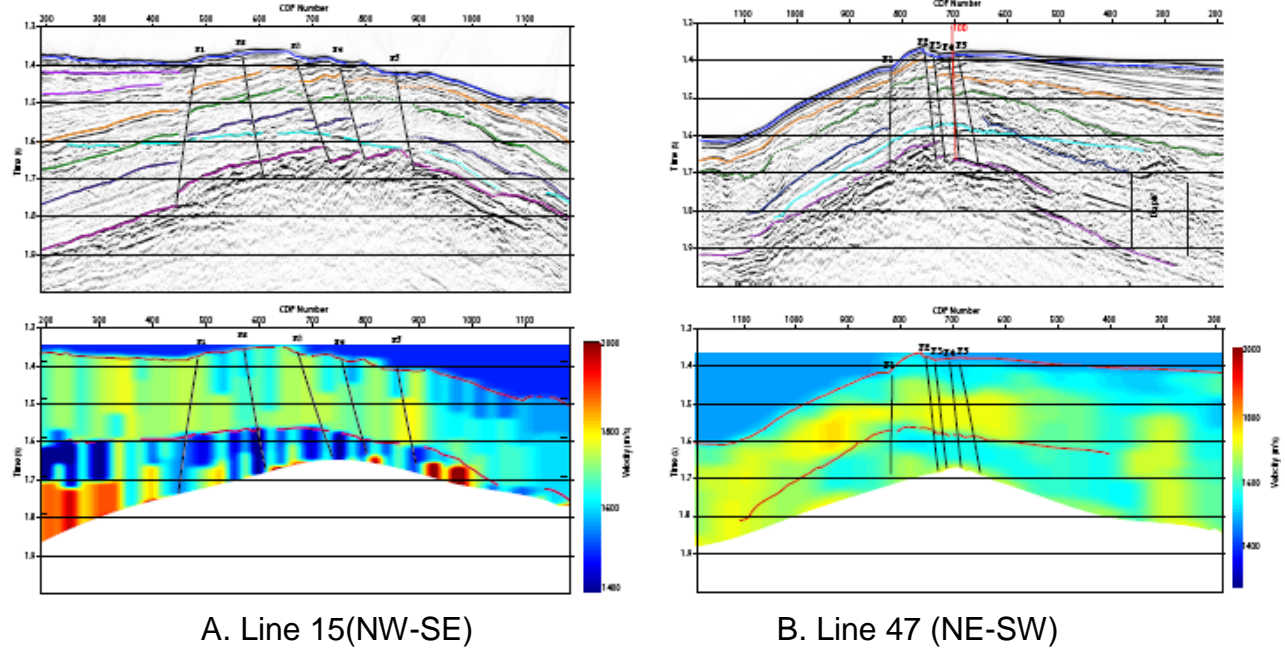


Figure 2. Multichannel Seismic. Top A and B: The interpreted section; light blue color represents BSR. Bottom A and B. The velocity model from the conventional semblance analysis method for stacking velocity estimation; blue is slower velocity and red is faster velocity. Water bottom and BSR are highlighted on the velocity model. A drop in interval velocity is observed below the BSR (free gas?) and several high velocity patches (hydrates?) are observed above the BSR.

About 100 km total length of MCS profiles (12 profiles ~8.5 km each covering the location of NGHP-10-01) were processed and interpreted. The main purpose of processing was to provide a quasi 3-D structural image. The processing sequence was simpler than the sequence adopted for inversion in Subtask 9.1. MCS processing follows standard methods emphasizing on deconvolution to

remove the source bubble effects and normal and dip move-out velocity analysis. Other modules include trace editing, filtering, stacking, and post-stack time migration sequentially. Typically in marine datasets, multiples are a serious concern. Fortunately, in our case, due to the depth of the seafloor (~1000 m), seismic coda of interest lies within the first multiple (~2.67 s). The time sections were scaled in depth using stacking velocity. The seafloor and BSRs were picked on both time and depth seismic profiles after analyzing inline and crossline misties. The picked horizons were interpolated into three-dimensional surfaces.

Multi-beam bathymetry data was used sea floor topography. These data were acquired onboard Sagar Kanya in 2002. Processing of these data was done using Multibeam System 4.6.10 (Caress and Chayes, 1996) has been used to process and grid the swath bathymetry data. The bathymetric mosaic shows the surface expression of major faults.

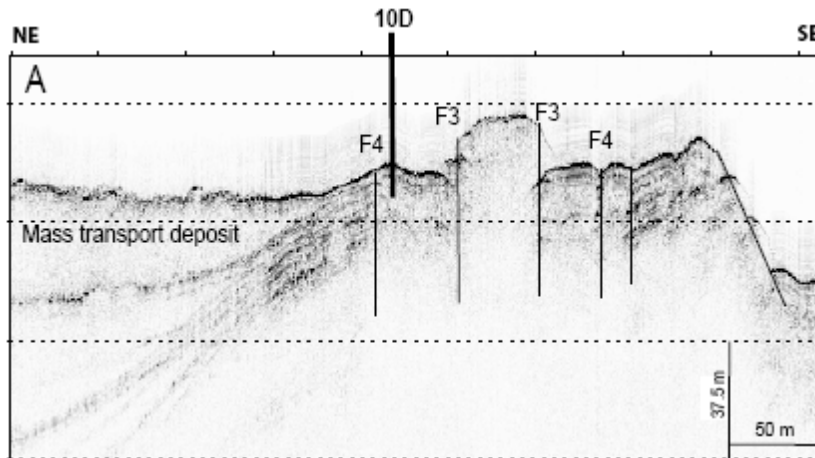


Figure 3. The SBP data close to the mound. The central portion of the mound is located close to site 10. The surface imprints of fault F3 and F4 have been interpreted. The SBP profile is coincident with Line 15 (Figure 2a).

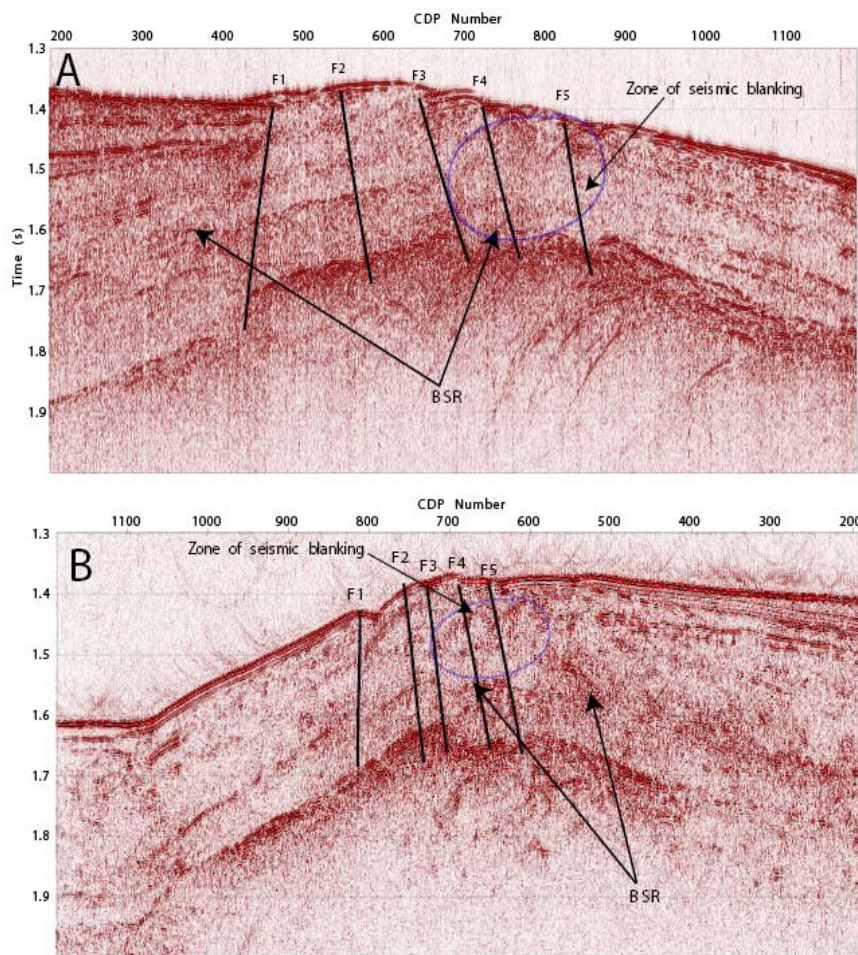


Figure 4. HRS profiles A)
Coincident with Line 15. B) Coincident with Line 47. The CDP number on HRS data represents the closest CDP number of MCS data. Faults observed in the MCS data (Fig. 2) have been interpreted in the HRS profiles. BSR is not observed in these data as strongly as MCS data.

The sea-bottom profile (SBP) data have been used to infer the shallow subsurface structure and faulting was acquired onboard Marion Dufresne in 2007 using Seafalcon 11 echo-sounder. One of the main features of this profiler was the use of a dedicated transmission array, large bandwidth signal and a large size multibeam reception array to create a high signal-to-noise ratio and a narrow beam width. SBP

High Resolution sparker (HRS) data was used to image shallow depths (< 100 m) below the seafloor in high resolution (~1.5 m scale). The data have a dominant frequency bandwidth of 150-1000 Hz and were acquired onboard Sagar Nidhi in 2009 using the 10KJ Geo-Resources Sparker system.

Geo-Thermal Gradient Computation

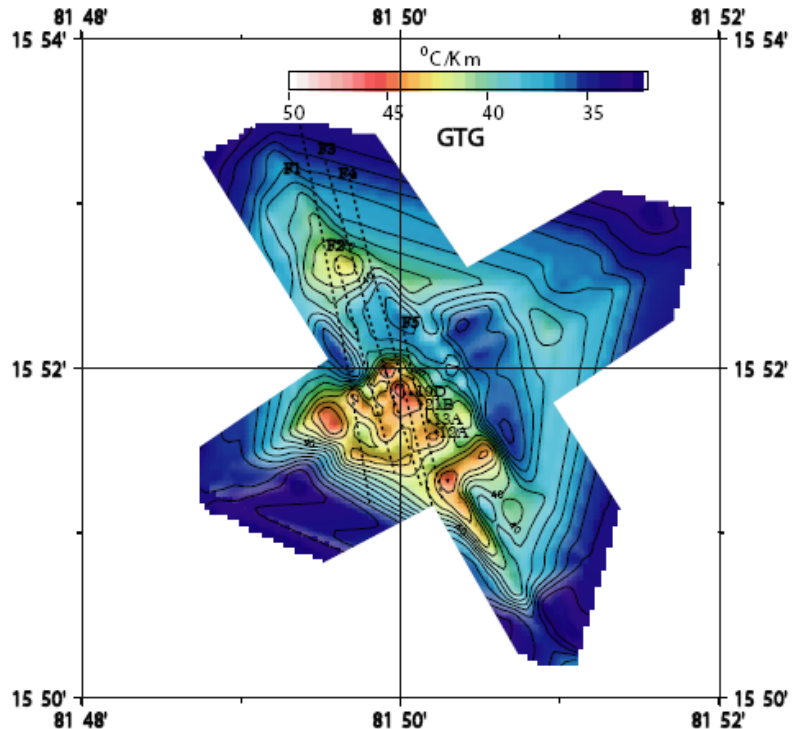


Figure 5. BSR derived GTG in the study area. The traces of fault system are shown in the plot. An abnormal increase in GTG is observed close to the fault system towards the mound.

BSR derived geothermal gradient was computed from the depth and temperature of the seafloor and BSR. The seafloor temperature was obtained by using the available Conductivity-Temperature-Depth (CTD) profiles in the study area. The phase curve of methane hydrate and sea water was obtained from the equation of Miles et al (1995). The temperature at the BSR depth was obtained by considering the phase curve and the seafloor temperature assuming that the BSR depth corresponds to the base of the hydrate stability zone. GTG was calculated from the above parameters as:

$$GTG = \frac{(T_{bsr} - T_{sf})}{(Z_{bsr} - Z_{sf})},$$

Where Z and T represent the depth and temperature respectively and the subscript *bsr* and *sf* corresponds to the BSR and seafloor respectively. The heat flow was calculated by multiplying GTG with the average thermal conductivity (0.82 W/mK) of the sediment as,

$$q = k_{avg} GTG$$

Where K_{avg} and GTG represent the average thermal conductivity and the geothermal gradient. The thermal conductivity was measured on the sediment cores collected onboard JOIDES Resolution (Collett et al., 2008).

We compute GTG for all seismic profiles individually. Along the NW-SE seismic profiles such as Line 15 (Fig. 2a), we observe an increase in GTG from 40 °C/km

to about 45 °C/km between CDPs 700 to 1000. The observed GTG is higher close to the fault system. Likewise, along Line 47 (Fig. 2b) the GTG increases from 38 °C/km to 45 °C/km between CDPs 650 to 850 close to the fault system F3-F5. The spatial distribution of GTG suggests that it increases from ~38 °C/km to ~45 °C/km towards the top of the mound. In general, anomalous GTG perturbation appears to be controlled by topography and the fault system in the study area. Further, GTG is higher towards the basinward side of the mound compared to that of landward side and *may* be related to increased width of the fault system in the basinward direction.

The mean thermal conductivity of the shallow sediment (< 200 m) in the site NGHP-01-10 measured onboard JOIDES resolution is about 0.82 W/mK with a standard deviation of 0.04 W/mK (Collett et al., 2008). The variation of the measured thermal conductivity in the shallow sediment is small (standard deviation of 0.04) and the presence of hydrate has insignificance influence on the bulk thermal conductivity (Grevenmeyer and Villinger, 2001), therefore, we ignore the variation in thermal conductivity and estimate the heat flow by taking the product of mean thermal conductivity and the BSR-derived GTG. The heat flow in this region increases towards the center of the mound from 31.16 W/m² to about 36.9 W/m².

Interpretation

Critical to understanding of fault-controlled hydrate distribution is a bathymetric mound (between CDPs 450 to 700 in Line 15A) which is bounded by the faults (F1 and F3; Figure 2). We interpret this mound on all 12 lines and estimate its elongation to be ~5 km length in NNW-SSE direction. The maximum relief of mound (using depth conversion with waver velocity) is ~30 m. Faults bounding the mound dip towards SSE and NNW direction. The throw (from depth scaling using stacking velocities) across the faults are ~20-30 m. The shaded relief map of multibeam swath bathymetry along with the available seismic lines also shows the extent and geometry of the mound.

Horizons and faults are interpreted on all lines for stratigraphic correlation (Fig. 2). The acoustic basement of the seismic profiles is marked by high amplitude, reverse polarity horizon (interpreted in magenta) which *may* represent the horizon with free gas. Other marker horizons on all lines are interpreted in orange, green, and dark blue. Major faults, F1-F5 (Figs. 2) are interpreted in all available seismic lines and the trace of the fault system is plotted on the seafloor map. The surface imprint of the fault system appears to be in NNW-SSE direction (Fig 5). Sites NGHP-01-10/21/12/13 where the presence of gas hydrates is confirmed by drilling (Collett et al., 2008) appear to be closely related to the interpreted fault system. The hydrate concentration in sites 12 and 13 was found to be far less than site 10. Although the sites are located close to each other (within a kilometer) the hydrate distribution appears to be heterogeneous; we believe that the heterogeneity is created by the fault system.

The SBP data across the topographic mound (Fig. 3) suggest two distinct geological strata; parallel continuous reflectors having a mound like structure and acoustically transparent masses having semi-prolonged bottom echo with regular overlapping hyperbolae suggesting mass transport deposits. These sediment deposits are conformable to the seafloor and onlap onto the mounded finely layered sediment. The surface imprint of the major faults (F1, F3 and F4) is observed in all the illustrated SBP profiles. In the central portion of horst structure, several closely spaced faults are observed. The NGHP-01-10 site is located close to the major fault F4.

The HRS data along the inline (Line 15; Fig. 2a) and crossline (Line 47; Fig. 2b) seismic profiles are illustrated in Fig. 4. The interpreted fault system are superimposed form the MCS lines. Due to the high frequency nature, the BSRs are not well defined except in few parts of model probably where the base of the hydrate stability zone is narrower. Amplitude blanking (reduction of acoustic impedance between layers *could be* due to the hydrates; Lee and Dillon, 2001) is widely observed. Prominent seismic blanking is observed between CDPs 650 to 950 in Fig. 4a while some seismic blanking is observed between CDPs 600 to 720 in Fig. 4b. Images indicate that zone of seismic blanking coincides with the region of fault system (F3-F5) further suggesting association of hydrate and the faulted region.

Discussion

In the KG basin, the direct evidence of the fracture filled gas hydrates comes from the X-ray images of the pressure cores. The analysis of LWD images, resistivity, and velocity logs of NGHP-01-10 site suggest the presence of gas hydrate filled high angle faults (Lee and Collett, 2009). The presence of fractures increases the secondary porosity and permeability of the sediment and result in focused fluid flow which increases the likelihood of gas hydrate formation (Ruppel and Kinoshita, 2000). In the seismic sections we have identified major fault systems (F1-F5) extending at least 200 m deep from the seafloor. The faults have created a horst-and-graben structure; the bathymetric mound is a horst. Site 10 which recovered massive hydrates is situated besides a horst structure. Several patches of locally increased velocity are observed in velocity model from modest processing of suggesting presence of hydrates in the vicinity of faults. The HRS data show blanking further suggesting presence of hydrates in the faulted stratigraphy. The lateral and vertical extent as well as the throw of the fault suggests that the fault system of this magnitude could be controlled by neotectonic activities and therefore could be regionally present in the K-G basin. It is therefore possible that the distribution of hydrates in the K-G basin is closely linked to fault distribution.

Indirect estimation of GTG and heat flow from the depth of the gas hydrate stability zone has been used to understand the thermal regime of the continental margins (Hyndman and Davis, 1992; Grevemeyer and Villinger, 2001). The heat

flow (q) primarily depends on the age of the crust (Stein and Stein, 1994) and can be calculated as,

$$q = 48 + 96 * e^{-0.0278*t} \quad (3)$$

Where t represents the age of the crust in Ma and the equation is valid for $t > 55$ ma. The study area is located in M11 magnetic anomaly (Ramana et al., 1994); hence we can assume the age of the crust to be ~ 130 Ma. Substituting the value for age of the crust in equation (3), we obtain the background heat flow to be about 50 m W/m². The heat flow also shows significant dependence on the nature of sediments, the sedimentation rate and age of the sediment. Assuming 100 % clay sediment (Collett et al., 2008) and a sedimentation rate of $\sim 20\text{-}30$ m/Ma, the correction factor will be of the order of 35-40 %. After accounting the correction due to sediment, we estimate the background heat flow to be in the range of 30 -32.5 m W/m². The background GTG estimated from heat flow assuming mean thermal conductivity of 0.82 W/mK will be about 36-40 °C/km.

BSR-derived GTG may differ from the actual GTG due to uncertainty in calculation of phase curves if the gas composition of the hydrates is not known, uncertainty in calculating the bottom water temperature, inaccuracy in estimating the depth of the reflectors due to unavailability or errors in velocity model and error in BSR depth estimation due to seismic anisotropy. Moreover, such discrepancy may also occur if the BSR depth does not correspond to the base of the hydrate stability zone due to capillary force arising in fine grained sediment (Ruppel, 1997). Additional errors in heat flow estimate may come from the uncertainties in estimating thermal conductivity and the effect of gas hydrates on thermal conductivity.

Results

The pressure cores and the log data of NGHP site 10 in KG offshore basin indicate that the distribution of gas hydrates are controlled by the fault/fracture. The origin of such fault system can be explained by neotectonic activities; we tentatively attribute the fault system to shale diapirism which is known to exist in KG basin. The gas-hydrates are preferentially distributed along the fault zone as indicated by velocity model. However, the BSR in the study area is observed throughout the mound and is formed due to the presence of free gas below the hydrate stability zone. The GTG and hence the heat flow increases by a factor of 15-20% at the center of the mound compared to that at flanks. We believe that the most likely cause of the increased GTG is due to the migration of deeply-originated fluid through the fault system.

Work Ahead

We are attempting to estimate a higher resolution velocity model through waveform inversion. The velocity model will also be used for rock-physics modeling and hydrate quantification.

Initial resolution tests for waveform inversion

Seismic data being used for the inversion have a broad frequency bandwidth of 10-120 Hz. However for the inversion purposes only a narrow bandwidth of 10-15 Hz is being used. Waveform inversion with synthetic data was performed using the real acquisition geometry. A maximum offset of 1.5 km was used. 91 shots were used in the inversion. The model from joint travelttime inversion and pre-stack depth migration (Figure 7a) was used as the starting model.

Waveform inversion was performed using the efficient inversion technique of Brenders and Pratt 2007. Starting with an initial travelttime model (Figure 7a), an initial source signature was estimated. 10Hz frequency was then inverted using this estimated source and the starting model was updated. The process was repeated for all frequencies in steps of 1Hz up to 15Hz. Updated model from previous inversion run was used as a starting model for inverting the next higher frequency. We were successfully able to recover a synthetic model with 100m checkerboard size and 10% perturbation strength. This is reflective of the perturbations we intend to resolve with the real data.

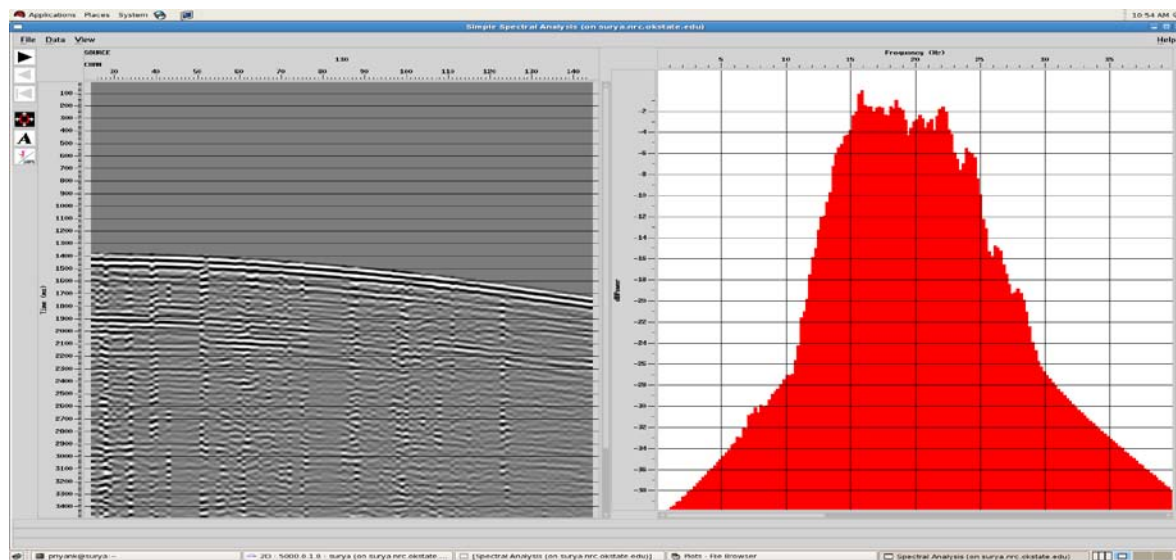


Figure 6. Amplitude spectrum of a representative shot used for waveform inversion with data muted above the seafloor reflection. Data have a dominant frequency in 15-20 Hz range.

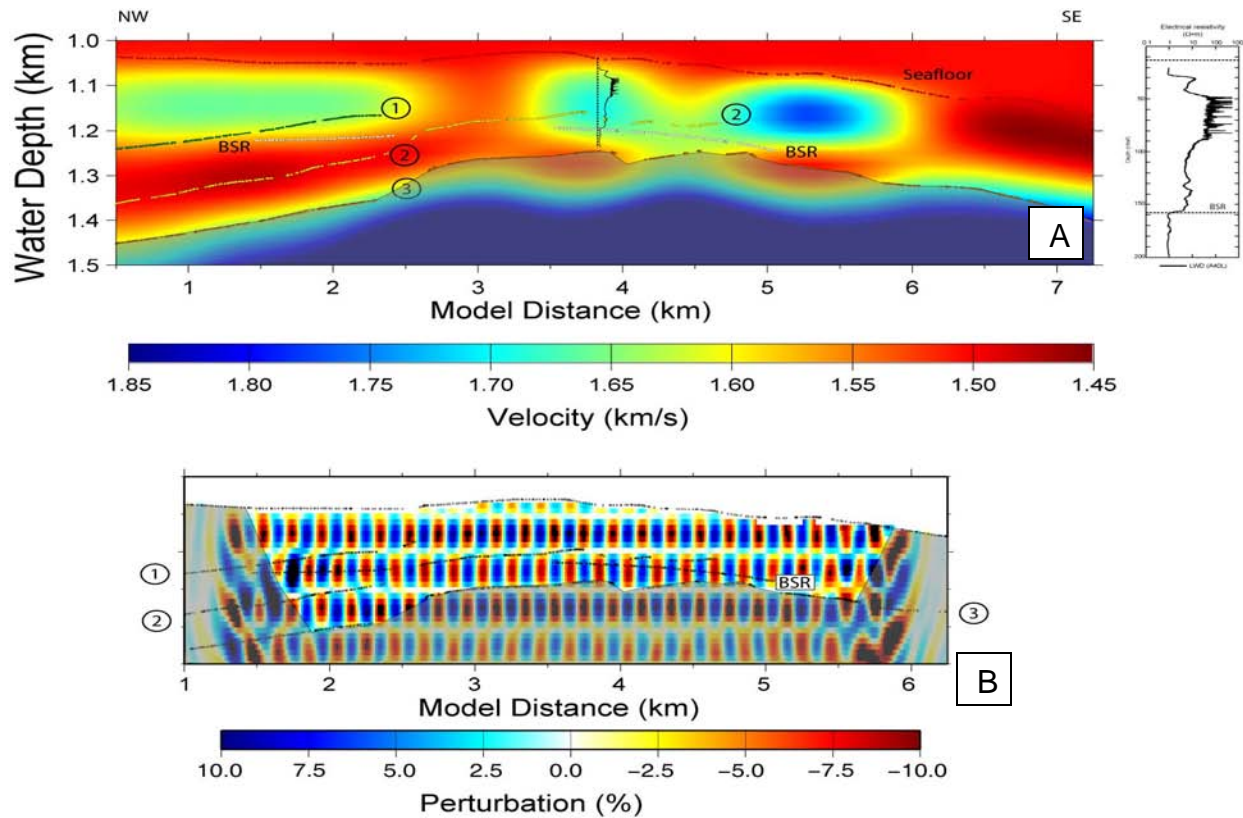


Figure 7: Waveform Inversion. a) Model from traveltime inversion. The sonic log is superposed on the model. This model was used as the starting model for waveform inversion. b) Recovered checkerboard model. The checkerboard size is 100m. Part of the model outside the zone of interest is shaded. Interfaces labeled 1 thru 3 and BSR is used for inversion of reflection arrival times.

Incomplete task description

Subtask 9.2 on waveform inversion remains incomplete due to a 6 month delay in computational facility setup at Oklahoma State University. The computation lab has been setup now and we have started working with the data as originally planned. We expect to be ready with the results by December 2010.

Subtask 9.3 on rock physics modeling will start from 08/10. This subtask will be done in collaboration with other groups that are being supported by DOE such as in Stanford. We have initiated collaborating with NIO, India, for initial rock physics modeling using velocity model from Subtask 9.1. We will initiate the collaboration with the Stanford group (or other groups as seen necessary) after estimating the waveform model.

Reference:

Brenders, A. J., and R. G. Pratt (2007), Full waveform tomography for lithospheric imaging: results from a blind test in a realistic crustal model, *Geophys. J. Int.*, 168, 133-151

- Caress, D.W., Chayes, D.N., 1996. Improved processing of hydrosweep DS multibeam data on the R/V Maurice Ewing. *Marine Geophysical Researches* 18, 631–650.
- Collett, T. S., et al., 2008. Results of the Indian National Gas Hydrate Program Expedition 01 initial reports, report, Director General of Hydrocarbons, Ministry of Petroleum and Natural Gas, New Delhi.
- Ganguly, N., Spence, G.D., Chapman, N.R., Hyndman, R.D., 2000. Heat flow variations from bottom simulating reflectors on the Cascadia margin. *Marine Geology* 164, 53–68.
- Grevemeyer, I., Villinger, H., 2001. Gas hydrate stability and the assessment of heat flow through continental margins. *Geophysical Journal International* 145(3), 647–660.
- Hyndman, R., Davis, E., 1992. A mechanism for the formation of methane hydrate and seafloor bottom-simulating reflectors by vertical fluid expulsion. *Journal of Geophysical Research* 97 (5), 7025–7041.
- Judd, A., Hovland, M., 2007. Seabed Fluid Flow: The Impact of Geology, Biology and the Marine Environment. Cambridge University Press.
- Lee, M., Collett, T., 2009. Gas hydrate saturations estimated from fractured reservoir at Site NGHP-01-10, Krishna-Godavari Basin, India. *Journal of Geophysical Research* 114(B7), B07102.
- Miles, P., 1995. Potential distribution of methane hydrate beneath the European continental margins. *Geophysical Research Letters* 22(23), 3179–3182.
- Pecher, I., Henrys, S., Wood, W., Kukowski, N., Crutchley, G., Fohrmann, M., Kilner, J., Senger, K., Gorman, A., Coffin, R., Richard B., Greinert, J., Faure, K., 2009. Focused fluid flow on the Hikurangi Margin, New Zealand—Evidence from possible local upwarping of the base of gas hydrate stability. *Marine Geology*. doi:10.1016/j.margeo.2009.10.006.
- Ruppel, C., 1997. Anomalously cold temperatures observed at the base of the gas hydrate stability zone, U.S. Atlantic passive margin. *Geology* 25, 699–704.
- Ruppel, C., Kinoshita, M., 2000. Heat, methane, and energy flux in an active margin gas hydrate province, offshore Costa Rica. *Earth and Planetary Science Letters* 179, 153–165.

Collaborations and Community Service

Jaiswal and Zelt have collaborated with National Institute of Oceanography for seismic and well data.

Task 10 Technology Transfer

Publications

Manuscript

Elevated Ocean Bottom Water Temperature and Abundant Marine Gas Hydrate in the Early Palaeogene. Guangsheng Gu, Gerald R. Dickens, Gaurav Bhatnagar, Frederick S. Colwell, George J. Hirasaki, Walter Chapman, *Nature Geoscience*, in revision.

Daigle, H., Dugan, B., in review, Origin and evolution of fracture-hosted methane hydrate deposits, *Journal of Geophysical Research*.

Waite, W.F, C. Santamarina, D. Cortes, B. Dugan, N. Espinoza, J. Germaine, J. Jang, J. Jung, T. Kneafsey, H. Shin, K. Soga, W. Winters, T-S. Yun, accepted pending revision, Physical properties of hydrate-bearing sediments, *Reviews of Geophysics*, 47, RG4003, doi:10.1029/2008RG000279.

Journal articles (draft manuscript) - Prepared the first draft for our manuscripts

3. "Pore water chemistry profiles across SMT above marine gas hydrates systems: A numerical modeling perspective" to be submitted to *Journal of Geophysical Research* (Chatterjee et al.)
4. "Analytical theory for relating depth of the sulfate-methane transition to gas hydrate saturation" to be submitted to *Geochemistry, Geophysics, Geosystems* (Bhatnagar et al.)
5. Guangsheng Gu, Walter Chapman, Priyank Jaiswal, George J. Hirasaki, Effect of Hydrocarbon Components on Hydrate/Gas Distribution and BSR, in preparation.

Conference presentations

Guangsheng Gu, Priyank Jaiswal, Walter Chapman, Colin Zelt, and George J Hirasaki, Compositional Effect on Hydrate/Free Gas Transition and BSR, American Geophysical Union Fall Meeting, 2008, San Francisco, CA. Poster.

Guangsheng Gu, Priyank Jaiswal, Walter Chapman, George J. Hirasaki, Effect of Hydrocarbon Components on Hydrate/Gas Distribution and BSR, SPE Gulf Coast Section, Regional Student Paper Contest, Houston, TX, April 17-18, 2009, (oral presentation).

Guangsheng Gu, Walter Chapman, Priyank Jaiswal, George J. Hirasaki, Effect of Hydrocarbon Components on Hydrate/Gas Distribution and BSR. DOE Methane Hydrate Meeting, Georgia Tech University, Atlanta, GA, Jan 25-29, 2010 (oral presentation).

S. Chatterjee, G. Bhatnagar, W. G. Chapman, G. R. Dickens, B. Dugan, G. J. Hirasaki, "Sulfate, Alkalinity, Calcium and Carbon isotope $\delta^{13}\text{C}$ profiles as an indicator of upward methane flux", (oral presentation) American Geophysical Union (AGU) Fall meeting, San Francisco, CA, December 2009

S. Chatterjee, G. Bhatnagar, W. G. Chapman, B. Dugan, G. R. Dickens, G. J. Hirasaki, "Carbon cycling across sulfate-methane transition above marine gas hydrate systems", (oral presentation) Society of Petroleum Engineers (SPE) Gulf-coast regional student paper contest, Lubbock, TX, April 2010

S. Chatterjee, G. Bhatnagar, W. G. Chapman, B. Dugan, G. R. Dickens, G. J. Hirasaki, "Sulfate-Methane Transition depth as a proxy for methane flux above gas hydrate systems", (selected for poster presentation) Gordon Research Conference – Natural gas hydrate systems, Waterville, ME, June 2010

Daigle, H., Dugan, B., 2009, Fracture genesis in methane hydrate systems, Rice University Department of Earth Science seminar, Houston, TX (17 November 2009).

Daigle, H., Dugan, B., 2009, Fracture genesis and fracture filling in methane hydrate systems, American Geophysical Union Fall Meeting, San Francisco, CA (17 December 2009).

Daigle, H., Dugan, B., 2010, Origins of fracture-hosted methane hydrates, Chevron technology talk, Houston, TX (11 March 2010).

DOE methane hydrate meeting, Georgia Tech University, Atlanta, GA

8. *Carbon cycling across SMT above marine gas hydrates systems: A numerical modeling perspective* – Monday Jan 25, 2010
9. *Effect of lithologic heterogeneity on gas hydrate distribution* – Wednesday Jan 27, 2010
10. Effect of Hydrocarbon Components on Hydrate/Gas Distribution and BSR. Guangsheng Gu, Walter Chapman, Priyank Jaiswal, George J. Hirasaki, DOE Hydrate Meeting, 2010 Jan 25-29, Atlanta, GA.

Daigle, H., 2009, Fracture genesis and fracture filling in methane hydrate systems, DOE/NETL Methane Hydrate Workshop, Atlanta, GA (26 January 2010).

Dugan, B., 2010, Physical properties studies: flow, fractures, and failures, DOE/NETL Methane Hydrate Workshop, Atlanta, GA (26 January 2010).

Guangsheng Gu, Sayantan Chatterjee, George J. Hirasaki, Walter G. Chapman, Brandon Dugan, Gaurav Bhatnagar, Colin Zelt, Gerald Dickens, Priyank Jaiswal, 2-D Simulation on Hydrate Accumulation in Different Heterogenous Lithology Structures, Gordon Research Conference on Natural Gas Hydrate Systems, Waterville, ME, June 6-11, 2010 (poster).

Brandon Dugan, Hugh Daigle, Sayantan Chatterjee, Guangsheng Gu, George Hirasaki, Continuum models of large-scale phenomena associated with hydrate-bearing sediments, Gordon Research Conference on Natural Gas Hydrate Systems, Waterville, ME, June 6-11, 2010 (oral presentation).

Hydrate Collaborations and Community Service

Dugan was a member of the panel discussion on Gas Hydrates and Slope Stability at the Submarine Mass Movements and Their Consequences Symposium, Austin, TX, November 7-12, 2009.

Dugan has opened hydrate-related collaborations with M. Riedel (Pacific Geoscience Center, British Columbia, Canada) and N. Scholz (University of Victoria, British Columbia, Canada) to model the hydrate formation and slope failure along the Cascadia margin and with Xiujuan Wang (Institute of Oceanology, Chinese Academy of Sciences) to study flow systems related to heterogeneous hydrate accumulations in the South China Sea and to compare them with the Gulf of Mexico.

Dugan has also been collaborating with the Chevron Gulf of Mexico JIP team to develop the science plan for Leg III in 2011. Dugan is leading the physical properties science plan initiative that will be integrated with the overall science plan to meet the objectives of the JIP in 2011.

Dr. George Hirasaki, Dr. Walter Chapman and Guangsheng Gu are contacting Dr. Dendy Sloan and Dr. Carolyn Koh in Colorado School of Mines for collaboration on multi-hydrocarbon flash calculation.

Jaiswal and Zelt have collaborated with National Institute of Oceanography for seismic and well data.

DOE Grants R15620, RO15621, RO15622

6/25/2010

Phase 4

COST PLAN / STATUS

Phase	Phase 1	Phase 2	Phase 3	Phase 4 7/01/09 – 7/16/10				Phase 4	Phase 5
Baseline period	10/06-6/07	7/07-6/08	7/08-6/09	7/1/09 - 9/30/09	10/1/09 - 12/31/09	1/1/10 - 3/31/10	4/1/10 - 7/16/10 <i>(estimated)</i>	Totals 7/01/09-7/16/10	7/17/10 – 7/16/11
<u>Baseline Cost Plan Allocation</u>									
Federal Share	\$ 3,624	\$320,010	\$ 331,135	\$ 89,012	\$ 89,012	\$ 89,012	\$ 89,012	\$ 356,048	\$259,335
Non-Federal Share	\$ 1,004	\$114,613	\$ 107,630	\$ 27,622	\$ 27,622	\$ 27,622	\$ 27,622	\$ 110,488	\$114,363
Total Planned	\$ 4,628	\$434,623	\$ 438,765	\$ 116,634	\$ 116,634	\$ 116,634	\$ 116,634	\$ 466,536	\$373,698
Cumulative Baseline Cost	\$ 4,628	\$439,251	\$ 878,016	\$ 116,634	\$ 116,634	\$ 116,634	\$ 116,634	\$ 1,344,552	\$1,718,250
<u>Actual Incurred Cost</u>									
Federal Share	\$ 3,082	\$298,506	\$ 242,993	\$ 74,631	\$30,585	\$33,930	\$205,854	\$345,000	
Non-Federal Share	\$ 1,091	\$118,145	\$ 95,520	\$ 5,078	\$27,043	\$27,043	\$54,879	\$114,043	
Total Incurred	\$ 4,173	\$416,651	\$ 338,513	\$ 79,709	\$57,628	\$60,973	\$260,733	\$459,043	
Cumulative Costs	\$ 4,173	\$420,824	\$ 759,337	\$ 79,709	\$137,337	\$198,310	\$459,043	\$1,218,380	
<u>Variance (plan-actual)</u>									
Federal Share	\$ 542	\$ 21,504	\$ 88,142	\$ 14,381	\$58,427	\$55,082	<i>(\$116,842)</i>	\$11,048	
Non-Federal Share	<i>\$ (87)</i>	<i>\$ (3,533)</i>	\$ 12,110	\$ 22,544	\$579	\$579	<i>(\$27,257)</i>	<i>(\$3,555)</i>	
Total Variance	\$ 455	\$ 17,971	\$ 100,252	\$ 36,925	\$59,006	\$55,661	<i>(\$144,099)</i>	\$7,493	
Cumulative Variance	\$ 455	\$ 18,426	\$ 118,678					\$126,171	

Milestone Plan/Status

Task	Milestone: Status and Results	Date	Status
5. Carbon inputs and outputs to gas hydrate systems	<p>5.1a Measure iodine in sediments We have measured iodine concentrations in pore waters and sediments from 4 gas hydrate systems.</p>	12/07	Done (except writing)
	<p>5.1b Constrain C_{org} inputs from iodine We have measured the content and isotopic composition of organic carbon and carbonate in sediment from cores of several gas hydrate systems. We are beginning to incorporate the results into models.</p>	10/08	Partly Done
	<p>5.2a Construct metal profiles in sediments We have measured metal contents in pore water and sediment from cores of two gas hydrate systems along the Peru Margin and in the Sea of Japan. The Sea of Japan work has been published (Snyder et al., 2007).</p>	12/09	Done (except writing)
	<p>5.2b Modeling/integrating profiles We are beginning to incorporate the results into models. We have written an article defending our use of the SMT as a proxy for methane loss through AOM.</p>	12/10	Begun

6. Numerical models for quantification of hydrate and free gas accumulations	<p>6.1 Model development. The recipient shall develop finite difference models for the accumulation of gas hydrate and free gas in natural sediment sequences on geologically relevant time scales.</p>	9/07	Done
	<p>6.2: Conditions for existence of gas hydrate The recipient shall summarize, quantitatively, the conditions for the absence, presence, and distribution of</p>	3/07	Done

	gas hydrates and free gas in 1-D systems by expressing the conditions in terms of dimensionless groups that combine thermodynamic, biological and lithologic transformation, and transport parameters.		
	<p>6.3 Compositional effect on BSR</p> <p>The recipient shall add to the numerical model, developed under this task, multi-hydrocarbon capability specifically to investigate how existence of multi-hydrocarbon components might affect Bottom Simulating Reflectors (BSRs).</p>	7/07 (new: 6/11)	Simple case done (writing manuscript); complex cases on going
	<p>6.4: Amplitude Attenuation and chaotic zones due to hydrate distribution</p> <p>The recipient shall simulate preferential formation of gas hydrate in coarse-grained, porous sediment in 1-D and 2-D by linking fluid flux to the permeability distribution and evolution.</p>	3/09 (new: 6/11)	ongoing
	<p>6.5: Processes leading to overpressure</p> <p>The recipient shall quantify, by simulation and summarize by combination of responsible dimensionless groups, the conditions leading to overpressure to the point of sediment failure.</p>	3/08 (new: 6/11)	1D written and published; 2D near completion and need to write results (Collaborating with task 8)
	<p>6.6 Concentrated hydrate and free gas</p> <p>The recipient shall, using 2-D models, simulate lateral migration and concentration of gas hydrate and free gas in structural and stratigraphic traps.</p>	3/08 (new: 6/11)	Ongoing; one manuscript in press (Daigle et al.)
	<p>6.7 Focused free gas, heat and salinity</p> <p>The recipient shall quantify, using 1-D and 2-D model</p>	9/09 (new:	Ongoing case studies,

	simulations and comparisons to available observations, the factors controlling the process of localized upward migration of free gas along faults and lateral transfer to dipping strata that can lead to chaotic zones and possible accumulations of concentrated hydrate.	6/11)	models work and general results near submission
	6.8a Sulfate profile as indicator of methane flux The recipient shall compute, for systems where data on the sulfate profile is available, the oxidation of methane by sulfate and shall indicate the perceived level of effect on gas hydrate accumulation and the data's value as an indicator of methane flux.	7/07	Done, and published
	6.8b Carbon cycling across SMT above marine gas hydrate systems. The recipient shall compute, for systems where data on the sulfate, bicarbonate (DIC), calcium, carbon isotope profiles are available, the reduction of sulfate by methane and by particulate organic carbon and shall indicate the perceived level of effect on gas hydrate accumulation and the depth to the SMT as an indicator of methane flux.	6/10	Done, finalizing manuscript for submission
	6.9 Application of models to interpretation of case studies. The models developed in Task 6 will be applied to case studies in the interpretation of each of the other tasks.	6/11	Started and working 2D system, manuscripts should be submitted by 06/11
7. Analysis of production strategy	7.1a Pore scale model development and Hydrate code comparison For this milestone, we will develop pore-scale models of hydrate accumulation by simulation. Our hydrate code will be used to solve a set of problems formulated by the Code Comparison Study group. Our results will be compared with those of other hydrate codes. Should be changed to: 6/08 Reason: The starting date was moved to 6/07 Status: Code comparison study is 100% complete.	1/08	6/08 This task is complete

	<p>7.1b Petrophysical and thermophysical properties of hydrate sediments from pore-scale model</p> <p>For this milestone, we will assume the pore-scale models of hydrate accumulation developed in the last milestone and estimate transport properties as a function of hydrate and gas saturations.</p> <p>Should be changed to: 6/09 Reason: The starting date was moved to 6/07</p>	1/09	6/09 This task is complete
	<p>7.2a Modeling of several production strategies to recover gas from marine hydrates</p> <p>Several production strategies would be modelled using the transport property correlations developed in the previous milestone. Optimal strategies will be identified.</p> <p>Should be changed to: 6/10</p>	1/10	On schedule
	<p>7.2b Effect of marine reservoir heterogeneities on production of methane</p> <p>Reservoir heterogeneity anticipated in marine environments (known or determined through other tasks) would be incorporated. Appropriate hydrate distributions, either constrained from experimental data or mechanistic simulations (Task 5) would be used. Sensitivity of gas production to the heterogeneities would be calculated.</p> <p>Should be changed to: 6/11 Reason: The starting date was moved to 6/07 Status: Have not started</p>	12/10	This task will start in 6/10
8. Seafloor and borehole stability	<p>8.1a Collection of data</p> <p>We have collected the published data and are working it into a data base. We are also working on a review paper summarizing the state of the art settings. This will include laboratory experiments, field data, published results, and unpublished data.</p>	05/08	Completed
	<p>8.1c Complete database</p> <p>We are organizing the data from task 8.1a into a format that can be searched and used by researchers trying to understand mechanical behavior of hydrate-bearing sediment. We will also identify key gaps in the database for focusing future hydrate research endeavors. We have started exchanging these data with the modeling components of this project.</p>	6/10	Done

	<p>8.2a Link database with models</p> <p>We have started passing data along to the modeling groups so they can use sediment properties from hydrate provinces as they simulate hydrate accumulation and production.</p>	6/11	Done, by 6/11 will be done with very high permeability contrasts
	<p>8.2b Add sediment stability to models</p> <p>Standard stability calculations have been implemented in a standard basin model. Now that it is functional we will work with the hydrate accumulation model to add a stability calculation to the 2-D models.</p>	6/10	Done
	<p>8.2c Conditions for (in)stability</p> <p>After implementing the stability model in the hydrate accumulation code, we can explore the conditions (e.g., hydrate dissociation, sea-level fall) that could drive slope failure and hydrate/methane release or lead to borehole failures during production.</p>	6/11	Ongoing, and will have general and case studies by 06/11
9 Geophysical imaging of hydrate and free gas	<p>9.1 Preliminary processing and inversion of seismic data.</p> <p>Perform conventional seismic reflection processing, velocity analysis, travel time tomography, and other analyses as deemed appropriate and necessary.</p>	8/08	Done Article in progress.
	<p>9.2: Final 1-D elastic and 2-D acoustic waveform inversion.</p> <p>Apply 1-D elastic and 2D acoustic inversions on data obtained from subtask 9.1 to derive determine high-resolution elastic and acoustic properties.</p>	8/09	Partly done. Delayed by 6 months due to computational facility setup at Oklahoma State University. Results expected in Decemb

			er 2010.
	<p>9.3: Rock physics modeling.</p> <p>Apply rock physics models to the developed seismic models to estimate hydrate saturation and lithology through application of well log data in conjunction with data from subtask 9.2. For this subtask we shall seek to collaborate with research being conducted under separately funded DOE-NETL projects (DE-FC26-05NT42663 with Stanford University, "Seismic-Scale Rock Physics of Methane Hydrate" and others as applicable).</p>	8/10	On Target

SUCCESS CRITERIA

Task 5: Carbon Inputs and Outputs to Gas Hydrate Systems

Subtask 5.1a Measure iodine in sediments

What has been done:

We completed iodine measurements in pore waters and sediments from 4 gas hydrate systems by 12/2007. We have spent considerable effort placing these results into a larger context, now completing a major synthesis of iodine in marine sediment. We have presented some of this work at conferences. We have a nearly polished manuscript almost ready for submission.

To be completed:

The manuscript needs to be written.

Subtask 5.1b Constrain C_{org} inputs from iodine

What has been done:

We have measured the organic content and its isotope composition in sediment above several gas hydrate systems. Some of the results have now been incorporated into our numerical models.

To be completed:

Additional analyses on new samples collected from the Sea of Japan (iodine and carbon isotopes were not measured on previous samples). Need to complete the combined and coupled modeling of gas hydrate formation and iodine cycling, and write and submit a manuscript.

Subtask 5.2a Construct metal profiles in sediments

What has been done:

We have measured metal contents in sediment cores from the Peru Margin, Sea of Japan and Gulf of Mexico. A manuscript has been published on the Sea of Japan work. Drafts have been written for the Peru Margin and Gulf of Mexico work.

To be completed:

Additional analyses on new samples collected from the Sea of Japan. The papers need to be completed.

Publications:

Snyder, G.T., A. Hiruta, R. Matsumoto, G.R. Dickens, H. Tomaru, R. Takeuchi, J. Komatsubara, Y. Ishida, and H. Yu, 2007, Authigenesis in marine sediments of Umitaka Spur, Japan Sea: Distribution and implications for the development of gas-charged systems. Deep-Sea Research II, 54, 1216-1239.

Subtask 5.2b Modeling/integrating profiles

What has been done:

We have placed our data into the numerical models for gas hydrate formation. We have written one article on a basic finding. We have presented this work at several recent meetings, and have preliminary drafts of two papers. This work is now heavily linked with Task 6.

To be completed:

The papers need to be completed and submitted.

Publications:

Dickens, J. and G.T. Snyder, 2009, Interpreting upward methane flux from pore water profiles, Fire in the Ice, National Energy Technology Laboratory Methane Hydrate Newsletter, Winter, 7-10.

Task 6: Numerical Models for Quantification of Hydrate and Free Gas Accumulations

Subtask 6.1: Model development.

What has been done:

This work has been finished by 09/2007, presented on many conferences, and manuscripts have been published:

Bhatnagar, G., W.G. Chapman, G.R. Dickens, B. Dugan, G.J. Hirasaki, 2007, Generalization of gas hydrate distribution and saturation in marine sediments by scaling of thermodynamic and transport processes, American Journal of Science, 307(6), 861-900, doi:10.2475/06.2007.01.

To be completed:

Well finished.

Subtask 6.2: Conditions for existence of gas hydrate.

What has been done:

This work has been finished by 03/2007, presented on many conferences, and manuscripts have been published:

G. Bhatnagar, W.G. Chapman, G.R. Dickens, B. Dugan, and G.J. Hirasaki, Scaling of Thermodynamic and Transport Processes for Predicting Methane Hydrate Saturation in Marine Sediments Worldwide, SPE Annual Technical Conference

and Exhibition, 24-27 September 2006, San Antonio, Texas, USA, SPE 106519-STU, 10.2118/106519-STU.

Bhatnagar, G., W.G. Chapman, G.R. Dickens, B. Dugan, G.J. Hirasaki, 2007, Generalization of gas hydrate distribution and saturation in marine sediments by scaling of thermodynamic and transport processes, American Journal of Science, 307(6), 861-900, doi:10.2475/06.2007.01.

To be completed:

Well finished.

Subtask 6.3: Compositional effect on BSR.

What has been done:

(1) We have used calculate the saturation and composition profiles for simple cases. When propane or ethane is existing together with methane, with constant overall composition assumption. From the work we have finished, we have found out that existence of another gas component in marine hydrate system, can affect the hydrate and gas distribution greatly. A thick transition region in which Aqueous, Hydrate and Free-gas phases can co-exist, and S_H and S_V can change gradually. The transition zone can be as thick as 300 m, comparable to thickness of GHSZ.

(2) Rock property model has been used to compute the vertical profile of acoustic impedance. For example, in the system we studied, the p-wave velocity V_p , can vary gradually throughout this transition zone.

(3) We have also built tools to generate 1D and 2D synthetic seismograms, with Ricker wavelets as source signals. The 1D tool is a code built by ourselves; the 2D code is revised from a waveform simulation code built by Dr. Gerhard Pratt. 2D synthetic seismograms have been tested successfully for simple cases, and 1D for complex cases.

This work has been presented in many conferences. A manuscript is in preparation on this topic.

Compositional Effect on Hydrate/Free Gas Transition and BSR, Guangsheng Gu, Priyank Jaiswal, Walter Chapman, Colin Zelt, and George J Hirasaki, American Geophysical Union Fall Meeting, 2008, San Francisco, CA. Poster.

Effect of Hydrocarbon Components on Hydrate/Gas Distribution and BSR, Guangsheng Gu, Priyank Jaiswal, Walter Chapman, George J. Hirasaki, SPE Gulf Coast Section, Regional Student Paper Contest, Houston, TX, April 17-18, 2009, (oral presentation).

Effect of Hydrocarbon Components on Hydrate/Gas Distribution and BSR. Guangsheng Gu, Walter Chapman, Priyank Jaiswal, George J. Hirasaki, DOE Methane

Hydrate Meeting, Georgia Tech University, Atlanta, GA, Jan 25-29, 2010 (oral presentation).

To be completed:

We'll build our own code to deal with complex cases, with consideration of advection, diffusion, and so on. Since the ability of flash calculation on multi-hydrocarbon system is dependent on available routines or softwares, we'll demonstrate our work on limited systems, for example, methane-propane system, or methane – ethane system. This will be completed before 6/11.

Subtask 6.4: Amplitude Attenuation and chaotic zones due to hydrate distribution.

What has been done:

(1) We have built 2-D codes successfully. Some simulation has been done on preferential formation of gas hydrate in coarse-grained, porous sediment in 2-D by linking fluid flux to the permeability distribution. Results have been presented in recent conferences.

(2) Some rock property model has been applied to evaluate the acoustic impedance from the lithology and hydrate distribution.

(3) Tools have been prepared, and will be used to generate synthetic seismograms. We'll quantify the effects of hydrate and free gas accumulation on seismic response.

Results presented on conferences:

Guangsheng Gu, Sayantan Chatterjee, George J. Hirasaki, Walter G. Chapman, Brandon Dugan, Gaurav Bhatnagar, Colin Zelt, Gerald Dickens, Priyank Jaiswal, 2-D Simulation on Hydrate Accumulation in Different Heterogenous Lithology Structures, Gordon Research Conference on Natural Gas Hydrate Systems, Waterville, ME, June 6-11, 2010 (poster).

Brandon Dugan, Hugh Daigle, Sayantan Chatterjee, Guangsheng Gu, George Hirasaki, Continuum models of large-scale phenomena associated with hydrate-bearing sediments, Gordon Research Conference on Natural Gas Hydrate Systems, Waterville, ME, June 6-11, 2010 (oral presentation).

To be completed:

We'll do more simulation to test hypothesis on amplitude blanking and chaotic zone, and if approved, to quantify relationships. To be completed before 6/11.

Subtask 6.5: Processes leading to overpressure

What has been done:

1D model works fine, manuscripts published; 2D model of overpressure works fine, manuscript to be completed by 6/2011.

Publications:

Bhatnagar, G., W.G. Chapman, G.J. Hirasaki, G.R. Dickens, B. Dugan, 2008, Effect of overpressure on gas hydrate distribution, Proc. 6th International Conf. Gas Hydrates (ICGH 2008), Vancouver, BC, Canada, 6-10 July 2008.

Hustoft, S., Dugan, B., Mienert, J., 2009, Effects of rapid sedimentation on developing the Nyegga pockmark-field; Constraints from hydrological modeling and 3-D seismic data, offshore mid-Norway, Geochemistry, Geophysics, Geosystems, 10(6), Q06012, doi:10.1029/2009GC002409.

To be completed:

2D work is near completion and need to write results (Collaborating with task 8).

Subtask 6.6: Concentrated hydrate and free gas**What has been done:**

We have built 2-D codes successfully. Accumulation of gas hydrate and free gas is being modeled in heterogeneous marine sediments over geologic time scales. The two-dimensional numerical model incorporates deposition and compaction of heterogeneous sediments, methane generation, and migration of water with dissolved gas. Fracture network systems and dipping sand layers are common examples of lithologic heterogeneities in natural gas hydrate systems, and are simulated using the current 2-D model. Increased fluid flux within these high permeability conduits results in concentrated hydrate deposits. Simulations are also currently being done with multiple fracture network column and parallel sand layers. Encouraging results have been presented in recent conferences, showing that high permeability conduits are very helpful for hydrate/free gas accumulation.

Publications:

Daigle, H., Dugan, B., in press, Origin and evolution of fracture-hosted methane hydrate deposits, Journal of Geophysical Research, 2010JB007492.

Presentations:

Guangsheng Gu, Sayantan Chatterjee, George J. Hirasaki, Walter G. Chapman, Brandon Dugan, Gaurav Bhatnagar, Colin Zelt, Gerald Dickens, Priyank Jaiswal, 2-D Simulation on Hydrate Accumulation in Different Heterogenous Lithology Structures, Gordon Research Conference on Natural Gas Hydrate Systems, Waterville, ME, June 6-11, 2010 (poster).

Brandon Dugan, Hugh Daigle, Sayantan Chatterjee, Guangsheng Gu, George Hirasaki, Continuum models of large-scale phenomena associated with hydrate-bearing sediments, Gordon Research Conference on Natural Gas Hydrate Systems, Waterville, ME, June 6-11, 2010 (oral presentation).

To be completed:

To do more simulation to study 2-D lithologic structure and hydrate/free gas accumulation.

Manuscripts to be completed by 6/2011.

Subtask 6.7 Focused free gas, heat and salinity.

What has been done:

2-D codes are ready. Simulations on focused upward migration of free gas along faults and lateral transfer to dipping strata have been performed. High saturations of gas and hydrate have been obtained. Results have presented in conferences.

Publications:

Daigle, H., Dugan, B., in press, Origin and evolution of fracture-hosted methane hydrate deposits, *Journal of Geophysical Research*, 2010JB007492.

Daigle, H., Dugan, B., manuscript to be submitted by 09/2011, Effects of multiphase methane supply on hydrate accumulation and fracture generation, *Geophysical Research Letters*.

To be completed:

More simulation will be performed to study the effects of lithlogic structure and other parameters on hydrate and free gas accumulation and migration. Work will be completed, and manuscripts drafted by 6/11.

Subtask 6.8a Sulfate profile as indicator of methane flux

What has been done:

Work has been completed, and manuscripts published.

Publications:

Bhatnagar, G., W.G. Chapman, G.R. Dickens, B. Dugan, G.J. Hirasaki, 2008, The sulfate-methane transition as a proxy for average methane hydrate saturation in marine sediments, *Geophysical Research Letters*, 35, L03611, doi:10.1029/2007GL032500.

Bhatnagar, G., W.G. Chapman, G.J. Hirasaki, G.R. Dickens, B. Dugan, 2008, Relating gas hydrate saturation to depth of sulfate-methane transition, Proc. 6th International Conf. Gas Hydrates (ICGH 2008), Vancouver, BC, Canada, 6-10 July 2008.

Subtask 6.8b Carbon cycling across SMT above marine gas hydrate systems

What has been done:

Work has been completed, and manuscripts to be submitted.

Computed carbon and sulfur mass balance in marine sediments at various sites e.g. Hydrate Ridge, and Keathley Canyon, GoM) with finite upward methane flux.

Bicarbonate (DIC), calcium, carbon isotope profiles were modeled in addition to methane and sulfate profiles to interpret upward methane flux from deeper hydrate bearing sediments. Computed steady state profiles are in good agreement with the observed profiles at these sites. The geochemical profiles across the SMT is interpreted to be a result of sulfate reduction by the AOM reaction at the SMT. This interpretation enabled the depth to the SMT to be used as indicator for upward methane flux, and the average hydrate saturation in the underlying sediments. With these results, shallow sulfate profiles could now be used to indicate methane flux from below.

Manuscripts:

- Bhatnagar, G., S. Chatterjee, W.G. Chapman, B. Dugan, G.R. Dickens, G.J. Hirasaki, Analytical theory for relating depth of the sulfate-methane transition to gas hydrate saturation. [Draft manuscript being finalized for submission].
- S. Chatterjee, Bhatnagar, G., W.G. Chapman, B. Dugan, G.R. Dickens, G.J. Hirasaki, Pore water chemistry profiles across sulfate-methane transition above gas hydrate systems: A numerical modeling perspective. [Draft manuscript being finalized for submission].

Presentations:

- S. Chatterjee, G. Bhatnagar, W. G. Chapman, B. Dugan, G. R. Dickens, G. J. Hirasaki, *Sulfate-Methane Transition depth as a proxy for methane flux above gas hydrate systems*, (poster) Gordon Research Conference – Natural gas hydrate systems, Waterville, ME, June 2010
- S. Chatterjee, G. Bhatnagar, W. G. Chapman, B. Dugan, G. R. Dickens, G. J. Hirasaki, *Carbon cycling across sulfate-methane transition above marine gas hydrate systems*, (oral presentation) Society of Petroleum Engineers (SPE) Gulf-coast regional student paper contest, Lubbock, TX, April 2010
- S. Chatterjee, G. Bhatnagar, W. G. Chapman, B. Dugan, G. R. Dickens, G. J. Hirasaki, *Carbon cycling across SMT above marine gas hydrates systems: A numerical modeling perspective*, DOE methane hydrate meeting, Georgia Tech University, Atlanta, GA, Monday Jan 25, 2010
- S. Chatterjee, G. Bhatnagar, W. G. Chapman, G. R. Dickens, B. Dugan, G. J. Hirasaki, *Sulfate, Alkalinity, Calcium and Carbon isotope $\delta^{13}\text{C}$ profiles as an indicator of upward methane flux*, (oral presentation) American Geophysical Union (AGU) Fall meeting, San Francisco, CA, December 2009

6.9 Application of models to interpretation of case studies.

What has been done:

The models developed in Task 6 will be applied to case studies in the interpretation of each of the other tasks.

Models have been tested and are being adapted for case studies offshore India and in Gulf of Mexico.

To be completed:

Some case studies will be finished to show that our simulations are helpful to explain case data and phenomena. Manuscripts will be finished. To be completed by 6/11.

Task 7: Analysis of Production Strategy

Subtask 7.1a Pore scale model development and hydrate code comparison

What has been done:

Model developed and code comparison study complete

Subtask 7.1b Petrophysical and thermophysical properties of hydrate sediment from pore-scale model

Publications:

Phirani, J., Pitchumani, R., & Mohanty, K. K., 2009, Transport Properties of Hydrate Bearing Formations from Pore-Scale Modeling, SPE 124882, Proceedings of SPE ATCE, New Orleans, LA, Oct. 4-7, 2009.

Subtask 7.2a Modeling several production strategies to recover gas from marine gas hydrates

Publications:

Phirani, J., Mohanty, K. K. & G. Hirasaki, 2009, Warm Water Flooding of Unconfined Gas Hydrate Reservoirs, Energy & Fuels, doi:10.1021/ef900291j.

Phirani, J., Hirasaki, G., & Mohanty, K. K., submitted to Chem. Eng., Production Strategy for an Unconfined Marine Hydrate Reservoir.

Subtask 7.2b Effect of marine reservoir heterogeneities on production of methane hydrate

What has been done:

Started in 06/2010; anticipate manuscript by 06/2011

Task 8: Seafloor and Borehole Stability

Subtask 8.1a Collection of data and 8.1b Complete database

What has been done:

Database submitted

Publications:

Daigle, H., Dugan, B., 2009, Extending NMR Data for Permeability Estimation in Fine-Grained Sediments, Marine and Petroleum Geology, 26, 1419-1427, doi:10.1016/j.marpetgeo.2009.02.008.

Dugan, B., 2008, Fluid Flow in the Keathley Canyon 151 Mini-Basin, Northern Gulf of Mexico, Marine and Petroleum Geology, 25, 919-923, doi:10.1016/j.marpetgeo.2007.12.005.

Waite, W.F., C. Santamarina, D. Cortes, B. Dugan, N. Espinoza, J. Germaine, J. Jang, J. Jung, T. Kneafsey, H. Shin, K. Soga, W. Winters, T-S. Yun, 2009, Physical properties of hydrate-bearing sediments, *Reviews of Geophysics*, 47, RG4003, doi:10.1029/2008RG000279.

Winters, W.J., B. Dugan, T.S. Collett, 2008, Physical Properties of Sediments from Keathley Canyon and Atwater Valley, JIP Gulf of Mexico Gas Hydrate Drilling Program, *Marine and Petroleum Geology*, 25, 896-905, doi:10.1016/j.marpetgeo.2008.01.018.

Subtask 8.2a Link database with models 01/10, done, by 6/11 will be done with very high permeability contrasts

What has been done:

All models are using realistic sediment properties based on data assimilated, aiding parameter evaluation and case studies

Subtask 8.2b Add sediment stability to models

What has been done: Models developed in 1D and 2D and benchmarked.

Subtask 8.2c Conditions for (in)stability

Publications:

Daigle, H., Dugan, B., in press, Origin and evolution of fracture-hosted methane hydrate deposits, *Journal of Geophysical Research*, 2010JB007492.

Hustoft, S., Dugan, B., Mienert, J., 2009, Effects of rapid sedimentation on developing the Nyegga pockmark-field; Constraints from hydrological modeling and 3-D seismic data, offshore mid-Norway, *Geochemistry, Geophysics, Geosystems*, 10(6), Q06012, doi:10.1029/2009GC002409.

Manuscript on failures in Cascadia is being developed; models have been completed.

Task 9: Geophysical Imaging of Gas Hydrate and Free Gas Accumulations

Subtask 9.1 Preliminary processing and inversion of seismic data

What has been done:

Jaiswal, P., Zelt, C.A., and Dewangan, P., Gas Hydrates in the Krishna-Godavari Basin, East Coast India, 71th EAGE Conference, Amsterdam, EAGE Expanded Abstracts, 2009.

Dewangan, P., Ramprasad, T., and Jaiswal, P., Fault controlled focused fluid flow in the vicinity of NGHP-01-10 site, Krishna-Godavari basin, Bay of Bengal, *Marine and Petroleum Geology*, submitted.

Manuscript on traveltime inversion is being developed.

Subtask 9.2 Final 1D and 2D waveform inversions

What has been done:

Due to the development of seismic lab at Oklahoma State University, subtask 9.2 is delayed. We have started working on this sub-task since January 2010. Currently we have obtained encouraging initial results that have been presented in the year-end report. We will complete this sub-task by 12/2010.

Subtask 9.3 Rock physics modeling

What has been done:

Started in 06/2010; anticipate manuscript by 06/2011. Currently preliminary hydrates models in pore-spaces and as matrix-component are being tested by Dr. P. Dewangan at National Institute of Oceanography. We will initiate collaboration with DOE funded groups such as the Stanford group after completing sub-task 9.2 in 12/2010.

National Energy Technology Laboratory

626 Cochran's Mill Road
P.O. Box 10940
Pittsburgh, PA 15236-0940

3610 Collins Ferry Road
P.O. Box 880
Morgantown, WV 26507-0880

One West Third Street, Suite 1400
Tulsa, OK 74103-3519

1450 Queen Avenue SW
Albany, OR 97321-2198

539 Duckering Bldg./UAF Campus
P.O. Box 750172
Fairbanks, AK 99775-0172

Visit the NETL website at:
www.netl.doe.gov

Customer Service:
1-800-553-7681

